BAYESIAN DATA DRIVEN MODELLING OF KINETOCHORE DYNAMICS: SPACE-TIME ORGANISATION OF THE HUMAN METAPHASE PLATE

Constandina Koki
Zeeman Institute (SBIDER)
Mathematics Institute
University of Warwick
Coventry
United Kingdom

Alessio V. Inchingolo
Centre for Mechanochemical Cell Biology
Division of Biomedical Sciences
Warwick Medical School
University of Warwick
Coventry
United Kingdom

Abdullahi Daniyan
Zeeman Institute (SBIDER)
Mathematics Institute
University of Warwick
Coventry
United Kingdom

Enyu Li
Zeeman Institute (SBIDER)
Mathematics Institute
University of Warwick
Coventry
United Kingdom

Andrew D. McAinsh*
Centre for Mechanochemical Cell Biology
Division of Biomedical Sciences
Warwick Medical School
University of Warwick
Coventry
United Kingdom
a.d.mcainsh@warwick.ac.uk

Nigel J. Burroughs*
Zeeman Institute (SBIDER)
Mathematics Institute
University of Warwick
Coventry
United Kingdom
n.j.burroughs@warwick.ac.uk

* Corresponding authors.

Conflict of Interest: The authors declare that they have no conflict of interest.

ABSTRACT

Mitosis is a complex self-organising process that achieves high fidelity separation of duplicated chromosomes into two daughter cells through capture and alignment of chromosomes to the spindle mid-plane. Chromosome movements are driven by kinetochores, multi-protein machines that attach chromosomes to microtubules (MTs), both controlling and generating directional forces. Using lattice light sheet microscopy imaging and automated near-complete tracking of kinetochores at fine spatio-temporal resolution, we produce a detailed atlas of kinetochore metaphase-anaphase dynamics in untransformed human cells (RPE1). We fitted 18 biophysical models of kinetochore metaphase-anaphase dynamics to experimental data using Bayesian inference, and determined support for the models with model selection methods, demonstrating substantial sister force asymmetry and time dependence of the mechanical parameters. Our analysis shows that K-fiber pulling and pushing strengths are inversely correlated and that there is substantial spatial organisation of KT dynamic properties both within, and transverse to the metaphase plate. Further, K-fiber forces are tuned over the last 5 mins of metaphase towards a set point, which we refer to as the anaphase ready state.

1 Introduction

Chromosome segregation relies on the self-assembly of a microtubule-based dynamic bipolar spindle. The microtubules are dynamic, undergoing cycles of polymerisation and depolymerisation (dynamic instability). They are nucleated at the centrosomes (spindle pole), and extend radially with a subset forming bundles that connect to each of the 92 sister chromatids (replicated chromosomes). These connections are mediated by kinetochores (KTs), multi-protein machines that are able to maintain attachment to the ends of microtubule bundles as they grow and shrink thereby generating pushing and pulling forces, respectively. Each microtubule-kinetochore attachment independently generates, and also brokers, these forces to orchestrate chromosome movements and, ultimately segregation of sister chromatids into daughter cells during anaphase, [Rago and Cheeseman, 2013].

Each of the 46 sister kinetochore pairs must become bi-orientated, *i.e.,* sister chromatids are attached to microtubules emanating from opposite poles of the spindle – this is the only geometry compatible with accurate chromosome segregation. Concurrently with biorientation, chromosomes align at the spindle equatorial plane forming the metaphase plate (MPP). During metaphase, which lasts ∼10 mins, chromosomes undergo quasi-periodic oscillations along the spindle axis, [Skibbens et al., 1993, Wan et al., 2012]. These oscillations are largely driven by sister KTs switching between poleward (P; attached microtubules depolymerising) and away-from-the-pole (AP; attached microtubules polymerising) moving states. When one sister is P and the other AP the sister chromatids undergo sustained directional movement. Sisters are connected by centromeric chromatin which operates as a spring, [Jaqaman et al., 2010b]. Directional switches arise when both sister KTs switch directional state (P, AP), that is believed to be regulated by the centromeric spring tension, [Wan et al., 2012, Burroughs et al., 2015]. Metaphase oscillations provide a unique opportunity to examine the mechanisms by which KTs generate and sense forces.

The purpose of metaphase remains a mystery. One possibility is that it simply reflects a "waiting" state before anaphase onset, the duration being linked to the rates of biochemical events necessary to initiate chromosome segregation in anaphase *i.e.,* Cyclin and Securin destruction that starts after checkpoint satisfaction, although mitotic slippage can occur, [Dick and Gerlich, 2013]. However, there is evidence of mechanical changes during this time suggesting active maturation of dynamics. This includes a thinning of the MPP (reduction in width along spindle axis), thought be related to a decrease in kinetochore speed, [Jaqaman et al., 2010b], that is also observed in PTK1 cells, [Cimini et al., 2001], a decrease in KT swivel (increased alignment of the intrakinetochore axis with the sister-sister axis) reflecting a decrease in the torque acting on KTs, [Smith et al., 2016] and a synchronisation of tension across sister pairs, [Matos et al., 2009]. Of note is that metaphase oscillations in cancer cells are attenuated, [Iemura et al., 2021], and the centromere mechanical maturation from prometaphase to metaphase is disrupted in aneuploid cell lines, [Harasymiw et al., 2019].

However, a cell level or mechanistic understanding of the time evolution of forces in the mitotic spindle during metaphase and anaphase is missing. One challenge is that mitotic events occur over multiple time scales, specifically there is i) fast directional switching with both sisters switching direction on the timescale of seconds, [Burroughs et al., 2015], ii) quasi-periodic metaphase oscillations with a period of a minute, iii) slow maturation of the metaphase plate on the timescale of minutes, and iv) mitosis occurs over a duration of 20-30 mins. A second challenge is that although chromosomes are typically treated as identical objects, there is a high degree of heterogeneity. Specifically, metaphase kinetochore oscillation quality varies substantially within a cell, including a fraction of non-oscillating pairs, whilst the position of the chromosome within the 3D spindle has been reported to influence mechanical forces with both polar ejection forces (PEF), [Armond et al., 2015a, Civelekoglu-Scholey et al., 2013] and KT swivel, [Smith et al., 2016], increasing towards the periphery of the metaphase plate. Non-sister kinetochores can also influence each others'

behaviour, their motion being correlated to that of neighbouring kinetochores, [Vladimirou et al., 2013], hypothesised to be due to cross-linking between K-fibres, [Vladimirou et al., 2013, Elting et al., 2017].

Understanding this complex multi-scale mechanical system requires development of quantitative mathematical models that can capture crucial elements of the system's biophysics and regulatory properties, which can then provide quantitative support for conceptual ideas and generate testable predictions. Efforts in this direction have been ongoing since the 1980's with previous work focusing on microscopic models of kinetochore-microtubule attachment, [Hill, 1985, Joglekar and Hunt, 2002, Civelekoglu-Scholey and Cimini, 2014], on the role of bridging fibres and spindle geometry [Kajtez et al., 2016, Miles et al., 2022], and on chromosome congression dynamics to the spindle equator, [Mogilner et al., 2006, Zaytsev and Grishchuk, 2015, Blackwell et al., 2017]. Careful calibration of models to experimental data is crucial to ensure model validity; however, few studies have inferred model parameters directly from experimental data. In a previous work, Armond et al. [2015a] fitted a biophysical model of metaphase oscillations to 3D kinetochore tracking data from HeLa cells, a transformed human cancer cell line which features extensive chromosome instability. The fitted model provided fundamental insight into the forces acting on kinetochores and how sister kinetochores coordinated directional switching, [Armond et al., 2015a, Burroughs et al., 2015]. A similar analysis on non-cancer cells has not been carried out, thus given the known dynamic perturbations in cancer cells, [Iemura et al., 2021, Harasymiw et al., 2019], there is a fundamental gap in our knowledge.

In this work, we generalise the paired sister kinetochore mechanical model of Armond et al. [2015a] to incorporate sister asymmetry (so that sister kinetochores/K-fibers are not dynamically identical), time dependence in model parameters (thereby capturing dynamic maturation), and extend the model through to anaphase. Using Bayesian inference, specifically a Markov chain Monte Carlo (MCMC) algorithm, and model selection (Bayes factor assessment of preference), we parametrised our biophysical models from experimental trajectory data and determined what model extensions are supported by the data. We analyse mitosis in immortalised human retinal pigment epithelial cells (RPE1), a karyotypically stable, non-transformed cell line, using lattice light sheet microscopy (LLSM, [Chen et al., 2014]). We achieve a high signal-to-noise ratio and a temporal resolution of 2s/frame; this enables analysis of mitosis dynamics in a normal human cell line whilst ensuring minimal photobleaching and phototoxicity (all our cells transition to anaphase). We demonstrate near-complete 3D tracking of the 46 kinetochore pairs for up to 15 mins. We fit the models to kinetochore trajectories to parametrise model parameters describing chromosome dynamics. Further, we use model selection techniques to determine the support from the data for sister dynamic heterogeneity and intrametaphase temporal variation of the biophysical parameters.

Our analysis provides a comprehensive atlas of kinetochore dynamics throughout metaphase and anaphase in non-transformed human cells with a normal karyotype. In Near-complete kinetochore tracking through the metaphase-anaphase transition, we demonstrate the near complete tracking of the KT complement in RPE1 cells over 10 mins at 2s time resolution, and quantify metaphase maturation with narrowing of the MPP, although there is no change in the period of oscillation between mid and late metaphase. In section Biophysical characteristics of Quasi-periodic oscillations in diploid non-transformed human RPE1 cells, we infer the biophysical parameters of RPE1 cells on the model of Armond et al. [2015a], demonstrating key differences with HeLA cells. In later sections, we present extensions of this model and examine the support for these model variants from the data. We examine within cell heterogeneity of kinetochores in section Sister kinetochores exhibit substantial sister asymmetry in kinetochore forces, identifying natural variation in pulling and pushing forces between kinetochores, including between sisters, with K-fiber pulling strength inversely correlating with pushing strength. We go on to show in section Spatial trends: K-fiber parameters have substantial spatial variation across the metaphase plate that spatial positioning within the MPP has a substantial impact on the mechanical behaviour of sister kinetochores, such that, for some kinetochore biophysical properties, there is less variability between cells than within cells. In section K-fiber mechanical parameters are time dependent and tune towards an anaphase ready state, we examine time dependence; K-fibre strength decreases on average towards anaphase reducing the energy in the oscillations. In fact, our analysis suggests that K-fibers are tuned, their properties approaching a set point as anaphase is approached. In section Anaphase onset time is heterogeneous, we analyse anaphase dynamics, demonstrating that sister pair timing of anaphase initiation is heterogeneous within a cell, whilst anaphase speed is unrelated to metaphase K-fiber forces. In KT heterogeneity and trends are robust to perturbation of the spindle assembly pathway, we perturb spindle assembly, demonstrating that dynamics is robust to spindle reassembly and kinetochore attachment pathways, specifically KT tuning is intact, and spatial trends are nearly identical. The only key differences are weaker K-fibers, a higher PEF, lower diffusive noise and an increasing kinetochore cluster spread in anaphase under nocodazole washout. We discuss these results and possible mechanisms in section Discussion.

2 Results

2.1 Near-complete kinetochore tracking through the metaphase-anaphase transition

To obtain insight into chromosome dynamics at the anaphase-metaphase transition, we developed a tracking algorithm that achieves near-complete tracking of fluorescently labelled kinetochores, using an endogenous label of a kinetochore protein, [Roscioli et al., 2020]. The tracking pipeline consists of: deconvolving the 4D movies; detecting candidate spots with a constant false alarm rate (CFAR) based spot detection algorithm, [Daniyan et al., 2024]; refining spot locations using a Gaussian mixture model to provide subpixel resolution; fitting a plane to the KT population thus defining the metaphase plate and an associated reference coordinate system; linking detected particles between frames over time to form tracks; and grouping kinetochore sister pairs based on metaphase dynamics. This provides sub-pixel resolution for the positions of each kinetochore, and allows us to study dynamics of sister kinetochore pairs, rather than simply individual kinetochores.

We performed live-cell imaging of non-transformed human RPE1 cells using LLSM (Figure 1) and generated tracks with our tracking-pairing pipeline. Data were collected at a high temporal resolution of 2.05s per z-stack over long timescales, typically tens of minutes, starting during prometaphase through to anaphase. A typical cell is shown in Figure 1, where we detect an average of 90 spots over 350 frames (724.5 secs). This is close to the expected 92 kinetochores expected for a human cell line with a diploid 46,XY karyotype. The tracklet plot, Figure 1C, shows that 82 KTs were tracked throughout the movie, whilst a total of 100 tracks were recorded (tracks are allowed to have gaps of at most 3 missing frames). Additionally, 43 kinetochore pairs were tracked for at least 75% of the movie, with 38 KTs remaining paired for the entire duration of metaphase (sisters are allowed gaps of at most 3 frames), Figure 1D,E. The scatter plot of duration of pairing against duration either sister exists demonstrates near complete pairing over the duration of KT detection, Figure 1F. The average sister track length for this movie was 705 s. The tracks along the metaphase plate normal are shown in Figure 1G. Spot detection and tracking performance are unaffected by the transition to anaphase.

There were 36 RPE1 cells imaged over metaphase-anaphase of varying length. To assess metaphase characteristics, we use a stringent filter to give good sister pair coverage per cell, specifically we require at least 30 sister pairs both tracked for 75% of movie. This gave 31 cells, tracking 1281 sister pair kinetochores. On average, we obtained 40 sister pairs per cell (quartiles Q1=38.5, Q3=43), where both sisters were tracked for at least 200 seconds (100 frames). As is typical for mammalian cells, (see HeLa cells, [Jaqaman et al., 2010b, Armond et al., 2015a]), kinetochores form a metaphase plate (Figure 1A) and undergo saw-toothed oscillations perpendicular to the metaphase plate (Figure 1H) before separating in anaphase when kinetochores segregate towards their respective spindle poles (Figure 1D). RPE1 cells oscillate in metaphase with a period of 84s and have a median inter-sister distance (KK distance) of 1.1 microns during metaphase, averaged over cells and time, Figure 2A,C. By aligning a cell's KT trajectories to the median anaphase onset time of a cell (see Methods), we can quantify changes over time as anaphase is approached, *i.e.,* map metaphase maturation. The MPP becomes thinner over time, as measured by both the compaction of the full KT complement, Figure 2D,E, and the sister mid-points (as used in Jaqaman et al. [2010a]), Figure 2H,I. The sister KK distance reduces slightly over metaphase; it begins to increase sharply as some kinetochore pairs initiate anaphase (Figure 2F,G). We confirmed these changes by splitting metaphase into mid-metaphase (330-230 s before anaphase) and late metaphase (130-30s before anaphase, avoiding dynamics immediately prior to anaphase), showing that both the KK distance and the MPP width significantly decrease. However, the average oscillation period and strength is invariant mid to late metaphase, Figure 2B. Thus, the MPP width primarily decreases because sister pair oscillations centralise to the plate, with a smaller contribution from a reduction in oscillations amplitude (reduced average KK distance).

2.2 Modelling metaphase kinetochore dynamics

There are 4 forces acting on chromosomes, Figure 3A: the K-fibers can either push or pull the chromosomes, pulling being the substantially stronger force, [Armond et al., 2015a], the centromeric spring attaching the chromatids can be stretched/compressed thus generating an intersister force, the polar ejection force (PEF) pushes chromatids towards the cell mid-plane and drag forces damp movements, Figure 3A. In Armond et al. [2015a] the dynamics of the two kinetochore sister positions perpendicular to the MPP were modelled. Using force balance the dynamics are formulated as a pair of stochastic differential equations, but since measurements are assumed equispaced, with time interval Δt, we can integrate over the Δt (assumed small) giving a discrete time dynamics for the sister distances, X_t^k, perpendicular to the MPP, [Armond et al., 2015a],

$$\begin{aligned}\left(X^1_{t+\Delta t}-X^1_t\right)/\Delta t &= -v_{\sigma^1_t}-\kappa\left(X^1_t-X^2_t-L\cos\theta_t\right)-\alpha X^1_t+\sqrt{\Delta t}N\left(0,\tau^{-1}\right),\\ \left(X^2_{t+\Delta t}-X^2_t\right)/\Delta t &= +v_{\sigma^2_t}-\kappa\left(X^2_t-X^1_t+L\cos\theta_t\right)-\alpha X^2_t+\sqrt{\Delta t}N\left(0,\tau^{-1}\right).\end{aligned} \tag{1}$$

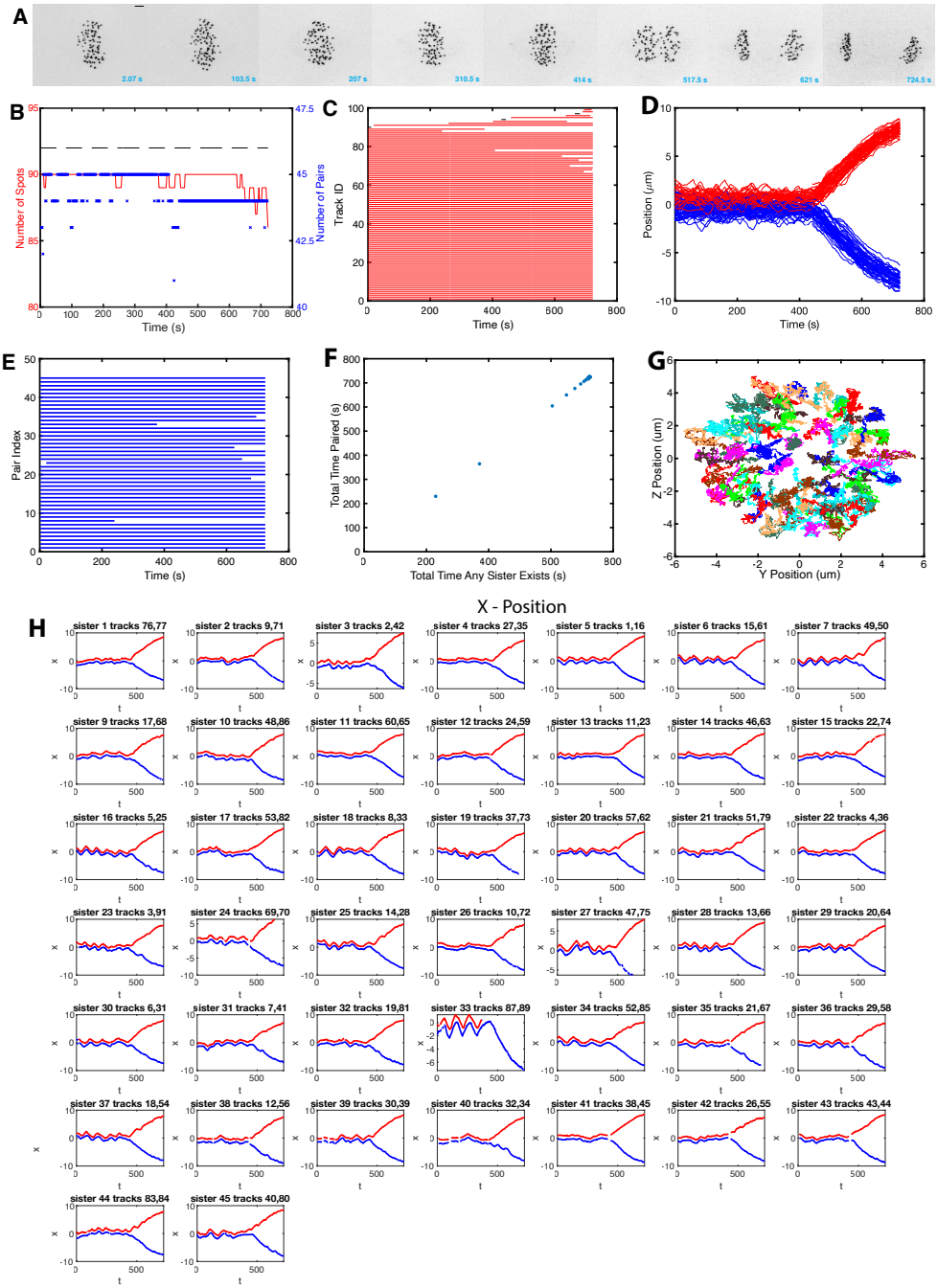

Figure 1: Near-complete tracking of kinetochores through metaphase and anaphase in human RPE1 cells. **A** Sequence of z-projected LLSM images through metaphase and the metaphase-anaphase transition (movie duration 724.5 s (2 s/frame)). Scale bar 2 microns. **B** The number of kinetochores tracked through time (red). The number of kinetochore pair trajectories at each time point (blue; only trajectories with both KTs tracked for at least 80% of the movie are shown). The dashed grey line indicates 92 kinetochores, the number in RPE1 cells. **C** Tracklet plot showing detected KT tracks, tracing the track through time; 82 tracks run through the entire movie, (3 missing time points are allowed, not necessarily consecutive). Because of track breakage, an individual kinetochore could be tracked more than once, resulting in more than a total of 92 tracks. **D** Track overlay time course showing displacement from the metaphase plate; red and blue tracks demarcate KTs descending to respective daughter cells. **E** Pairlet plot showing the times in a movie that a sister pair (by pair index) exists (and is paired). **F** Total time a sister pair is paired against total time either sister exists. **G** yz overlay of tracks in metaphase, viewed from above the metaphase plate. **H** Individual kinetochore pair tracks over time, red and blue show tracks of each KT.

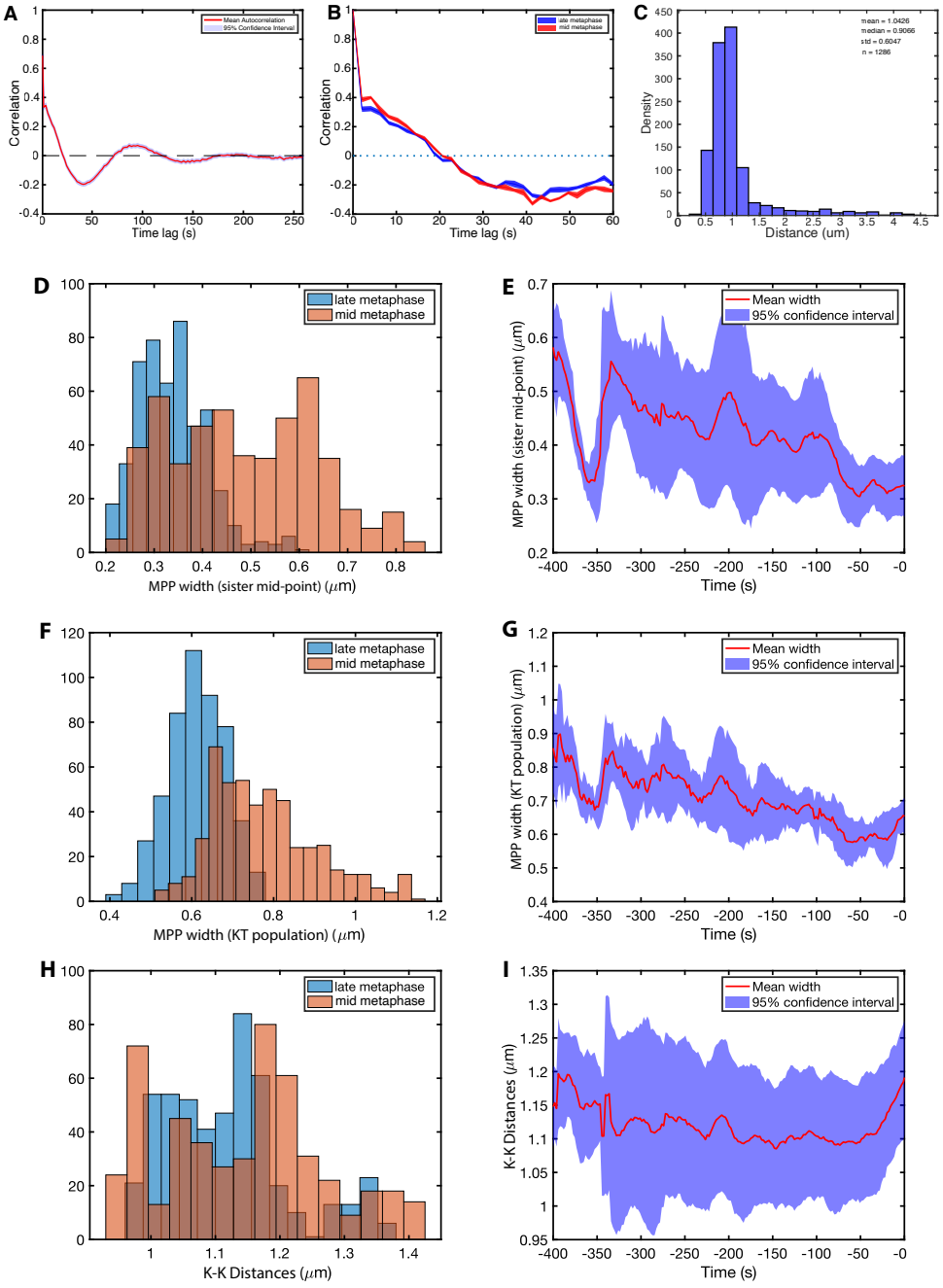

Figure 2: Quantification of intrametaphase maturation. **A** Autocorrelation plot showing the temporal correlation of metaphase oscillations. **B** Autocorrelation of metaphase oscillations in late (red) and mid (blue) metaphase. **C** Sister kinetochore (KK) distance pooled over all KT pairs and time. **D:I D/E** MPP width as measured by paired sister mid-point width (smallest eigenvalue of the covariance matrix of kinetochore mid-points). MPP statistics: **F/G** Metaphase plate (MPP) width as measured by the covariance matrix of the KT population (smallest eigenvalue). **H/I** KK distance. Comparison of mid (orange) and late (blue) metaphase in **D,F,H**, and time-series (time before anaphase onset) in **E,G,I**, mean (red) and standard deviation (blue). Data are based on cells having at least 30 sisters both tracked for 75% of movie. Mid- and late- metaphase had significantly different MPP width (both measures), and KK distance ($p_{MW} < 10^{-3}$ for **D**, **F**, **H**).

The $v_{\sigma_t^k}$ term (taking values v_+ or v_-) is the polymerisation/depolymerisation force from the K-fiber attached to sister k at time t and dependent on the current microtubule state σ_t^k corresponding to polymerising $(+)$ and depolymerising $(-)$ K-fibers, dynamics discussed below. The term $\kappa\left(X_t^1 - X_t^2 - L\cos\theta_t\right)$ is a Hookean spring force modelling the centromeric chromatin spring (assumed linear) connecting a kinetochore pair, spring constant κ, the natural length L, and θ_t is the angle between the normal to the metaphase plate and the vector connecting a sister pair at time t (thereby projecting the spring force perpendicular to the metaphase plate), Figure 3. The αX_t^1 term corresponds to the PEF pushing the chromosomes towards the equator (at $X = 0$), α is the polar ejection force parameter; we assume that the PEF is linear in the displacement from the metaphase plate since this is small relative to the length of the spindle, [Ke et al., 2009]. We assume diffusive noise, giving the Gaussian noise distribution $N\left(0, \Delta t\tau^{-1}\right)$, mean 0, variance parametrised by precision τ (inverse of variance). All forces are divided by the unknown drag coefficient as in Armond et al. [2015a]; the effect of this is that all terms in equation (1) have dimensions of speed, and units of the force parameters α and κ are $\left[s^{-1}\right]$.

The hidden states σ_t^k evolve as a discrete time Markov chain parametrised by p_{coh} and p_{icoh}, the probabilities of a kinetochore remaining in the coherent (sisters move in the same direction, states $+-, -+$) and incoherent (sisters move in opposite direction, states $++, --$) state over a time interval Δt, respectively. Specifically, the hidden states are described via the transition matrix P, with (states σ with ordering $\{++, +-, -+, --\}$),

$$P = \begin{bmatrix} p_{icoh}^2 & p_{icoh}q_{icoh} & p_{icoh}q_{icoh} & q_{icoh}^2 \\ p_{coh}q_{coh} & p_{coh}^2 & q_{icoh}^2 & p_{coh}q_{coh} \\ p_{coh}q_{coh} & q_{coh}^2 & p_{icoh}^2 & p_{coh}q_{coh} \\ q_{icoh}^2 & p_{icoh}q_{coh} & p_{icoh}q_{icoh} & p_{icoh}^2 \end{bmatrix},$$

with $q_{coh} = 1 - p_{coh}$ and $q_{icoh} = 1 - p_{icoh}$. Simulating from this biophysical model produces trajectories with quasi-periodic oscillations qualitatively similar to observed data, [Armond et al., 2015a]; saw-tooth like oscillations occur when the coherent mean lifetime is larger than the incoherent lifetime.

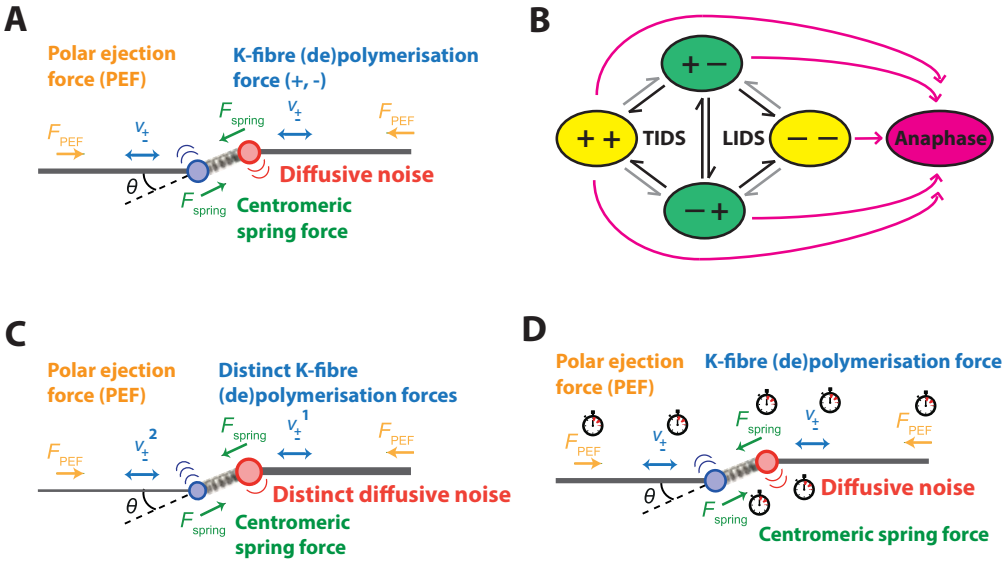

Figure 3: Biophysical model schematics for KT dynamics in metaphase and transition to anaphase. **A** Basic metaphase model of Armond et al. [2015a] showing the forces on a KT pair: K-fiber forces (either depolymerising or polymerising), spring force (green), PEF (orange) and diffusive noise (pink). Drag force not shown. **B** Schematic of hidden states comprising sister pair K-fiber polymerisation states (+ polymerising, − depolymerising). Transitions between states are either initiated by the leading sister (Leading sister Induced Directional Switch, LIDS) or the trailing sister (Trailing sister Induced Directional Switch, TIDS); a joint switch (both sisters switching direction in the same frame) is rarer. Saw tooth oscillations arise because the coherent states $(++, --)$ are of longer duration. In black is the first sister switching, grey the second. Anaphase onset is an irreversible transition (pink), *i.e.,* Anaphase is a trapping state. **C** Sister asymmetry model variants where sister K-fiber forces (v_+ or v_-) and/or diffusive noise may be unequal. **D** Model for time dependence in the biophysical parameters.

Bayesian inference of biophysical parameters

We take a Bayesian approach fitting the models directly to each experimental trajectory, a method that infers all the biophysical model parameters jointly. In essence, Bayesian methods sample parameter values consistent with observed data. Crucially, this allows us to quantify uncertainty in the fitted parameters. We use STAN [Stan Development Team, 2024b, Carpenter et al., 2017] that uses an Hamiltonian Markov chain Monte Carlo algorithm, [Betancourt and Girolami, 2015, Neal, 2011]. In Bayesian analysis, the key quantity is the posterior distribution $P(\theta|x_{1:T})$ of the model parameters $\theta = (\tau, \alpha, \kappa, v_-, v_+, L, p_{coh}, p_{icoh})$ given the observed data, x_t, in our case a sister pair trajectory $x_t = [X_t^1, X_t^2]$. Details on the likelihoods for each model, how we deal with missing data and the parameter and hidden state sampling (from the posterior distribution) are given in the Appendix C. There is an identifiability issue in all models such that the natural length L is poorly inferred from the data. This is discussed in Armond et al. [2015a] and resolved by measuring the natural length in nocodazole (which depolymerises all MTs); the average natural length (KK distance) for RPE1 cells is 0.78 microns, similar to HeLa cells at 0.76 microns, [Armond et al., 2015a]. All the models analysed in this paper then satisfy practical identifiablity [Hines et al., 2014, Browning et al., 2020].

Prior to fitting these models, we implemented a data quality control. In particular, we discarded cells with a low coverage of sister pairs or a very high proportion of poor oscillators (indicating poor health), and for the metaphase-anaphase model, if there was insufficient anaphase. This reduced the analysed cells from 36 DMSO treated cells to 28 cells. We also filtered KT-pair trajectories, requiring no more than 20% missing data, and cell videos are required to have at least 120 metaphase frames. Trajectories with poor inference, identified by severe divergences in STAN, were excluded, and cells were discarded if a high proportion of sister pair trajectories showed frequent divergences, resulting to a further reduction of the analysed cells to 26. While divergences indicate the model isn't fully capturing the dynamics, they were rare (1.5%; Appendix C, with slight variations between the different models). Hence, in the model analysis there are slight differences in the number of trajectories considered due to performance issues. For the metaphase dynamics models (that don't include the anaphase transition), we truncated the trajectories to metaphase. Specifically, we used a change point model to detect the anaphase transition per KT pair, Appendix D. Then we truncated 30s before this, to ensure the cell is in metaphase.

Model selection

Model selection is based on pairwise comparison of models using the Bayes factor, all model comparisons being nested; thus we assess the evidence for increasing the complexity of the model. The Bayes factor for model M' relative to a simpler model M is the fraction $B = \frac{\pi(D|M')}{\pi(D|M)}$ given data D; the model marginals $\pi(D \mid M)$ are computed using a bridging sampler, Gronau et al. [2020]. We use the criteria of Kass and Raftery [1995] and chose the more complex model if it had at least substantial preference over the simpler model (Bayes factor $B > 3.2$). We initially determine which models are supported relative to the basic model (eq. (1)), giving a set of preferred models. Within this set, any nested models we then assessed for support for increasing the complexity using the Bayes factor between pairs of models in the nesting, removing any more complex models for which increased complexity is not supported. If multiple models remain, we select the model with the highest Bayes factor (relative to the basic model) as the preferred model. In this way we navigate the model network to determine the model with the greatest support, and with model complexity justified by the data. This iterative process allows us to navigate the model space systematically, identifying the model with the strongest support while ensuring it's complexity is justified by the data.

2.3 Biophysical characteristics of Quasi-periodic oscillations in diploid non-transformed human RPE1 cells

We use model (eq. (1)) to infer all the biophysical model parameters concurrently, see Appendix C. We analysed (after data quality filtering) 26 cells, 798 KT pairs, an average of 31.9 sister pairs/cell. The inferred (marginal posterior) distributions for each of the biophysical model parameters are shown in Figure 4 for a single sister pair trajectory. A comparison between the prior and posterior marginals demonstrates that all parameters are identifiable except for the natural length L which has a posterior nearly identical to the prior, expected given its identifiability issues, [Armond et al., 2015a]. The model fit to the trajectory provides an automated state annotation, *i.e.,* the hidden K-fiber polymerisation state is inferred at each time point, Figure 4B, thereby allowing switching events of KT sister pair state to be inferred. Metaphase quasi-periodic oscillations require that both KTs of a sister pair change direction at a directional switch, [Armond et al., 2015a]. There are two switching choreographies; a switching event initiated by the leading sister (lead induced directional switch, or LIDS) and switching initiated by the trailing sister (trail induced directional switch, or TIDS), Figure 3B; coincident switching (within the time resolution) is rare. In this trajectory directional switching (between coherent states $+-$ to $-+$, or $-+$ to $+-$), occurs through LIDS events, *i.e.,* the intermediate state is $++$, compressing the centromeric spring. Both choreographies are in fact observed (26 cells, 798 KT pairs) with a LIDS/TIDS ratio of 3.2, specifically 68.5% LIDS, and 21.1% TIDS and 10.3% joint switches. This is similar to that previously reported for HeLA cells, with a LIDS/TIDS of 3.8, [Armond et al., 2015a].

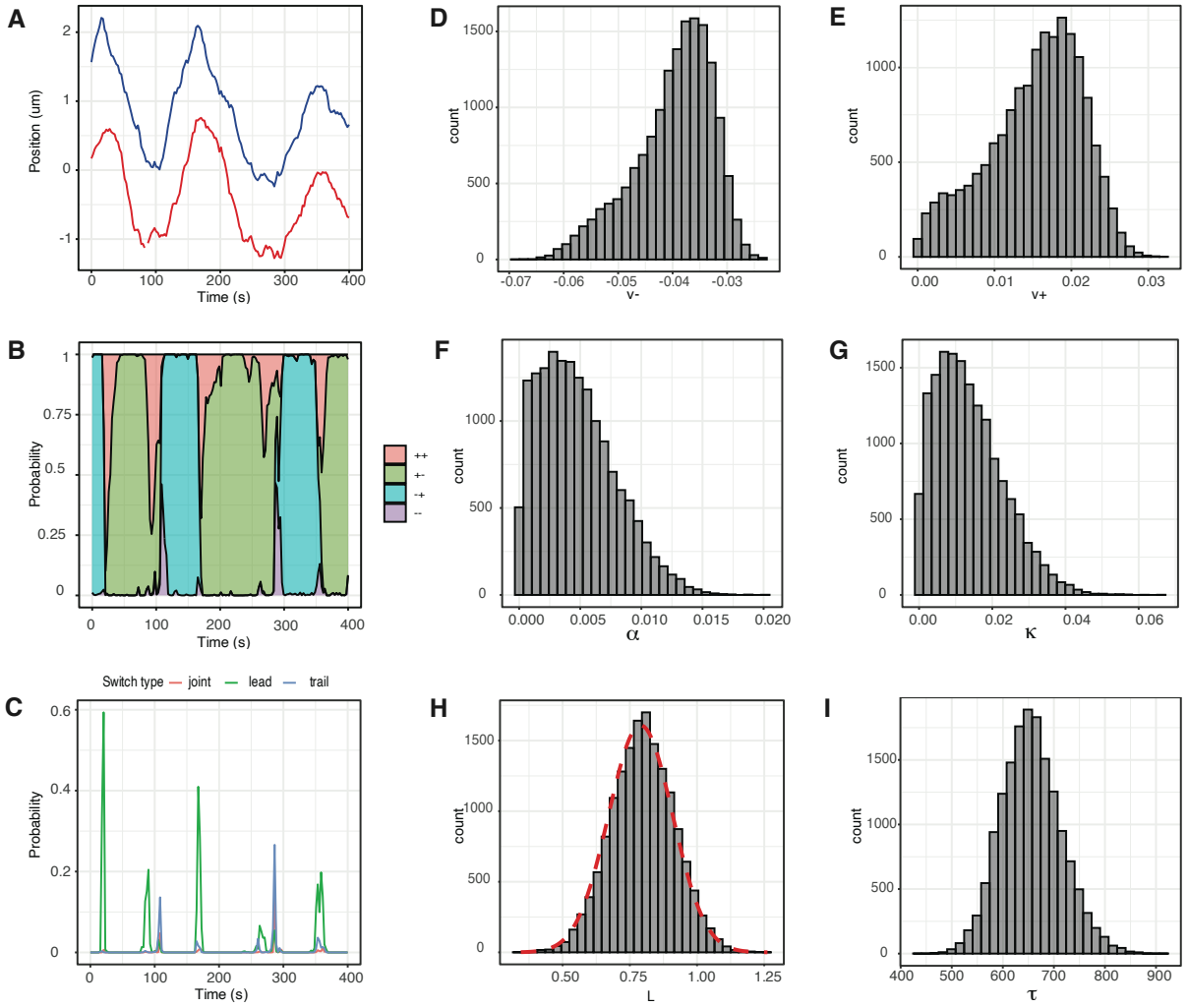

Figure 4: Single trajectory model inference showing parameter estimates and trajectory annotation. **A** Observed KT sister pair trajectory from LLSM tracking the Ndc80-eGFP endogenously marked KTs. **B** Trajectory annotation for the hidden K-fiber polymerisation states; probability $P\left(\sigma_t | x_{1:T}; \theta\right)$ for being in each state at each time point as sampled via the backward algorithm (see Methods). **C** Probability of a directional switch initiated by the leading kinetochore (green), trailing kinetochore (grey), or a joint switch (red). Switching probability is assessed using the sampled hidden states and corresponds to a proportion of MCMC samples matching a particular pattern of states (e.g. $[-+,-+,++,+-]$ or equivalent for a LIDS) corresponding to a given switch type. **D-I** Marginal posterior distribution of the biophysical parameters for the trajectory data in A. In **H** the informative prior density plot for natural length L is plotted with red dashed line on top of posterior histograms.

Variables	Median	PIR
τ	673.7 [241.4]	95.042
κ	0.022 [0.018]	0.018
α	0.009 [0.008]	0.005
v_-	-0.041 [0.021]	0.008
v_+	0.010 [0.010]	0.007
L	0.808 [0.033]	0.158
p_{icoh}	0.760 [0.216]	0.155
p_{coh}	0.949 [0.027]	0.026

Table 1: Inferred biophysical parameter values of all sister KT-pairs using the model (1) (model of Armond et al. [2015a]). The first column reports the median of the posterior medians for each parameter, and in brackets the population interquartile range. The second column reports the median of the inferred Posterior Interquartile Ranges (PIR) of each parameter. Based on 26 cells, 798 KT pairs.

Inferred biophysical parameters for RPE1 cells are given in Table 1. Compared to HeLa cells, [Armond et al., 2015a], the average sister-sister separation and the period of the quasi-periodic oscillations are larger, Figure 2, 1.68 microns and 102 secs respectively, (based on the autocorrelation function, ACF), compared to 1 micron, 70 seconds, in HeLa cells, [Burroughs et al., 2015]). The model enables these differences to be unravelled as differences in the K-fiber forces, the PEF and the centromeric spring. The most substantial difference is the distribution of the spring constant, κ, which has shifted to smaller values for RPE1 cells ($0.022 \pm 0.007\ s^{-1}$; mean $\pm$ population standard deviation) compared to the previous estimates for HeLa cells ($0.03 \pm 0.01\ s^{-1}$). This therefore indicates that RPE1 cells have a more compliant (weaker) centromeric chromatin spring than HeLa cells. Other notable differences compared to previous estimates in HeLa cells relate to the microtubule speed parameters, v_- and v_+. The magnitude of these parameters have a greater difference ($|v_-| - v_+$) in RPE1 cells compared to HeLa cells; v_- is estimated as -41 ± 18 nm/s in RPE1 cells versus -35 ± 15 nm/s in HeLa, similarly v_+ is estimated as 10 ± 10 nm/s in RPE1 cells versus 13 ± 16 nm/s in HeLa, (mean $\pm$ standard deviation of the population). It should be noted however, that the HeLa cell analysis in Armond et al. [2015a] is based on far lower coverage of kinetochores than the current analysis, which may affect estimates.

2.4 Sister kinetochores exhibit substantial sister asymmetry in kinetochore forces

The above model assumes sister KTs and K-fibers are biophysically identical, *i.e.,* have the same pulling and pushing forces. Here, we relax the assumption of sister symmetry in the K-fiber forces and their noise terms, *i.e.,* the sisters can have distinct (unloaded) velocities $v^k_\pm$ and noise (precisions τ^k) in eq. (1), $k = 1, 2$, Figure 3C. Clearly κ is common, whilst α could be asymmetric, although this would be a spindle pole asymmetry because the sister chromatids are identical in shape and elasticity, so we do not consider that here. The full asymmetric model is given by, (generalising model eq. (1))

$$\begin{aligned} X^1_{t+\Delta t} &= X^1_t + \Delta t\left(-v^1_{\sigma^1_t} - \kappa\left(X^1_t - X^2_t - L\cos\theta_t\right) - \alpha X^1_t\right) + \sqrt{\Delta t}N(0,(\tau^1)^{-1}),\\ X^2_{t+\Delta t} &= X^2_t + \Delta t\left(+v^2_{\sigma^2_t} - \kappa\left(X^2_t - X^1_t + L\cos\theta_t\right) - \alpha X^2_t\right) + \sqrt{\Delta t}N(0,(\tau^2)^{-1}), \end{aligned} \tag{2}$$

the hidden states $\sigma^k_t \in \{+,-\}$ have the same dynamics as above. This model allows sisters to differ in all 3 variables; we also consider the reduced models with only 1 or 2 parameters being different, giving 7 asymmetric models and the symmetric model (eq. (1)). A more complex model is deemed to be supported from the data if the Bayes factor $B > 3.2$, see Appendix C. The false positive rate was evaluated for the asymmetric $v_\pm$ model relative to the symmetric model, giving a false positive rate of around 1% on simulated data. We report results of the following 5 models

- M_0 no asymmetries, *i.e.,* symmetric model (eq. (1)).
- $M^a_{v_-}$ asymmetry only on v_-
- $M^a_{v_+}$ asymmetry only on v_+
- $M^a_{v_\pm}$ asymmetries on v_- and v_+
- $M^a_{v_\pm\tau}$ asymmetries on v_-, v_+ and τ

with the superscript a denoting asymmetry models, subscript which parameter(s) are asymmetric. The other models were rarely preferred, so not discussed further. The model likelihoods these 5 models are given in Appendix C.

We fitted the 4 asymmetric sister models to 26 cells, 798 sister pairs. In RPE1 cells, 24.4% of sister kinetochores have significant asymmetry, with most, (42.6% of asymmetric pairs) preferring asymmetry in $v_- v_+$ whilst 87.7% have significant asymmetry in v_-, Figure 5B, Table 2. However, (significantly) asymmetric sisters only show mild differences in biophysical parameters relative to symmetric sisters, Table 3, asymmetric and symmetric trajectories in fact appear similar, Figure 5C. Asymmetric sisters have a significantly different (larger) average pulling force (averaged over the two sisters) than symmetric sisters 9.3% ($p_{MW} < 10^{-7}$, one-sided)[1], whilst the centromeric spring constant, PEF potential and natural length are 15.9 % ($p_{MW} = 0.01$), 34.3% ($p_{MW} < 10^{-7}$) and 2.6% ($p_{MW} < 10^{-6}$) larger. Since it is easier to detect differences when $|v_-|$ is larger, the asymmetric group would be expected to have a larger average v_-. In all cells there is a fraction of (significantly) asymmetric sisters, see Appendix Figure B3A,B, while, there is also no half-spindle bias in the (significantly) asymmetric KTs, *i.e.,* cells exhibit equal numbers of stronger KTs to the right, respectively left, half-spindle, Appendix Figure B3C,D. Thus, kinetochore asymmetry is not due to spindle asymmetry, that can arise because of a younger and older centrosome.

Preferred Model	v_-, v_+, τ	v_-, v_+	v_-	v_+	Totals
Strength of Asymmetry			**DMSO**		
Substantial	1	24	36	13	74
Strong	1	27	32	8	68
Decisive	0	37	15	1	53
Substantial+	2 (1.03%)	88 (45.13%)	83 (42.56%)	22 (11.28%)	195
Strength of Asymmetry			**Nocodazole**		
Substantial	0	23	35	29	87
Strong	0	39	33	15	87
Decisive	2	56	47	7	112
Substantial+	2 (0.7%)	118 (41.46%)	115 (40.07%)	51 (17.77%)	286

Table 2: Asymmetry profile: Detailed report of the preferred asymmetric models over the DMSO and nocodazole washout treated cells. We observe that asymmetric sisters are predominately asymmetric on v_-.

We next addressed if this random (natural) variability in $v_\pm$ between sisters is independent. We observed a correlation between pushing (v_+) and pulling (v_-) forces in the asymmetric population, Figure 5D, with K-fibers that are stronger at pulling being weaker at pushing ($p_{Binom} < 10^{-8}$, rejecting the null hypothesis that the strongest pulling sister (v_-) had equal probabilities of being either the stronger or weaker pushing sister (v_+)). Thus, pairs where a sister is both a stronger puller and pusher (respectively weaker puller and weaker pusher) are in a minority. When we tested for independence on the full asymmetric model, using all KTs, we find that the v_+^k, v_-^k parameters are not independent ($p_{Hoef} < 10^{-18}$, $p_{DC} < 10^{-4}$, $p_{Corr} < 10^{-5}$). Drived by this result, we modelled the joint empirical distribution of v_-, v_+ by fitting a mixture of multivariate Gaussians, Appendix Figure D18A. This model fitted extremely well, the QQ plot in fact indicating that there are no extremal subpopulations with large, or small, $|v_-|$, Appendix Figure D18B. Hence, this suggests that sister asymmetry is caused by natural variation of the K-fibres within a cell. We therefore investigated if sister-sister difference are similar to non-sister differences. We examined the distribution of sister differences, $\Delta v_\pm = v_\pm^1 - v_\pm^2$, and tested if this was identical to non-sister differences by randomising the pairing, Figure 5E. There was no significant difference (1% level) between these distributions ($p_{MW} = 0.986$, $p_{MW} = 0.621$, for $\Delta v_- = v_-^1 - v_-^2$ and $\Delta v_+ = v_+^1 - v_+^2$, respectively and $p_{KS} = 0.056$ and $p_{KS} = 0.141$ for $\Delta v_- = v_-^1 - v_-^2$ and $\Delta v_+ = v_+^1 - v_+^2$, respectively). This result also holds when we allow for the effects of location in the MPP (applying the same tests on 5 equally sized groups, based on their averaged location on the metaphase plate, see Section 2.6). The lowest p-value for the tests over the 5 classes was $p_{MW/KS} = 0.385$.

Our analysis suggests that K-fiber forces are intrinsically variable and therefore sister differences (asymmetry) is a continuum. The significantly asymmetric sisters will therefore be those with the largest differences. Notably, the mechanism introduces an inherent anti-correlation between pulling and pushing forces.

2.5 Spatial trends: symmetric and asymmetric sisters are organised transversely to the MPP

Our analysis reveals that K-fibers are intrinsically noisy, which results in an asymmetry in sister KTs in $v_\pm$ and in the diffusive noise τ, Figure 5. Sister asymmetry in pulling forces should localise the sister pair off centre of the MPP plate, the K-fiber depolymerisation force being the dominant force acting on the chromosome, [Armond et al., 2015a]. Specifically, a sister pair with a substantially stronger pulling sister will be pulled on average towards its

[1]Details and abbreviations on the statistical tests used in throughout our analysis can be found in Appendix Table C8.

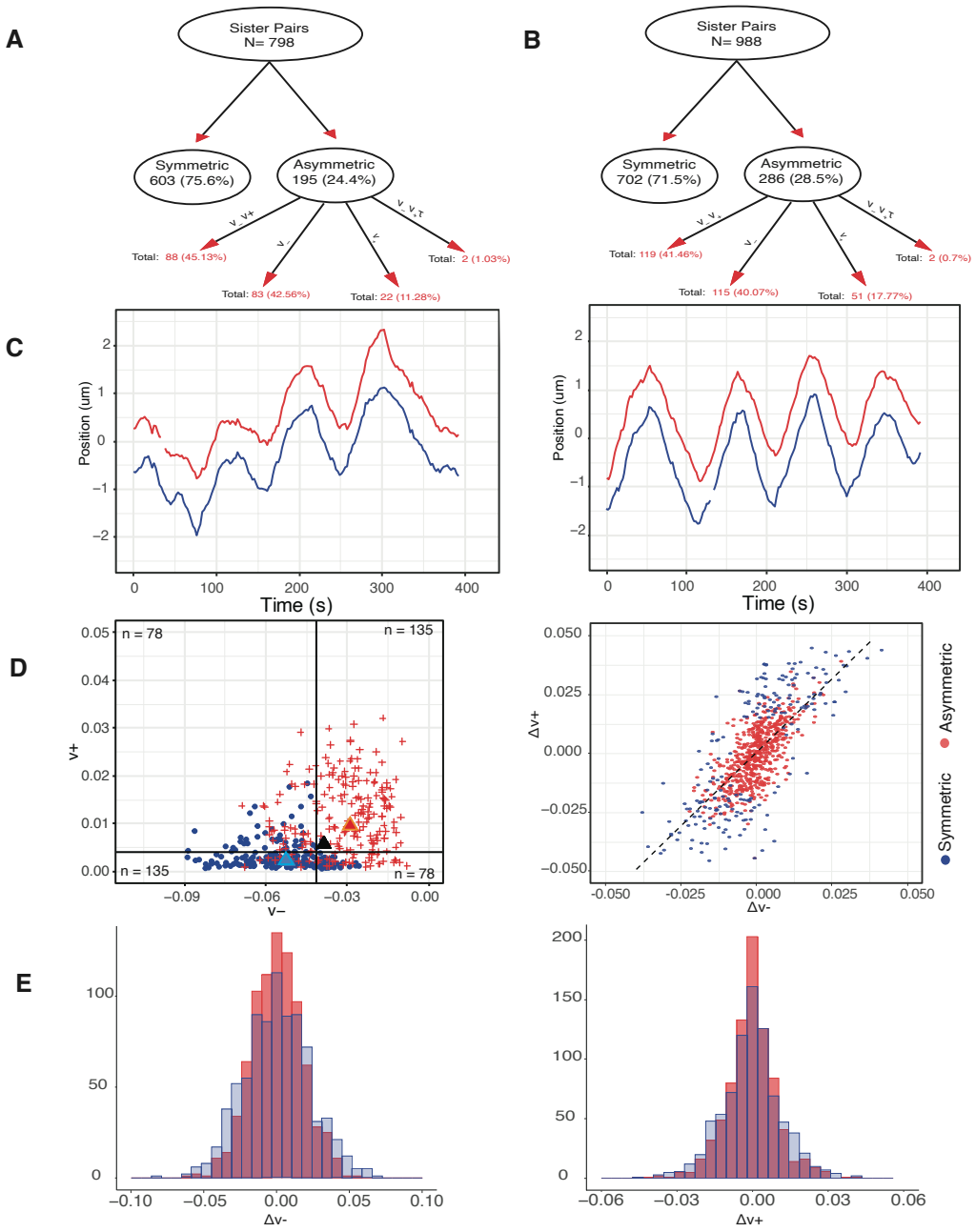

Figure 5: Asymmetry in sister kinetochores is a result of natural variation (noise). **A/B** Graphical representation of asymmetry model preference network in DMSO (A) and Nocodazole (B) treated cells. **C** Typical symmetric (left) and asymmetric (right) trajectory, DMSO treated. No distinctive characteristics between the symmetric and asymmetric sister pairs. **D** (Left) Comparison of inferred v_- and v_+ of asymmetric sister pairs (on asymmetric $v_\pm$ model). For each pair, the stronger and weaker pulling sister are shown, blue and red respectively. Population medians are marked with triangle, while the black triangle shows the population median of the symmetric pairs. The number of KTs in each quadrant is shown in every quadrant corner. (Right) Scatter plot of sister difference in pulling force $\Delta v_- = v_-^1 - v_-^2$ versus pushing force $\Delta v_+ = v_+^1 - v_+^2$, with symmetric and asymmetric sister pairs indicated in red and blue respectively, (inferred on the $v_\pm$ asymmetric model). Asymmetric pairs do not present any distinctive pattern. **E** Histograms of the sister difference distribution, *i.e.,* Δv_- (left) and of Δv_+ (right), when sisters are paired (red) and randomised pairing (blue), (randomisation is restricted to a metaphase radial box to account for variation with respect to the metaphase plate distance, see Figure 7).

	Symmetric		Asymmetric	
	Median	PIR	Median	PIR
τ	661.8 [265.4]	95.055	700 [311.9]	96.90
κ	0.020 [0.018]	0.017	0.023 [0.022]	0.017
α	0.010 [0.008]	0.005	0.013 [0.010]	0.005
v_-^1	-0.042 [0.021]	0.008	-0.060 [0.020]	0.009
v_-^2	-0.042 [0.021]	0.009	-0.032[0.026]	0.009
v_+^1	0.010 [0.010]	0.007	0.004 [0.005]	0.007
v_+^2	0.010 [0.010]	0.007	0.015 [0.016]	0.007
L	0.806 [0.033]	0.156	0.839 [0.067]	0.155
p_{icoh}	0.734 [0.216]	0.173	0.766 [0.215]	0.133
p_{coh}	0.950 [0.027]	0.026	0.952 [0.024]	0.024

Table 3: Summary statistics of symmetric and asymmetric sisters. We label sister 1 as the sister with the greater pulling force (*i.e.,* $\left|v_-^1\right| \geq \left|v_-^2\right|$). The first and third columns reports the medians of posterior medians for symmetric and asymmetric sisters respectively, while brackets report the population interquantile range. The second and fourth columns report the median of Posterior Interquantile Ranges (PIR) for symmetric and asymmetric sisters, respectively. Based on Mann-Whitney and Kolmogorov-Smirnov tests, the asymmetric posterior distributions of κ,α, v_- and L are significantly different that the symmetric posterior distributions, with size of effect (*i.e.,* percentage difference of the medians) being 15.9%, 34.3%, 9.5% and 2.6% . Inference on asymmetric sisters is based on $M_{v\pm}^{\alpha}$.

pole, experiencing on average a higher PEF force from that pole, the pair thus achieving a stable average off-centre position towards the stronger sister's pole. This is in fact observed, significantly asymmetric sister pairs are localised on average towards their pole relative to symmetric sisters, Figure 6A. To ascertain if this repositioning is retained through anaphase, we back-tracked the KTs that descend to respective poles tracking the cluster back through metaphase. Within each poleward destined cluster, we can partition the KTs into 3 groups, firstly those that are part of a symmetric pair, secondly the stronger pulling sister of an asymmetric pair and finally the weaker pulling sister of an asymmetric pair. The stronger pulling sisters are positioned towards the pole in metaphase, Figure 6C, as expected since the sister centre is offset towards the stronger sister's pole, an offset that is significant relative to the KTs from symmetric pairs, $p_{MW/KS} < 10^{-16}$. This offset is in fact retained through into anaphase, Figure 6E. Similarly, the KTs that have the weaker pulling force of an asymmetric pair are positioned away from the pole to which they descend, $p_{MW/KS} < 10^{-14}$, Figure 6C,E. An analysis of the KT position ranking within its cluster (ranked mean position towards the pole) also demonstrates the relative positioning of the weaker and stronger sisters of an asymmetric pair compared to kinetochores of a symmetric pair, Appendix Figure B16. The relative positioning is in fact fairly stable through metaphase with a small number of KTs changing position – what is surprising is that asymmetric KTs tend to be at the extremes, the majority in their correct position (rank), but a minority diametrically opposite. Our results demonstrate that there is an ordering along the spindle axis (MPP normal) of KTs that is a consequence of unequal K-fiber pulling forces in metaphase, an ordering that is retained through anaphase. Thus, stronger KTs of a sister pair are positioned in the front of the cluster, weaker KTs at the back in metaphase and anaphase.

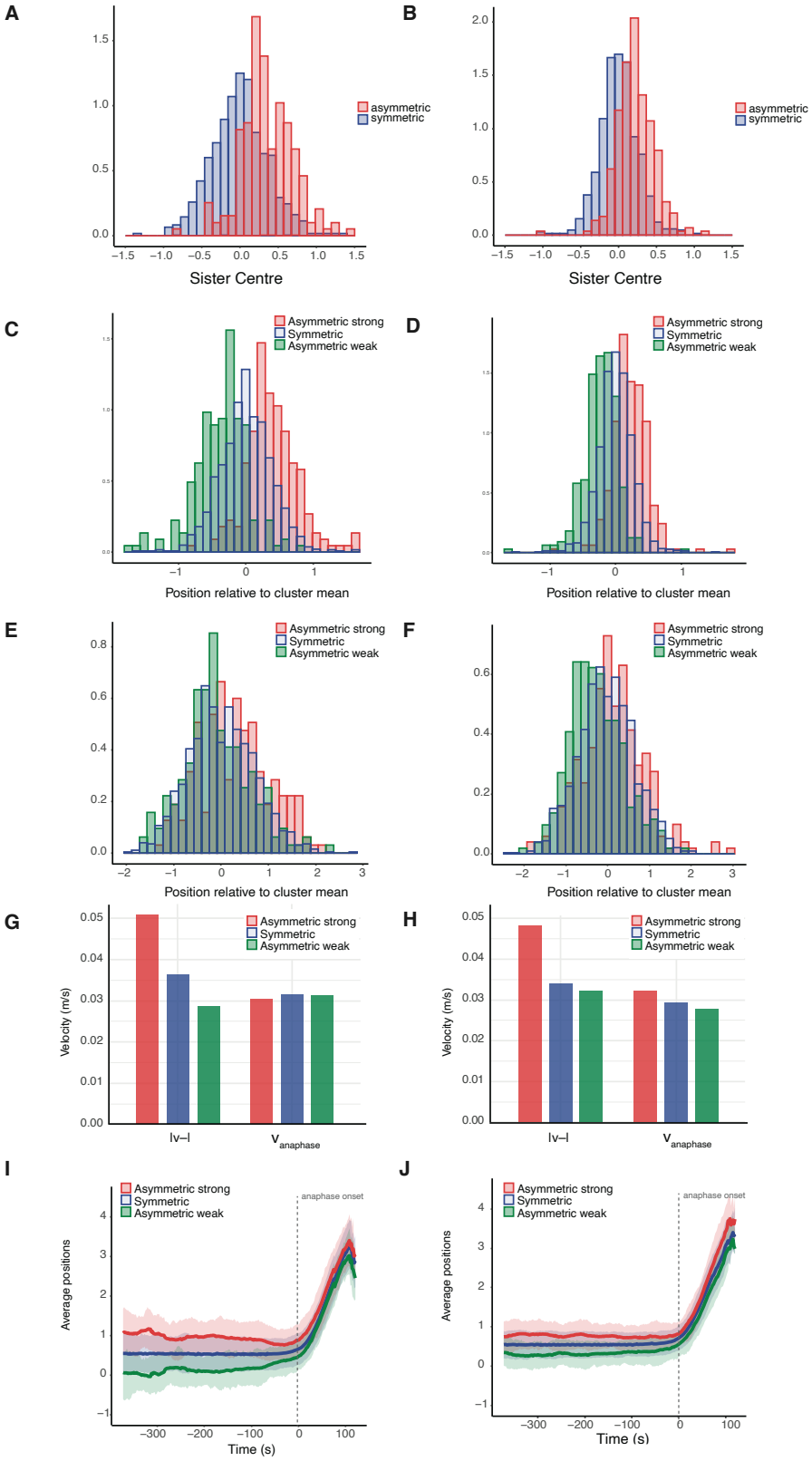

Figure 6: Symmetric and asymmetric kinetochores are laterally organised transverse to the MPP. *Caption continues*.

Figure 6 continued. Pulling strength group position lateral to the MPP. Left (**A,C,E,G,I**) DMSO (195 asymmetric and 603 symmetric sister pairs) Right (**B,D,F,H,J**) Nocodazole washout treated cells (286 asymmetric and 702 symmetric sister pairs) right. **E/F** Mean positions of sisters relative to their cluster mean in anaphase. Cumulative distributions of asymmetric stronger pulling is significantly greater than cumulative symmetric distribution which in turn is statistically greater than asymmetric weaker pulling ($p_{KS} < 10^{-6}$, DMSO, $p_{KS} < 10^{-4}$ Nocodazole. In addition, the median of asymmetric stronger pulling is significantly greater than the median of symmetric sisters which in turn is significantly greater than the median of asymmetric weaker sisters for both DMSO and nocodazole washout treated cells, ($p_{MW} < 10^{-5}$, $p_{MW} < 10^{-10}$). **G/H** Comparison of averaged median speeds v_- and $v_{anaphase}$ for pulling strength groups on **G** DMSO ($N = 611$) and **H** nocodazole washout ($N = 767$) treated cells, with no reversals. **I/J** Evolution of the average positions for **I** DMSO and **J** nocodazole washout treated cells. Shaded envelope shows interquartile range for each group. $t = 0$ denotes the median anaphase onset per cell.

2.6 Spatial trends: K-fiber parameters have substantial spatial variation across the metaphase plate

Previous reports suggest that KT dynamics varies with position in the MPP, in particular that (i) trajectories are more stochastic towards the periphery, [Jaqaman et al., 2010b, Armond et al., 2015a] (ii) that the PEF increases towards the periphery of the MPP, [Armond et al., 2015a] and (iii) that sister pairs at the periphery exhibit higher swivel, [Smith et al., 2016]. To determine if there are trends in the biophysical parameters with distance r from the centre of the metaphase plate in RPE1 cells, we partitioned the population of KTs with respect to position, as in Armond et al. [2015a], Figure 7. There are substantial trends with r in a number of parameters, specifically the pulling v_- ($p_{Corr/Kendall/Spearman} < 10^{-16}$) and pushing v_+ ($p_{Corr} < 10^{-7}$, $p_{Kendall/Spearman} = 0.002$) forces, the spring constant κ ($p_{Corr} < 10^{-8}$, $p_{Kendall}, p_{Spearman} < 10^{-13}$) and precision τ, ($p_{Corr/Kendall/Spearman} < 10^{-16}$). These trends are also detectable in single cells, Appendix Figure B5. In contrast to previous reports (on HeLA cells) there was no trend in the PEF, which was invariant with r ($p_{Corr} < 0.48$, $p_{Kendall/Spearman} = 0.12$), see Appendix Table A4 for a summary of p-values. In the previous study, Armond et al. [2015a] did not observe any trends in the other dynamic parameters that we see here in RPE1 cells. The coverage in Armond et al. [2015a] was substantially lower than in our study, which may explain these differences; however, they could also reflect differences between RPE1 and HeLa cells. Chromosome size is known to increase towards the periphery, [Mosgöller et al., 1991, Booth et al., 2016], which could increase drag forces towards the periphery, whilst drag may also be dependent on MT density, that may vary laterally across the spindle. In our model the drag coefficient is not inferable separately, but scales all the mechanical parameters as follows, generalising eq. (1):

$$\left(X^k_{t+\Delta t} - X^k_t\right) = \gamma(r)^{-1}\left(-v_{\sigma^k_t} - \kappa\left(X^1_t - X^2_t - L\cos\theta_t\right) - \alpha X^k_t\right) + \sqrt{\Delta t} N(0, (\tau\gamma(r)^2)^{-1}), \tag{3}$$

Thus, $v_\pm, \kappa, \alpha, \tau^{1/2}$ would scale identically with r. The scalings are compared in Figure 7B. There is substantial variation in the relative reduction in the parameters (percentage difference peripheral to middle of MPP 38%, 25%, 9%, 53% and 2% of v_-, v_+, α, κ and L respectively), whilst an opposite trend is seen for $\tau^{-/2}$, which increases by 10%, suggesting that solely changing drag across the MPP is not consistent with the data. The relative changes in the parameters are also not consistent with changing both drag and chromosome size across the MPP; a change in chromosome size would affect both the drag and the PEF.

Biological variation of KTs and K-fibers is expected to produce variation in the mechanical properties of KTs/K-fibers, and subsequently their dynamics. The variation we see with respect to location in the metaphase plate in our pooled cell samples indicates that within cell variation is in fact substantial since it is evident even on data pooled over cells. To ascertain the contributions to the variance from spatial location and biological variation between cells we performed a 2-way ANOVA on the median estimates per sister pair for each parameter, Table 4, with a 2-way grouping with respect to the 5 radial partitions and 26 cells. The interaction term (between radial location and cell) was always insignificant (in all parameters), so removed from the ANOVA analysis. In all parameters cell grouping was significant, whilst MPP location was significant in all except α and L. However, the variance contributions from location and cell showed high variability; the location variance of v_- is 2 orders of magnitude larger than that due to the cell variation, whilst the location variance of switching parameter p_{icoh} is also substantially larger indicating that the duration of directional switching is heterogeneous with location. All other parameters have similar (or smaller) variance contributions from location and between cells (the natural length has a strong prior and the size of effect is small despite a significant difference between cells, whilst it also has negligible trend with r). The higher between cell variance of α suggests that the PEF varies substantially between cells, whilst K-fibre depolymerisation forces and the centromeric spring varies substantially within cells, consistent with the strong trends seen in Figure 7. Examining the relative standard deviation shows that variation of v_+, α, κ is substantial (over 35%), whilst that of v_- is lower (17%), reflecting the fact that pulling is the dominant force, Table 1 and Armond et al. [2015a]. Scatter plots with respect to cell for v_-

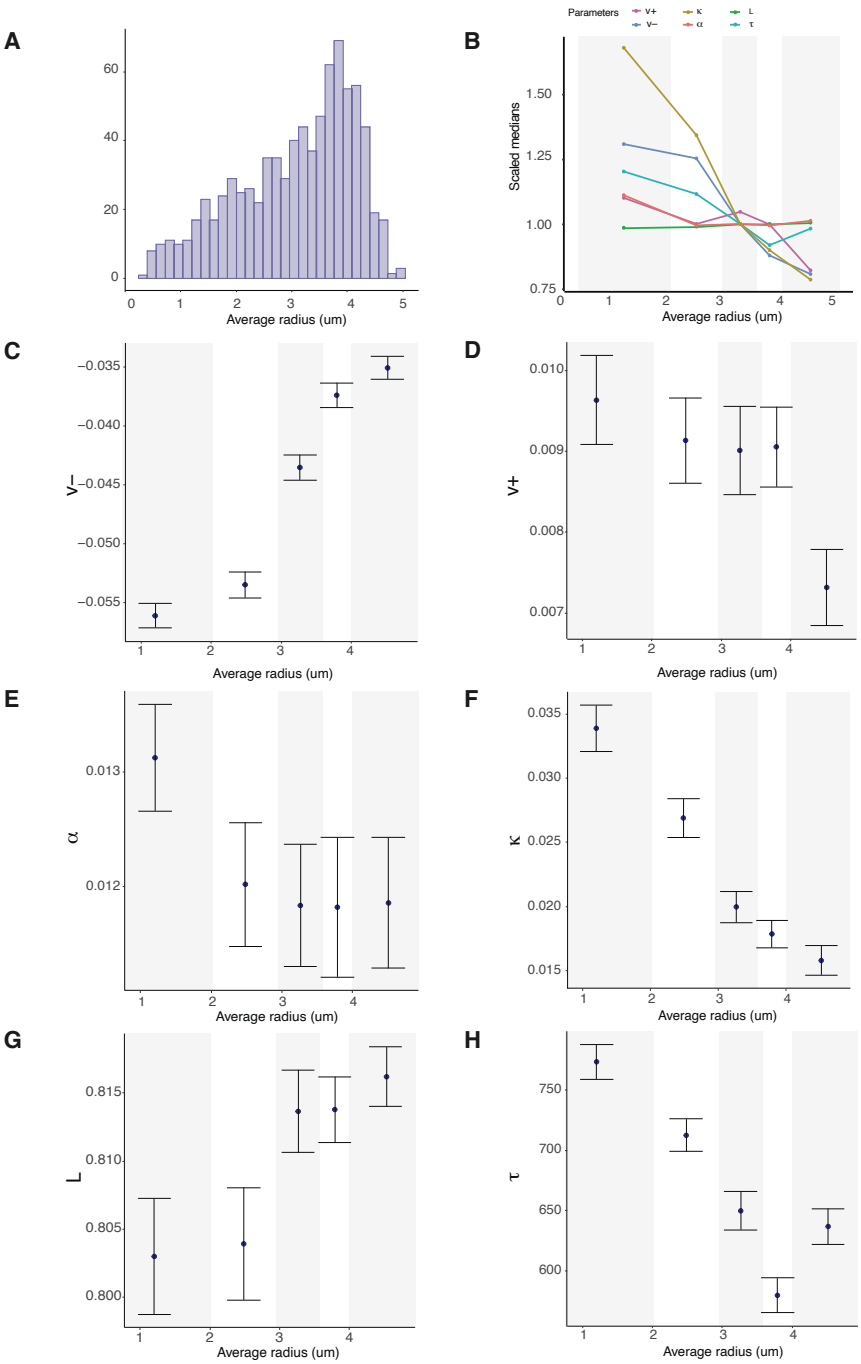

Figure 7: K-fiber pulling strength and centromeric spring stiffness decreases towards the periphery of the metaphase plate. **A** Location of kinetochore pairs within the metaphase plate across 26 cells. **B-H** Summary statistics (medians of posterior medians and standard error) of indicated biophysical parameters partitioned into 5 groups for the average radial position within the metaphase plate. Groups are equally sized, containing the same number of observations, with the five groups defined by their radial distances, *i.e.,* $[0, 2.03]$, $(2.03, 2.95]$, $(2.95, 3.58]$, $(3.580, 4.01]$, $(4.01, 5.03]$ respectively. **B** Summary of scaled spatial trends over all parameters. **C** Pulling forces v_-, **D** Pushing forces v_+, **E** Spring constant κ, **F** Polar ejection force (PEF), **G** precision τ, **H** Natural length of the centromeric chromatin spring connecting the kinetochore sisters L. Based on 798 kinetochore pairs over 26 cells.

(larger between location variance) and α (larger between cell variance) illustrates the large variation of both within and between cells compared to the mean, Appendix Figure B4.

Parameter	Total variance	Between-cell variance	Between-location variance	Between cell/location variance	total s.d/mean
α	3.9×10^{-5}	$2.6 \times 10^{-6*}$	3.8×10^{-7}	6.856	0.498
κ	1.5×10^{-4}	$2.2 \times 10^{-5*}$	$1.8 \times 10^{-5*}$	1.177	0.563
L	7.3×10^{-4}	$1.2 \times 10^{-4*}$	$2.3 \times 10^{-5*}$	5.270	0.033
τ	3.1×10^{4}	$2.9 \times 10^{3*}$	$1.6 \times 10^{4*}$	5.474	0.240
v_-	1.8×10^{-4}	$2.7 \times 10^{-5*}$	$4.6 \times 10^{-5*}$	0.582	0.313
v_+	2.8×10^{-5}	$8.8 \times 10^{-6*}$	$1.7 \times 10^{-6*}$	5.124	0.589
p_{icoh}	1.1×10^{-2}	$1.1 \times 10^{-3*}$	$3.5 \times 10^{-3*}$	0.341	0.114
p_{coh}	2.8×10^{-4}	$5.1 \times 10^{-5*}$	$3.0 \times 10^{-5*}$	1.725	0.018

Table 4: K-fiber force variation within cells is larger than between cells. Variance contributions of the biophysical parameters, ($n = 383$ KT pairs from $N = 14$ cells to allow for at least 3 sister pairs in each group), grouping by cell and location (5 radial boxes) within the metaphase plate. The second column denotes the within-cell variance (*i.e.,* residuals), while the third and fourth columns report the within cell and location variance respectively. Parameter estimations use the model with asymmetry on v_- and v_+; the posterior median v_- and v_+ values are averaged over the two sisters. Stars denote that there is statistically significant difference ($\alpha < 0.01$) between groups of this factor. The ratio of the between cell to the between location variance is shown in fifth column and the size of effect (ratio of population parameters' standard deviation to the population parameters' (abs) mean) in last column. Stars denote the statistically different ratio at $\alpha < 0.01$. Caution: Due to low coverage of KT pairs per cell within each radius group, these results should be taken with caution as some of the ANOVA assumptions are violated. Results on 3 radial boxes give similar results, see Appendix Table A1.

2.7 K-fiber mechanical parameters are time dependent and tune towards an anaphase ready state

The metaphase plate (MPP) undergoes time-dependent maturation in RPE1 cells, including a compaction of the width along the spindle axis as anaphase onset is approached, [Embacher et al., 2022] and Figure 2; a similar decrease in MPP width is observed in HeLa cells [Jaqaman et al., 2010b]. We thus investigated whether the biophysical parameters change in time, potentially explaining MPP maturation. We modified the basic model M_0, (eq. (1)) to have time dependent parameters; we assumed time dependence is exponential this preserving the parameters sign whilst it is also a good approximation for weak linear dependence. The full time dependent model has 5 time dependent parameters, and given by,

$$\begin{aligned} X^1_{t+\Delta t} &= X^1_t - v_{\sigma^1_t,0} \cdot e^{v_{\sigma_t,1}\, t}\Delta t - \kappa_0 e^{\kappa_1\, t}\Delta t(X^1_t - X^2_t - L\cos(\theta_t)) - \alpha_0 e^{\alpha_1\, t}\Delta t X^1_t + \sqrt{\Delta t}N(0, \tau^{-1}e^{-\tau_1 t}) \\ X^2_{t+\Delta t} &= X^2_t + v_{\sigma^2_t,0} \cdot e^{v_{\sigma_t,1}\, t}\Delta t - \kappa_0 e^{\kappa_1\, t}\Delta t(X^2_t - X^1_t + L\cos(\theta_t)) - \alpha_0 e^{\alpha_1\, t}\Delta t X^2_t + \sqrt{\Delta t}N(0, \tau^{-1}e^{-\tau_1 t}) \end{aligned} \tag{4}$$

where we define for a time dependent parameter the constant term, with subscript 0, (value at the start of the movie), and rate of change parameter (on a log scale) with subscript 1. We don't analyse time dependence in switching, as there are too few switching events per trajectory, or time dependence of the centromeric springs' natural length as that is fixed from an accessory experiment (nocodazole washout) because of identifiability issues. We consider a nested sequence of models. We label models by the parameters that are time dependent, for example $M^t_{v_+}, M^t_{v_-}$ are the models with only v_+, and v_- time dependent respectively (as eq. (4)), superscript t denoting time dependent parameter models.

Inference of temporal dependence of mechanical parameters

We fitted five different models with a single time dependent mechanical parameter, $M^t_{v_+}$, $M^t_{v_-}$, M^t_κ, M^t_α, M_τ, and four multiple time varying parameter models $M^t_{v_+v_-}$, $M^t_{v_+\tau}$, $M^t_{v_-\tau}$, $M^t_{v_+v_-\tau}$, to each KT sister pair metaphase trajectory. We kept the same quality control criteria for trajectories as in the asymmetry model, *i.e.,* restricted analysis to trajectories with at least 120 time points and less than 20% missing data in metaphase. We calculated the Bayes factors to determine the significance of the time dependence of mechanical forces (See Methods). We find that a substantial proportion (46.6%) of kinetochores demonstrate significant time dependence. Specifically, there is proportion of sister pairs showing significant time dependence in v_-, *i.e.,* 20.2%, v_+, *i.e.,* 15.8%, τ, *i.e.,* 25.3%, α, *i.e.,* 6.5% and κ, *i.e.,* 1%, Table 5. This suggests that the K-fibre pulling and pushing forces and the diffusive noise are time dependent. In contrast, few kinetochore pairs show significant time dependence in the centromeric spring strength κ or polar ejection

forces α, Table 5; therefore more complex models with time dependent κ or α were not explored. Through comparison of nested models, we determined which combinations of parameters are time dependent in each sister pair giving the model preference network, Figure 8.

Preferred Model	DMSO (n=788)	Nocodazole (n=762)	Totals (n=1550)
Time invariant	421 (53.4%)	294 (38.6%)	715 (46.1%)
α	51 (6.5%)	20 (2.6%)	71 (4.6%)
κ	6 (1%)	12 (1.6%)	18/1550 (1.1%)
v_-	103 (13%)	92 (12.1%)	195 (12.6%)
v_+	40 (5%)	110 (14.4%)	150 (9.6%)
v_- , v_+	42 (5.3%)	101 (13.3%)	143 (9.2%)
τ	93 (11.8%)	78 (10.2%)	171 (11%)
$v_-\,\tau$	15 (1.9%)	27 (3.5%)	42 (2.7%)
$v_+\,\tau$	17 (2.1%)	28 (3.7%)	45 (2.9%)
$v_\pm\,\tau$	0 (0%)	0 (0%)	0 (0%)

Table 5: Temporal dependence: Numbers of pairs that preferred each temporal model for the DMSO and nocodazole washout treated cells. The total number of pairs per treatment is shown in the column header.

To determine how the K-fibre biophysical properties vary in time, we analysed the posterior median of $v_{\pm,0}$, $v_{\pm,1}$ from $M_{v\pm\tau}$ for all KTs. This model, although not preferred, incorporates the main time dependence observed in our data; for trajectories that prefer a simpler nested model the inferred rate of change for parameters that were constant in the nested model are close to zero and other inferred parameters were similar. There is significant correlation between v_{-1} and v_{-0}, ($p_{Corr} < 10^{-16}$), and similarly for v_+ and τ ($p_{Corr} < 10^{-16}$ for both parameters), with predominantly negative time dependent coefficients, 68.4 % with $v_{-1} < 0$, and similarly 70% with $v_{+1} < 0$. Thus, the magnitude of both the pulling and pushing K-fibre forces typically decrease as metaphase proceeds, and K-fibers with higher magnitude pulling (or pushing) forces decrease faster, whilst the pulling, respectively pushing forces, of K-fibers with weak pulling, pushing are strengthened. This suggests the forces are being focused towards a specific value, *i.e.,* K-fiber forces tune towards *an anaphase ready state*. This anaphase ready state corresponds to the time invariant K-fibers, *i.e.,* when $v_{1-} = v_{1+} = 0$, giving $v_{-*} = -0.033$ microns s^{-1}($sd = 0.009$), $v_{+*} = 0.003$ microns s^{-1}($sd = 0.001$) using the line of regression. Tuning is also observed in the majority of cells, for instance the same positive correlation between v_{-0} and v_{-1} is present in 26 out of 26 individual cells, with the majority (24 of 26) having a negative (and thus physical) intercept on the $v_{-1} = 0$ axis, Appendix Figure B10.

To further explore tuning, we estimated for each KT pair the forces $v_\pm(t)$ at 2 fixed reference time points, specifically at 300s prior to anaphase (in mid-metaphase) and 30s before anaphase onset (in late metaphase). The scatter plot, Appendix Figure B6, clearly shows the focusing effect, with a fixed point of $v_- = -0.04$ microns/s (with standard error (se) = 0.016 microns/s), $v_+ = 0.01$ microns/s (se = 0.009 microns/s), *i.e.,* similar estimates for the K-fiber pulling, pushing strengths of the anaphase ready state as above. This fixed point has lower energy than at mid-metaphase, *i.e.,* , the forces from mid-metaphase reduce significantly over the 5 mins to anaphase, Figure 8F,G. This is consistent with the typically negative rate of change parameters, Figure 8.

These results suggest the following temporal dynamics of v_-,

$$\frac{dv_-}{dt} = (av_- + b)\, v_-.$$

Specifically, Figure 8C implies that the average rate of change of $\log|v_-|$, v_{1-}, is correlated with v_{0-}, giving $a, b > 0$. This system has a (stable) fixed point at $v_- = -b/a$; it integrates to give the general time dependent solution:

$$\frac{1}{v_-(t)} = -\frac{a}{b} + e^{-bt}\left(\frac{1}{v_-(0)} + \frac{a}{b}\right)$$

Turning this into a discrete map, $v_-(0)$ to $v_-(t)$ for a fixed t, as Appendix Figure B6, gives a stable fixed point of this map at $-b/a$. The KT pairs with significant time dependence are in fact those with initial values further from the anaphase ready state, as shown in Table 6, and thus have a larger rate of change, and a stronger time dependence. Their time dependence is therefore easier to detect. With respect to the diffusive noise, the posterior median of τ_0 and τ_1 from $M_{v\pm\tau}$ were analysed. 125 out of 788 DMSO treated kinetochore pairs (15.9%) show significant time dependence in the

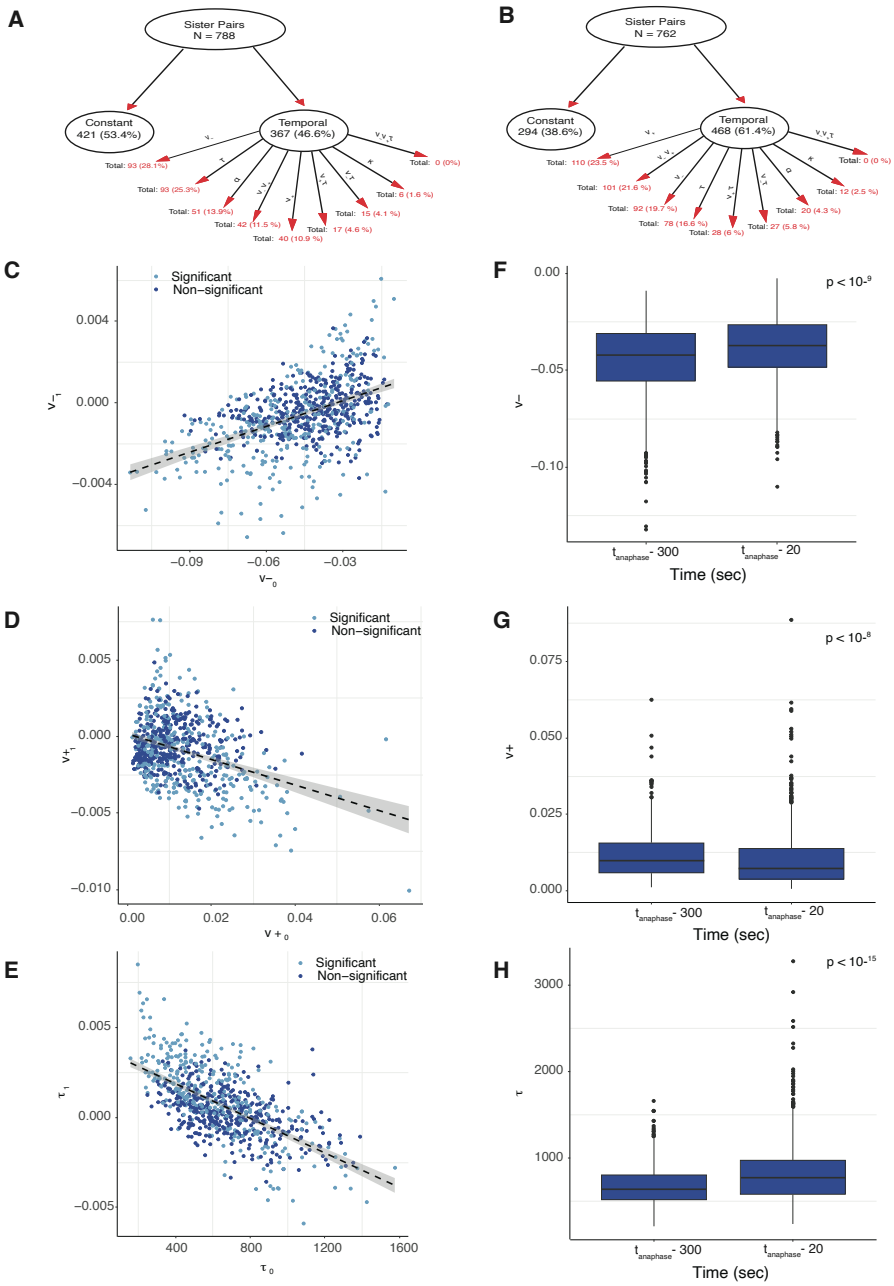

Figure 8: K-fiber forces decrease towards anaphase and are tuned towards an anaphase ready state. **A/B** Model selection summary of the temporal models over the constant-time model, on DMSO (A) and nocodazole washout (B) treated cells. A summary of each temporal models over the total number of temporal kinetochore pairs is denoted in red. **C/D/E** Scatter plot of posterior median of time dependence p_1 versus initial parameter value p_1 for **C** pushing forces, $v_{1,+}$ versus $v_{0,+}$; **D** pulling forces, $v_{1,-}$ versus $v_{0,-}$; **E** $\tau_{1,+}$ versus $\tau_{0,+}$ of DMSO treated cells. **F/G/H** Box-plots of posterior median parameter at the beginning and the end of the trajectory for **F** pushing forces v_+; **G** pulling forces v_-; and **H** noise τ of DMSO treated cells. Parameters over time (mid-metaphase to late-metaphase comparison) are statistically different ($p_{MW} < 10^{-9}, p_{MW} < 10^{-8}, p_{MW} < 10^{-16}$ for v_-, v_+, τ respectively). Finally, variances over time are statistically different with ($p_{BF} < 10^{-10}, p_{BF} < 0.02, p_{BF} < 10^{-21}$ for v_-, v_+, τ respectively). Parameters are inferred on the $M_{v\pm\tau}$ model.

	Posterior Medians			
	Time dependent KTs	Time invariant KTs	Anaphase ready state	p-value
v_{-0}	-0.052	-0.041	$v_{-*} = -0.033$	$< 10^{-8}$ $(< 10^{-7})$
v_{+0}	0.012	0.009	$v_{+*} = 0.003$	$< 10^{-4}$ (10^{-7})

Table 6: KT pairs with significant time dependence are those with initial values further from the anaphase ready state. Table shows the posterior median estimates of $v_{\pm 0}$ and $v_{\pm}$ for the the significant/non-significant time dependent KT pairs. Posterior distributions are statistically different, using one sided Kolmogorov-Smirnov (one-sided Mann-Whitney) tests. Anaphase ready state estimates from the line of regression of $v_{\pm 0}$ against $v_{\pm}$ are shown for comparison.

noise (preferring any of $M^t_{\tau}, M^t_{v_-\tau}, M^t_{v_\pm\tau}$). The noise precision of most of the kinetochore pairs (64.1%) increases which indicates that the random (diffusive) noise in KT dynamics weakens over metaphase. There is a significant correlation (negative), ($p_{Corr} < 10^{-15}$), between the time dependent coefficient (τ_1) and the initial magnitude of noise (τ_0) , which suggests, for kinetochore pairs with large noise at the beginning of the movie, that their noise typically diminishes during metaphase. Similarly, precision significantly increases from mid to late metaphase at the population level, ($p_{MW/KS} < 10^{-16}$), Figure 8H. As shown Appendix Figure B6C, the noise precision is also tuned, *i.e.,* there is an anaphase ready precision.

2.8 KT heterogeneity and trends are robust to perturbation of the spindle assembly pathway

To analyse whether the heterogeneity in space, time and random noise is robust to perturbations, we used nocodazole washout treatment to alter the spindle assembly pathway. Nocodazole disassembles microtubules, with near complete loss of microtubules after 2hrs treatment at concentration 330nM, [Sen et al., 2021]. Upon washout rapid microtubule assembly occurs and congression and segregation then follow. There is a substantial increase in merotelic attachments and segregation errors, [Cimini et al., 2001, Worrall et al., 2018], and a 3 fold increase in lazy kinetochores [Sen et al., 2021]. Lazy kinetochores are defined as KTs that significantly fall behind their cluster at any point during anaphase. At 4s time resolution, there were 0.26% lazy KTs in RPE1 cells, rising to 0.86% in nocodazole washout treated cells, Sen et al. [2021]. It is unknown which of the mechanisms that result in the normally high fidelity of segregation are disrupted under nocodazole washout treatment.

We analysed kinetochore heterogeneity in metaphase of nocodazole washout treated cells (330nM conc, 2 hr treatment followed by washout as in Sen et al. [2021]), analysing 1240 KTs in 33 cells (out of 51 imaged cells using identical cell filtering requirements to previously). In these 33 cells detection and tracking performance was similar to cells cultured in DMSO; on average we obtained 89.9 KTs per frame, and 37.6 sister pairs per cell (quartiles Q1=35, Q3=41) where both sisters were tracked for at least 200 seconds (100 frames). The videos of nocodazole washout treated cells were typically longer than those of DMSO cultured cells, 237 frames versus 181 frames.

Metaphase was similar in nocodazole washout treated cells to DMSO cultured cells; the quasi-periodic oscillations had similar period and strength (ACF depth), Figure 9, and did not vary over metaphase, Appendix Figure B1. MPP maturation over the last 5 mins was substantially weaker in nocodazole washout although still significant; this is possibly because the MPP width had already decreased 5 mins before anaphase. The reduction in the KK distance over the last 5 mins of metaphase was weak, Appendix Figure B1. The average KK distance is marginally larger in nocodazole washout treated cells (1.135 microns compared to 1.104 microns, averaged over time and KTs), and there is a stronger spatial dependence across the MPP in nocodazole washout treated cells with the KK distance increasing towards the periphery, Figure 9A. The period and oscillation strength (ACF depth) were approximately constant across the MPP in both DMSO and nocodazole washout; the 20.2% greater depth of the ACF in the MPP centre compared to the periphery (DMSO) reflects the fact that oscillations are noisier towards the periphery.

In nocodazole washout treated cells kinetochore heterogeneity and trends were similar but typically K-fibers were weaker.

1. **Biophysical parameters**. Nocodazole washout treated cells have on average weaker K-fibers, specifically the magnitude of v_+, v_- were reduced by 37.5% ($p_{MW} < 10^{-15}$), and 5.8% ($p_{MW} < 10^{-4}$) respectively, Appendix Table A3. They also have significantly reduced diffusive noise, ($p_{MW} < 10^{-15}$, the precision increased by 20%), a higher PEF ($p_{MW} < 10^{-10}$, α increased by 15%) and the spring constant is reduced by 40% ($p_{MW} < 10^{-9}$). The natural length is as exected the same as in DMSO, since the same informative prior is used. These data suggests that fewer MTs are bundled into K-fibers, leaving a higher density of spindle MTs that would explain the increase in the strength of the PEF.

2. **Spatial trends with the metaphase plate radius** were reproduced similar to DMSO, Figure 10. In nocodazole washout treated cells, K-fibre pushing (v_+), pulling forces (v_-), the spring constant (κ) and diffusive noise (τ) were reduced by 14%, 34%, 65%, 19% from middle to periphery of the metaphase plate (in nocodazole washout treated cells). Finally, unlike DMSO, we observed a statistically significant reduction of 15% of the PEF parameter α towards the periphery, ($p_{Corr}, p_{Kendall/Spearman} < 10^{-3}$).
3. **Sister asymmetry** was similar with 28.5% having significant asymmetry. There was an identical anti-correlation between the strength of pulling and pushing forces, Figure 5, and Appendix Figure B11, and sister differences were identical to differences between random KTs. The lateral organisation transverse to the MPP into strong/weak asymmetric and symmetric KT groups was also reproduced, Figure 6B,D,F,H,J.
4. **Temporal trends** were very similar, Figure 8B, Table 5, in fact there was a reduction in the preference for the time invariant model (53.4% DMSO to 46.1% nocodazole washout), likely due to the typically longer time series and the reduced diffusive noise under nocodazole washout, both increasing the ability to detect temporal variation. Significant temporal dependence was primarily seen in $v_\pm, \tau$ as before, with preferences for temporal dependence in v_- (24.5%), v_+ (21.7%), τ (16.6%), whilst preference for temporal dependence in the other parameters is infrequent, Table 5. The correlation between the rate parameters and the initial parameter value was similar, Appendix Figure B12 suggesting that K-fibers in nocodazole washout treated cells also tune towards an anaphase ready state. The anaphase ready state has slightly lower pulling force (magnitude) and pushing forces, (-0.02, 0.003) compared to (-0.04, 0.01) microns/s in DMSO, with this difference being statistically different ($p_{MW/Ztest} < 10^{-20}$). As before the K-fibre reduction in pulling/pushing force magnitudes over the last 5 mins of metaphase is significant ($p_{MW/KS} < 10^{-16}, p_{MW/KS} < 10^{-9}$ for v_-, v_+ respectively). There is little increase in the precision over that period, Appendix Figure B7 and Appendix Figure B12, whereas the precision increased in DMSO, Figure 8. This is possibly explained by the higher precision on all inferred models in nocodazole washout treated cells, Figure 10, Appendix Figure B7 and Appendix Table A3, possibly limiting any further increase. We confirmed that this higher precision isn't due to differences in movie length (reducing the length of movies had little effect on mean (median) estimates) as expected.

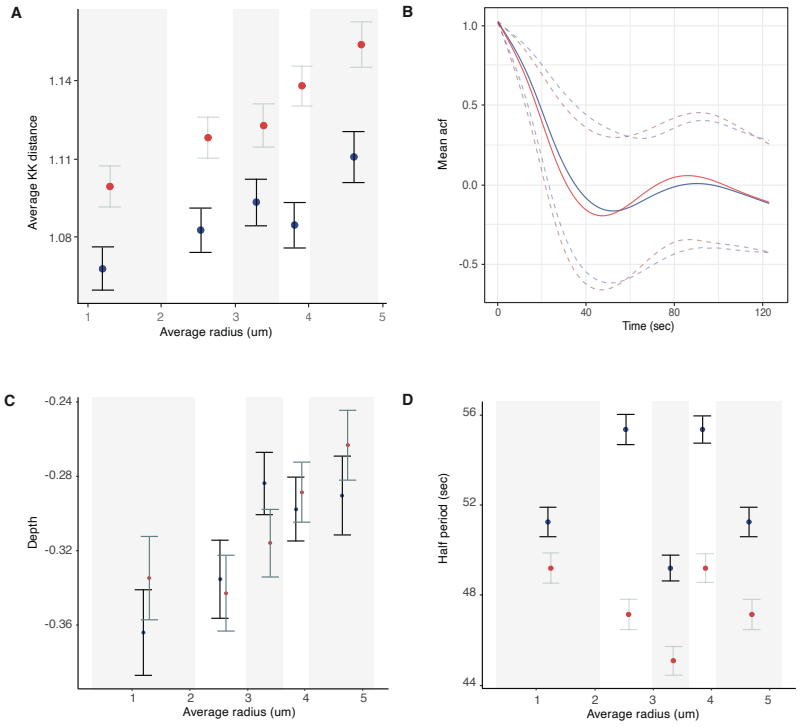

Figure 9: Quasi-periodic oscillation period and strength are constant across the MPP and robust to perturbation. **A** Sister Kinetochore distance across the metaphase plate. **B** Mean autocorrelations for DMSO (blue) and nocodazole washout (red) treated cells. Gray lines denote the 5% and 95% percentile. **C** Average depth (ACF minimum) and **D** oscillation period for sister pairs across the metaphase plate.

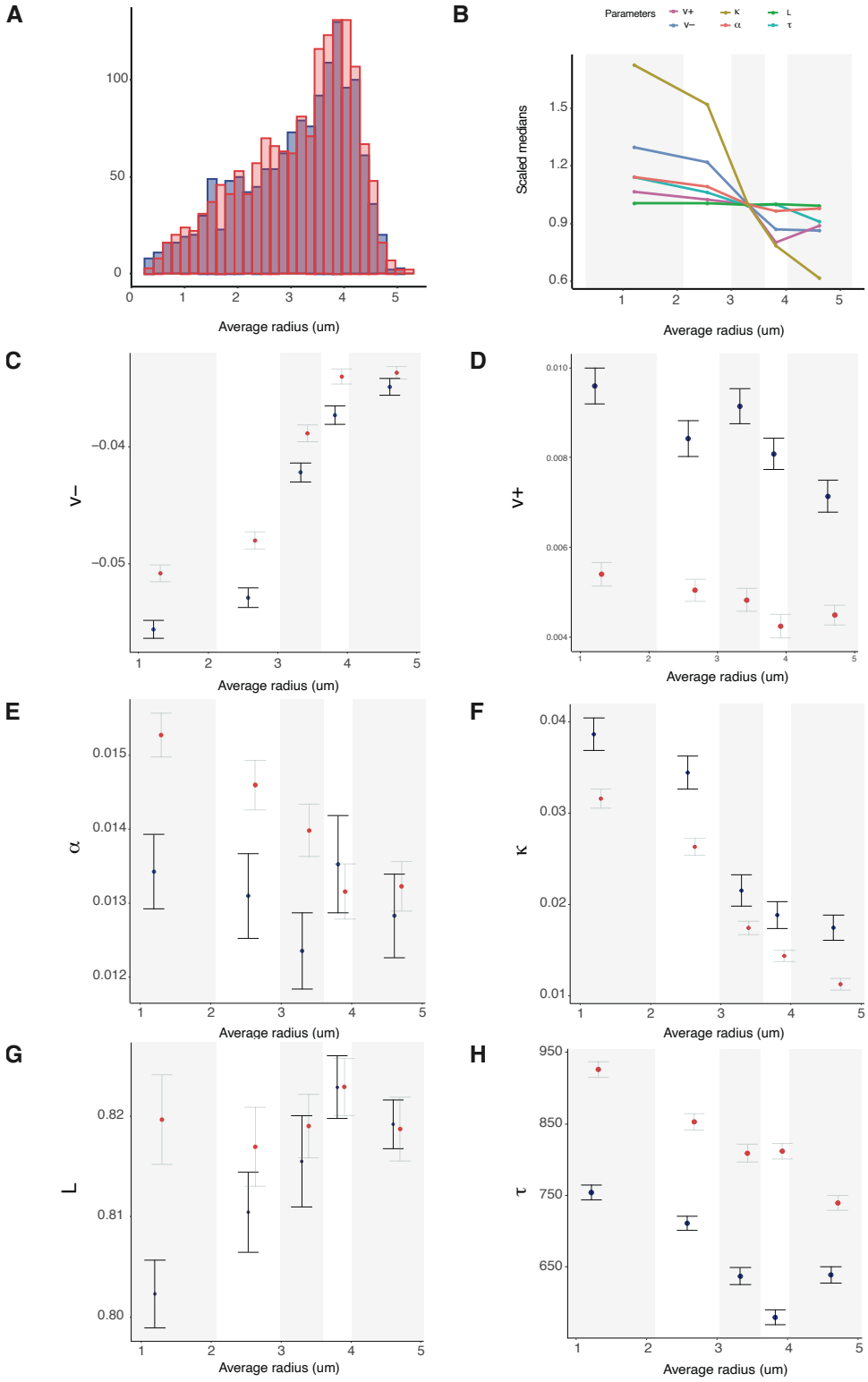

Figure 10: Comparison of spatial mechanical parameter trends across the metaphase plate for DMSO (blue) and Nocodazole (red) treated cells. *Caption continues.*

Figure 10 continued. **A** Location of DMSO (blue) and nocodazole washout (red) treated kinetochore pairs within the metaphase plate, based on 798 and 984 kinetochore pairs respectively, over 59 cells. **B-F** Summary statistics of indicated biophysical parameters partitioned into 5 groups for the average radial position within the metaphase plate. Groups are equally sized, containing the same number of observations (DMSO and nocodazole washout treated cells), with the five groups defined by their radial distances, *i.e.,* $[0, 2.07]$, $(2.07, 2.97]$, $(2.97, 3.59]$, $(3.59, 4.01]$, $(4.01, 5.20]$ respectively. Hence, the groups' margins are not identical to groups of Figure 7. **B** Summary of scaled spatial trends over all parameters for nocodazole washout treated cells, in reference to Figure 7. **C** Pulling forces v_{-}, **D** Pushing forces v_{+}, **E** PEF, **F** Spring constant κ, **G** natural length of the centromeric chromatin spring connecting the kinetochore sisters L, **H** precision τ.

2.9 Anaphase onset time is heterogeneous

Our analysis suggests the existence of mechanisms that tune K-fibers as anaphase is approached, most predominately tuning the pulling force and reducing diffusive noise. This raises the question of how such tuning benefits segregation and if we can detect dynamic differences in anaphase in a perturbed mitosis. At anaphase the sister pairs separate, with 2 clusters of KTs approaching respective poles. These clusters separate at the same speed in DMSO and nocodazole washout treated cells, Figure 11A, although nocodazole washout treated cell clusters spread substantially compared to DMSO, that have approximately constant cluster width, Figure 11B. Although K-fibers are depolymerising in anaphase, we observed occasional reversals in individual KT trajectories, whereby a short reversal of direction occurs, Figure 11C. The frequency of reversals in nocodazole washout treated cells was substantially higher than in DMSO, with 50.8% (471 out of 927) of KTs having a reversal (by eye), compared to 22.7% of reversals in DMSO. Thus, anaphase dynamics is perturbed under nocodazole washout.

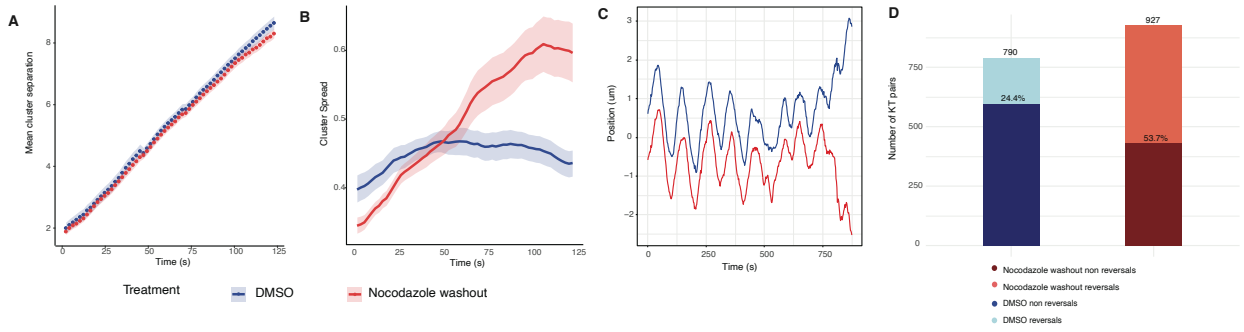

Figure 11: Anaphase clusters for DMSO (blue) and nocodazole washout (red) treated cells. Time $t = 0$ marks the median of estimated anaphase onset time per cell. **A** Mean cluster separation. Shaded areas denote the standard errors. **B** Cluster spreads during time and left axis based on 699 DMSO treated (blue) and 644 nocodazole washout treated (red) KT-pairs, which had long enough anaphase time points. **C** Example of a sister pair trajectory with reversals in anaphase. **D** Summary of KT-pairs with reversals and no reversals in DMSO (blue) and nocodazole washout cells (red). From 790 (927) KT-pairs 611 (465) pairs had no reversals, *i.e.,* 77.3% (49.2%) for DMSO (nocodazole washout treatment).

Anaphase transition model

To analyse anaphase further, we extended the asymmetric model (eq. (2)) to incorporate anaphase dynamics and an anaphase transition event, implemented similar to the metaphase-anaphase model in Sen et al. [2021]. Specifically, we introduce an additional hidden state, A, the anaphase state with dynamics given by,

$$\begin{aligned} dX_t^1 &= v_A^1 dt + s^1 dW_t^1, \\ dX_t^1 &= -v_A^2 dt + s^2 dW_t^2, \end{aligned} \tag{5}$$

where v_{A}^k, s^k are sister k's velocity and diffusion coefficient in anaphase. Since the sisters are no longer connected the spring forces are removed, whilst the velocity in anaphase may be different to the depolymerising K-fibre velocity. We also removed the PEF since it decays over anaphase, although the decay dynamics is unknown. Our model is only appropriate for the part of anaphase when the speed is approximately constant and the separation between the descending KT clusters is not too large, since as they approach the poles they slow down. We only fitted the model to

linear regions (truncating movies if there were signs of slow down). Anaphase portions were around 50 frames, enough to infer the anaphase speed and anaphase onset time.

The transition to anaphase is modelled as a smooth switch with a transition probability to A at time t given by,

$$p_{\mathrm{A}}(t) = \frac{1}{1+\exp\left(-\left(t-t_{\mathrm{A}}\right)/\beta\right)}.$$

Thus, the transition to anaphase occurs around time t_{A} with $\beta = \Delta t/2$ (fixed) determining the range over which switching can occur. We assume the anaphase state A is equally accessible from each of the other states, but transitions back from anaphase to metaphase are not possible, *i.e.,* state A is absorbing. Thus, once anaphase onset occurs the chromosomes segregate.

Switches between hidden states (see Figure 3B) occur at each time step according to the time dependent transition matrix (state order as eq. (7), with the anaphase state A in the last column/row),

$$\mathbf{P}(t) = \begin{bmatrix} p_{icoh}p_{icoh}q_{\mathrm{A}}(t) & p_{icoh}q_{icoh}q_{\mathrm{A}}(t) & p_{icoh}q_{icoh}q_{\mathrm{A}}(t) & q_{icoh}q_{icoh}q_{\mathrm{A}} & p_{\mathrm{A}}(t) \\ p_{coh}q_{coh}q_{\mathrm{A}}(t) & p_{coh}p_{coh}q_{\mathrm{A}}(t) & q_{coh}q_{coh}q_{\mathrm{A}}(t) & p_{coh}q_{coh}q_{\mathrm{A}} & p_{\mathrm{A}}(t) \\ p_{coh}q_{coh}q_{\mathrm{A}}(t) & q_{coh}q_{coh}q_{\mathrm{A}}(t) & p_{coh}p_{coh}q_{\mathrm{A}}(t) & p_{coh}q_{coh}q_{\mathrm{A}} & p_{\mathrm{A}}(t) \\ q_{icoh}q_{icoh}q_{\mathrm{A}}(t) & p_{icoh}q_{icoh}q_{\mathrm{A}}(t) & p_{icoh}q_{icoh}q_{\mathrm{A}}(t) & p_{icoh}p_{icoh}q_{\mathrm{A}} & p_{\mathrm{A}}(t) \\ 0 & 0 & 0 & 0 & 1 \end{bmatrix}$$

with $q_{coh} = 1 - p_{coh}$ and $q_{icoh} = 1 - p_{icoh}$ as before, and $q_{\mathrm{A}}(t) = 1 - p_{\mathrm{A}}(t)$, where p_{coh} and p_{icoh} are the probabilities of a kinetochore remaining in the coherent, respectively incoherent state over a time interval Δt, and p_A is the probability of transition to the anaphase state, A.

Inference of anaphase parameters

We fitted the anaphase model to 790 KT pair trajectories (out of 798 pairs, 91.9%) with at least 20 frames in anaphase, from 26 cells cultured in DMSO. The inference algorithm for this metaphase-anaphase model displayed more divergences than our base model, rising to 3% and reducing the analysable KT-pairs to 767. In addition, as this model doesn't incorporate reversals that would reduce the inferred anaphase speed, we filtered out the KT pairs which had reversals during anaphase by visual inspection. Hence, we report the fitting of the anaphase model to 611 KT pairs (of 767 pairs, 79.7%) in DMSO.

Inference of the anaphase model on nocodazole washout treated cells, (eq. (5)), had more divergences than in DMSO, *i.e.,* 835 out of 927 pairs had no divergences, (90.1%) in nocodazole washout, compared to 767 out of 790 (97.1%) in DMSO, consistent with the higher frequency of reversals under nocodazole washout treated cells, Figure 11D. We filtered out KT pair trajectories with reversals leaving 456 KT pairs (from 30 cells) for which the inference is reliable. Anaphase dynamics in nocodazole washout treated cells was similar to DMSO based on the reversal free trajectories, Appendix Figure B15, with similar dispersion of anaphase onset times, and similar anaphase speeds.

An example of anaphase inference on an experimental trajectory is shown in Figure 12A, where both anaphase timing and the anaphase speed are inferred with high confidence and consistent with expert judgement. Within a cell we observe substantial variation in anaphase timing of KTs, Figure 12B, with an average standard deviation of 10.3 secs (range 5 secs to 32 secs) across the 26 cells. Anaphase timing did not vary over with MPP location Figure 12E, $p_{Corr} = 0.38$. The average anaphase speed was typically smaller than the average depolymerisation speed, specifically being 67% of the depolymerisation speed on average. This is expected since the model ignores the PEF in anaphase, and the depolymerisation force typically decreases towards anaphase whilst we are comparing v_a to the average metaphase force v_-. There is a weak correlation between v_- and v_a ($\rho = 0.17$, $p_{Corr} < 10^{-15}$), Figure 12F, although there is no trend in v_a across the MPP (Figure 12C), which is in stark contrast to the strong decrease in the strength of the depolymerisation force with r. The only correlations of note are that the anaphase speed of sisters is correlated ($\rho = 0.39$, $p_{Corr} < 10^{-15}$), Figure 12H, and there is positive correlation ($\rho = 0.247$, $p_{Corr} < 10^{-9}$) between anaphase speed and anaphase time relative to median anaphase time, *i.e.,* sisters with a later transition to anaphase have a higher anaphase speed. Similar results were obtained if reversals were not filtered out, data not shown.

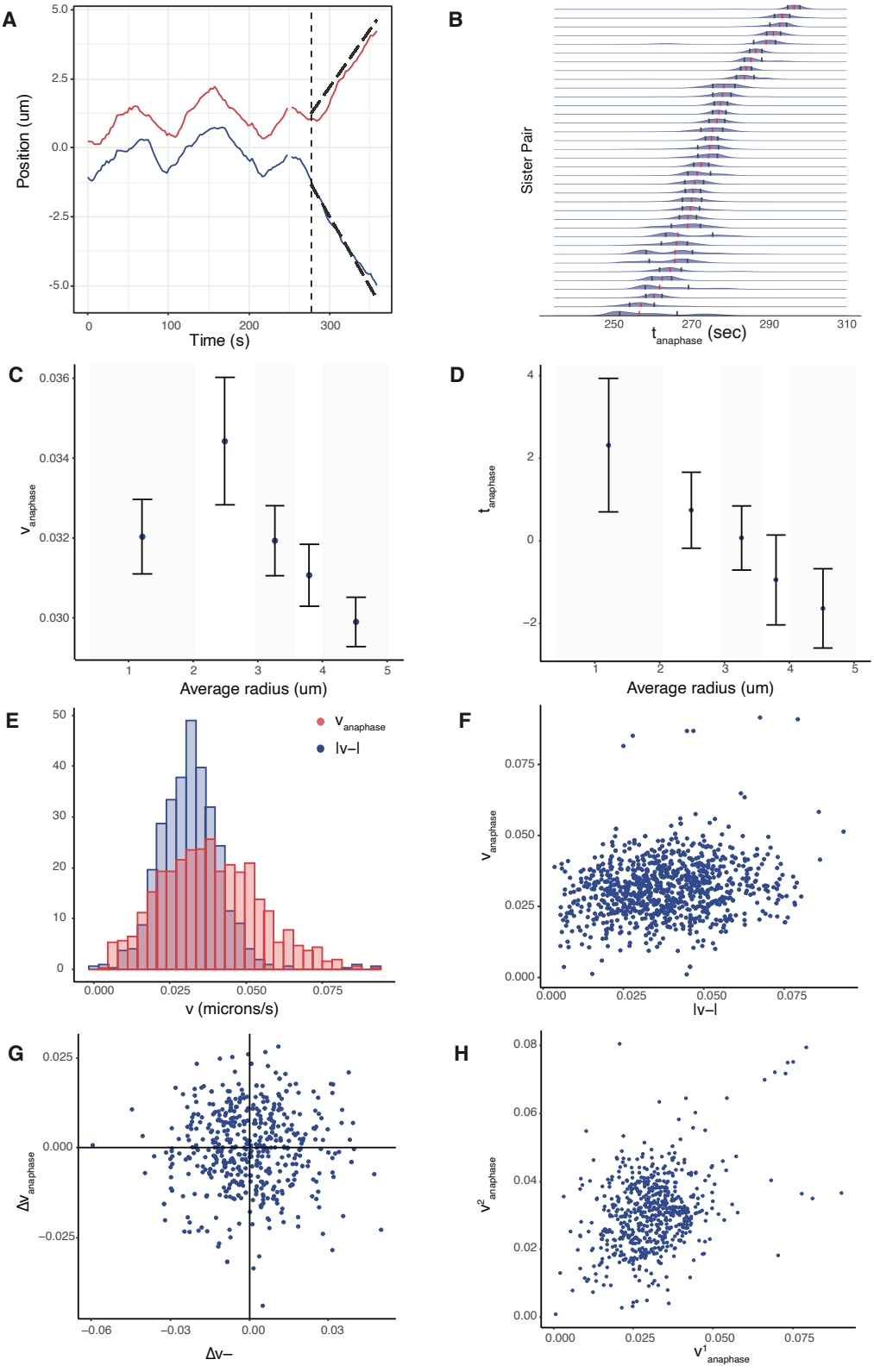

Figure 12: Anaphase K-fibers are dynamically homogeneous across the MPP despite variation in anaphase initiation. *Caption continues.*

Figure 12 continues **A** Example of the anaphase inference on a KT sister pair trajectory with anaphase event indicated with vertical line, and dashed lines above/below anaphase trajectory have gradients of v_a^k. **B** Anaphase timing of KT pairs in an individual cell. Red dots denote the distribution median, while the blue dots define the interquartile range **C/D** Spatial biophysical parameter trends across the metaphase plate for anaphase speed/anaphase timings (relative to the median anaphase time per cell). The estimated correlation between anaphase speed and anaphase timings is 0.247 ($p_{Corr} < 10^{-9}$). **E** Estimated densities of $v_{anaphase}$ (red) and pulling force (blue), (normalised by the drag coefficient). **F** Correlation of anaphase speed and absolute v_- (estimated correlation = 0.174, $p_{MW} < 10^{-15}$). **G** Difference of $v^1_{anaphase}$ and $v^2_{anaphase}$ versus v^1_- and v^2_- only on asymmetric (on v_-) sister pairs. No statistically significant correlation is observed. **H** Correlation of anaphase speeds for sister 1 and sister 2 (estimated correlation 0.386, $p_{Corr} < 10^{-15}$). These figures are based on a subset of KT pair trajectories ($N = 611$ from 26 cells cultured in DMSO), which exhibited no reversals during anaphase (visual inspection), had adequate coverage of anaphase.

3 Discussion

In this work we developed a pipeline for the study and analysis of KT dynamics at the cell level, revealing spatial organisation both within and transverse to the MPP, and intrametaphase temporal variation in untransformed human cells (RPE1). Our pipeline comprises high resolution LLSM imaging, image processing (segmentation/KT detection, tracking and pairing), biophysical parameter inference and evidence based data driven modelling to comprehensively assess the sources of KT dynamic heterogeneity in cells. LLSM uses an ultra thin sheet of light to limit effects of phototoxicity and photobleaching, [Chen et al., 2014], which allows high temporal resolution imaging (2.05 s/frame) in 3D over long timescales. We improved our previous tracking software (KiT, [Harrison et al., 2022]) to achieve near complete detection and tracking, see Methods and [Daniyan et al., 2024]. Finally, we developed a suite of 18 KT-pair mechanistic models that incorporate sister asymmetry and time dependent mechanical parameters, generalising the symmetric, time invariant parameter model of Armond et al. [2015a], and used model selection methods to assess the evidence for sister asymmetry and parameter time dependence. We fitted these models to KT-pair trajectories of 59 cells: 1596 KTs from 26 cells in DMSO, 1240 KTs from 33 cells in nocodazole washout treated cells, and used model selection methods to determine the support for asymmetry and temporal dependence. We reported results on the vanilla model of Armond et al. [2015a], 4 asymmetric models, 9 temporal models (3 other models were not discussed since support was negligible) and a metaphase-anaphase model. Our analysis demonstrates substantial heterogeneity in KT dynamics within a cell, summarised in Figure 13. Specifically, KT dynamics vary in time ($v_\pm, \tau$), demonstrating tuning towards an anaphase ready state, and spatially, both within the MPP ($v_\pm, \kappa, \tau$) and transverse to the MPP (caused by random sister asymmetry in v_-). In addition, observed that oscillations towards the periphery become more stochastic because of an increasing diffusive noise, a change in oscillation quality that is also seen PTK cells [Civelekoglu-Scholey et al., 2013], and an increase in the dynamic switching time (time to switch both sisters), Figure 10, Table 4. Perturbing the spindle self-assembly pathway (nocodazole washout) gave similar results indicating that the processes governing spatial, temporal and random noise are intrinsic to mitosis; specifically dynamics and levels of heterogeneity were nearly identical except for a weakening of K-fibers, and an increased PEF that also acquired variation within the MPP.

The majority of the parameter variation we report can be related to the K-fibers, Figure 13. Specifically, we observed strong trends in the K-fiber force strength across the MPP, with both the pulling and pushing forces decreasing towards the periphery (38% and 25% respectively), we observed sister pulling force asymmetry that resulted in KT lateral organisation across the MPP, and a decay of the pulling and pushing forces in the last 5 mins of metaphase. MT polymerisation in K-fibers will likely contribute substantial active noise, [Gnesotto et al., 2018], thus the variation in diffusive noise in space and time probably reflects changes in MT dynamics and/or cohesion of K-fibers, rather than a change in chromosome diffusion coefficients. What causes this spatial and temporal variation in K-fiber dynamics is unknown, but there are known mechanisms that could generate heterogeneity. Specifically,

- The spindle is not a homogeneous environment with high levels of geometric and force variation transverse to the spindle axis. Specifically, there is substantial changes in spindle geometry towards the periphery and bridging fibers connect the spindle poles that can exhibit high curvature, [Vukušić et al., 2017, Kajtez et al., 2016, Miles et al., 2022], whilst bridging fibers are also under much higher compressive forces towards the periphery compared to central K-fibers, [Pavin and Tolić, 2020]. The spatial dependence of the K-fiber properties ($v_\pm, \tau$) within the MPP may therefore be a consequence of adaptation to this changing geometry.
- Chromosome size and centromere size varies between chromosomes, and in particular, large chromosomes tend to be localised towards the periphery, [Mosgöller et al., 1991, Booth et al., 2016]. Both centromere differences between chromosomes [Dumont et al., 2020] and kinetochore size [Drpic et al., 2018] have been implicated in biasing chromosome segregation errors, whilst chromosomes 1 and 2 (the 2 largest chromosomes) have a

higher mis-segregation rate [Worrall et al., 2018]; these biases must be a result of a mechanical dependence on size, which may be related to the within MPP trends we observe.

- Our asymmetric models indicate that random variation is responsible for KT heterogeneity within a cell, particularly in $v_{\pm}, \tau$, with variation in v_{-} between sisters giving rise to lateral organisation of KTs in the MPP, Figure 13. This random variation in K-fiber properties could be a result of outer KT assembly at nuclear envelope breakdown (NEBD), [Navarro and Cheeseman, 2021], or self-assembly of the K-fibers and spindle during prometaphase, which will introduce variation in K-fiber composition, bundle coherence, [Armond et al., 2015b], and/or control processes. However, since there is an inherent anti-correlation in K-fibre pulling and pushing forces, Figure 5B, bundle size (MT count) is unlikely to be responsible as this would be expected to increase both pushing and pulling forces. This is also suggested by the fact that the random variation in KT pulling forces does not correlate with anaphase pulling forces, which would be expected if related to MT composition. Thus, control processes are more likely. K-fibers are in different states in metaphase and anaphase, with substantial phosphorylation occurring at anaphase, thus any heterogeneity in control processes will not transfer into anaphase dynamics.

We hypothesise that the temporal intrametaphase changes in K-fiber dynamics that we observe are due to a regulatory process that prepares the system for anaphase. Intrametaphase molecular changes in the KT or K-fibers that could underpin this regulatory process, or these changes in the biophysical parameters have not been reported, more likely reflecting the fact that quantification is difficult given the need to accurately time metaphase progress on a minute time scale.

We also observed spatial trends in the centromeric spring constant κ, the stiffness decreasing 53% from the centre to the periphery of the MPP. Our model assumed a linear spring, although nonlinearity has been reported, stiffness increasing with extension, [Stephens et al., 2013, Harasymiw et al., 2019]. However, since the spring extension increases towards the periphery, Figures 9 and 13, nonlinearity is not the cause of variation with radial distance r, in fact it would give an opposite trend. Centromere size could potentially affect the spring stiffness but data on centromere size variation within the MPP isn't available, and the change in κ over the MPP is substantial suggesting it arises from a direct dependence on r, for instance from the change in the spindle geometry. The inferred spring constant in all our models, and Harasymiw et al. [2019], is an effective spring constant, so this must be considered as a possible cause. The centromeric spring models the connecting chromatic material between the sister chromatids, a composite material with likely anisotropic elasticity. There are two clear effects that might affect the effective spring constant upon moving towards the periphery. Firstly, a geometrical effect, with K-fibers not being aligned with the spindle axis, Figure 13, increasing the sister-sister distance would then also comprise a shear, and if shear is energetically inexpensive the effective spring constant would decrease towards the periphery. Secondly, chromosome arms take up a different geometry towards the periphery, being pushed outwards relative to the KTs. Therefore, again, anisotropy in the chromatic material may play a role as sister-sister extension likely impacts on the material differently as the arm location varies.

The onset of anaphase, when kinetochore pairs begin to separate and segregate towards their respective spindle poles is tightly controlled temporally, [Holt et al., 2008], and appears entirely synchronous at low time resolution, but is in fact asynchronous, Figure 12B, (previously reported for RPE1 cells in Armond et al. [2019], Sen et al. [2021]). Peripheral sister-chromatids initiate anaphase earlier than central sister-chromatids by 4s in RPE1 cells, and have a lower anaphase speed, Figure 12C,D (there is positive correlation ($\rho = 0.247$, $p_{Corr} < 10^{-9}$) between anaphase speed and relative anaphase time). Further, we observed a weak correlation between the depolymerisation speed v_{-}^{k} and v_{a}^{k}, $\rho = 0.174$, $p_{Corr} < 10^{-15}$, Figure 12F, thus although our estimated anaphase force (our model ignoring PEF in anaphase) is the same order as the K-fiber pulling forces in metaphase, there is only a weak correlation between K-fiber pulling in metaphase and anaphase, whilst spatial trends in the MPP are distinctly different. This likely reflects the fact that K-fibers in metaphase and anaphase are regulated by different mechanisms and the KTs are in different states, although it is also reminiscent of the anaphase speed governor, [Anjur-Dietrich et al., 2021]. K-fibers in metaphase undergo dynamic instability and rarely have high coherence between MTs in the bundle, [Armond et al., 2015b], whilst anaphase K-fibers depolymerise for extended periods and high coherence is expected. However, we do observe a fraction of KTs undergoing transient reversals of the usual poleward motion during anaphase, Figure 11. These reversals were reported in previous studies, [Skibbens et al., 1993], whilst metaphase-like chromosome oscillations have been shown to persist into anaphase upon inhibition of protein dephosphorylation, [Su et al., 2016]. The cause of these reversals is not understood, but suggests that coherence of microtubules within anaphase K-fibers may be dependent on factors that are perturbed under nocodazole washout, potentially the efficacy of dephosphorylation.

The KT clusters (that descend to respective poles) exhibit a decrease in their spread over metaphase in DMSO, whilst are in fact tighter in nocodazole washout treated cells throughout metaphase, *i.e.,* metaphase cluster width is 0.467 microns in DMSO while the width in nocodazole washout is significantly lower, 0.353 microns ($p_{MW} < 10^{-15}$, one-sided). We observed a statistically significant reduction in spread from mid to late metaphase, *i.e.,* 0.468 to 0.414 microns in

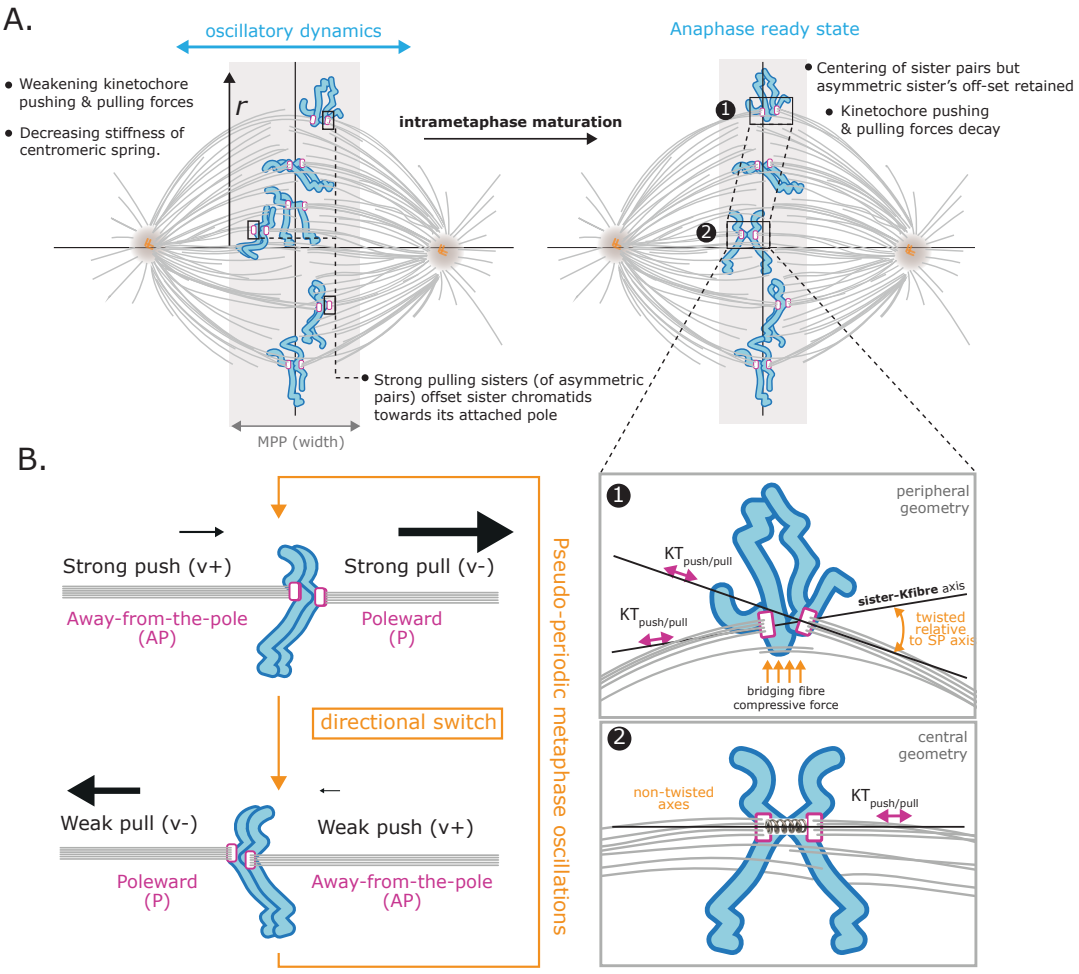

Figure 13: Organisation of the KT population within (radially) and transverse (laterally) to the MPP. **A** Left. Schematic of the spindle showing microtubules, bridging fibers, KTs (magenta) and chromosome arms (cyan). K-fiber pulling and pushing forces decay with radial distance (r), while the centromeric spring stiffness decreases. Strong pulling sisters of asymmetric pairs offset the sister pair towards its pole. Right. Late metaphase organisation after intrametaphase temporal tuning. The anaphase ready state has more centred chromosomes, and the K-fibre pulling and pushing forces typically decay. Sister chromatid offset is retained, but decreased. Annotated chromosomes at the periphery, (1), and central, (2), are shown in detail (lower panel), emphasising how the different local spindle geometry impacts attachment force orientation. **B** Schematic representation of forces in an asymmetric sister pair through the directional switching cycle (orange) of metaphase oscillations. Magnitude of the force is indicated by size of arrow. Schematic shows the inverse correlation between pulling and pushing strength of a K-fibre, whilst pulling forces are substantially larger than pushing forces.

DMSO and from 0.351 to 0.321 in nocodazole washout ($p_{MW} < 10^{-15}$, one-sided). Descending clusters are organised laterally with weak pulling KTs on the inside, and strong pulling KTs on the outside, Figure 13. This ordering was preserved from mid to late metaphase in both DMSO and nocodazole washout, Appendix Figure B16D,E, Appendix Figure B17D,E, ($p_{KS} \geq 0.998$, DMSO and $p_{KS} \geq 0.829$ nocodazole washout), suggesting that the tuning towards the anaphase ready state does not affect poleward bias of these groups and is operative in nocodazole washout. KT group order is also weakly preserved through to anaphase, Appendix Figure B16F, Appendix Figure B17F. However, anaphase is not robust to nocodazole washout, showing a substantial increase in average cluster spread from 0.345 to 0.610 microns (*i.e.,* 77% increase) within the first 60 frames from anaphase onset, Figure 11B, whilst DMSO cluster size varies within a 17.5% tolerance (minimum to maximum mean cluster size). Finally, as in DMSO, anaphase speed and relative anaphase time are significantly positively correlated $\rho_{noc} = 0.125$ ($p_{Corr} < 10^{-3}$), but significantly weakened compared to DMSO $\rho_{DMSO} = 0.247$, ($\rho_{noc} < \rho_{DMSO}$ is significant, $p_{Ztest} = 0.004$).

Our analysis suggests that metaphase dynamics are robust to changes in the spindle environment. Specifically, despite the substantial variation in K-fibre length and composition across the MPP, Novak et al. [2018], qualitatively similar dynamics occurs throughout the plate indicating mechanism robustness, in fact the strength of oscillations and the period are essentially invariant across the MPP, Figure 9. This robustness is of course already well documented, quasi-periodic oscillations being observed in different human cell lines, [Jaqaman et al., 2010b, Armond et al., 2015a], and conserved across species. Our results are also robust to perturbation of spindle assembly under nocodazole washout treatment; we saw practically identical trends in biophysical parameters in space (across the MPP) and in time (intrametaphase tuning), both effects also being observed in individual cells, Appendix Figure B11. The only differences of note in nocodazole washout were a stronger PEF, weaker K-fibers (lower $|v_{\pm}|$), lower levels of diffusive noise, and tuning towards a less active state (with lower $|v_{\pm *}|$). We hypothesise that K-fibers comprise fewer MTs in nocodazole washout, so are weaker but more coherent, thus reducing active noise contributions to the inferred diffusion. Correspondingly the density of MTs is higher in the spindle explaining the higher PEF.

Our data driven analysis suggests that the model that should be used for analysis of human KT dynamics is (sister k),

$$X^k_{t+\Delta t} = X^k_t - \left(v_{\sigma^k_t,*} + \left(v^k_{\sigma^k_t,0} - v_{\sigma^k_t,*} \right) e^{v^k_{\sigma^k_t,1} t} \right) \Delta t - \kappa \Delta t \left(X^1_t - X^2_t - L\cos\left(\theta_t\right) \right) - \alpha \Delta t X^k_t + \sqrt{\Delta t} N \left(0, \left(\tau^k e^{-\tau^k_1 t} \right)^{-1} \right), \tag{6}$$

where $v_{\pm,*}$ is the anaphase ready state, although time resolution, spatial resolution and signal to noise will impact the ability to infer all these processes. Further work is required to confirm support for this joint asymmetric, temporal model, and determine whether it is identifiable, and the requirements on time and spatial resolution to do so. This is a model for individual KT pairs. There is also substantial variation in biophysical parameters with metaphase plate position, although we have not determined the functional form of this variation. This could be inferred using Gaussian process modelling.

Our results are dependent on our models capturing the key mechanical processes driving KT dynamics. Our data driven modelling approach has demonstrated that fundamental properties of KT biophysical behaviour can be extracted, so although we have used simple models that match the data complexity, they have powerful knowledge generating capability. Further improvements may be possible. Our models are in 1D, with K-fiber forces assumed to lie along the axis. In practice, there is slight curvature of the trajectories in metaphase as they track the spindle geometry, so $v_{\pm}$ may be underestimated towards the periphery. Extending to 3D should be possible. The impact of bridging fibers on KT dynamics is also unknown. However, acute removal of PRC1, which weakens such fibers, does lead to changes in sister kinetochore tension and orientation, [Jagrić et al., 2021]. Our model for drag forces may also be too simplistic since the spindle behaves as a visco-elastic anisotropic material, [Shimamoto et al., 2011]. Assessing the impact of this visco-elasticity, and the spindle structure more generally on KT dynamics, would require rheology experiments in association with KT tracking. Interactions between kinetochore pairs, [Vladimirou et al., 2013] can also be incorporated. As regards anaphase, our model is extremely simple and ignores the complexity of the synchronised switching of KTs to depolymerisation and the release of cohesin. Further, how the PEF alters during anaphase is totally unexplored.

This study provides unprecedented detail and analysis of the behaviour of the complement of kinetochores within a cell and the temporal-spatial trends in their dynamics. Our analysis emphasises that kinetochore behaviour is highly variable within a cell implying that the dynamics of the chromosomes should be viewed in the context of the mechano-chemical machinery of the spindle rather than in isolation. Our methods, and the comprehensive characterisation of individual KTs that is achievable, should prove invaluable when comparing cell phenotypes, [Pargett and Umulis, 2013], and interpreting perturbations, be it genetic or through application of drugs. Thus, our methodology will allow mechanistic hypotheses to be evaluated with high precision. This work sets the stage for future work to quantitatively analyse

the whole of mitosis at the cell level, from nuclear envelope breakdown through to telophase. **Acknowledgements.**

We gratefully acknowledge the initial work and software development by Jonathan Harrison.C.K., A.V.I, A.D. were supported by BBSRC (BB/R009503/1), and A.D., A.D.M. were supported by a Wellcome Senior Investigator Award (grant 106151/Z/14/Z).

4 Methods and Materials

Code

The trajectory data and original code used to produce the results reported in this work are available at Github, `https://github.com/ckoki21/MetaAnaDynamics.git`. Any additional information required to re-analyze the data reported in this paper is available from the lead contact upon request.

Cell culture and generation of cell lines

Immortalized (hTERT) diploid human retinal pigment epithelial (RPE1) cell line (MC191), expressing endogenously tagged Ndc80-eGFP, was generated by CRISPR-Cas9 gene editing, [Roscioli et al., 2020]. hTERT-RPE1 cells were grown in DMEM/F-12 medium containing 10% fetal bovine serum (FBS), 2 mM L-glutamine, 100 U/ml penicillin and 100 mg/ml streptomycin (full growth medium); and were maintained at 37ºC with 5% CO_2 in a humidified incubator.

Live cell imaging by lattice light sheet microscope

The lattice light sheet microscope (LLSM), [Chen et al., 2014], used in this study was manufactured by 3i (https://www.intelligent-imaging.com). Cells were seeded on 5 mm radius glass coverslips one day before imaging. On the imaging day, each coverslip was transferred to the LLSM bath filled with CO_2-independent L15 medium, where live imaging takes place. All imaged cells entered anaphase, which is a suitable proxy for a lack of phototoxicity effects, [Jaqaman et al., 2010b]. The LLSM light path was aligned at the beginning of every imaging session by performing beam alignment, dye alignment and bead alignment, followed by the acquisition of a bead image (at 488 nm channel) for measuring the experimental point spread function (PSF). This PSF image is later used for the deconvolution of images. 3D time-lapse images (movies) of Ndc80-eGFP were acquired at 488nm channel using 1% laser power, 20 ms exposure time/z-plane, 75 z-planes, 307 nm z-step and 0.5 s laser off time, which results in 2 s/z-stack time/frame. Acquired movies were de-skewed and cropped in XYZ and time, using Slidebook software in order to reduce the file size. Cropped movies were then saved as OME-TIFF files in ImageJ.

Tracking

Kinetochore tracking is performed using the software package KiT v3.0. The tracking algorithm proceeds by detecting candidate spots via a constant false alarm rate (CFAR) detection method, [Daniyan et al., 2024], to set a KT-wise dynamic threshold on per image frame in a movie. Candidate spot locations are refined by fitting a Gaussian mixture model. Spot locations are linked between frames by solving a linear assignment problem, with motion propagation via a Kalman filter. Tracked kinetochores are paired by solving another linear assignment problem. Sister kinetochore pairing used spatial and temporal trajectory data. Sister kinetochores are closer (d_{ij}, average distance) and exhibit less distance variation (v_{ij}, distance variance) than non sisters. In the presence of a metaphase plate, their connecting vector aligns with the plate's normal (α_{ij}, average angle). Pairing costs were calculated as $d_{ij} \times v_{ij}$ without a plate or $d_{ij} \times v_{ij} \times \alpha_{ij}$ with a plate. Trajectories had to overlap for at least 10 frames, and the configuration with the minimum global cost was selected.

The code to perform kinetochore tracking is available from `https://github.com/cmcb-warwick/KiT`, and this software includes a graphical user interface (GUI) for ease of use.

Filtering Criteria

To assess metaphase characteristics, Figure 2, 36 RPE1 cells were imaged during metaphase-anaphase of varying durations. A filter was applied to ensure good sister pair coverage per cell. Specifically, at least 30 sister pairs had to be tracked for 75% of the movie length, resulting in 31 cells meeting the criteria and 1281 sister pair kinetochores being tracked. On average, 40 sister pairs per cell were tracked (quartiles: Q1 = 38.5, Q3 = 43), with both sisters tracked for at least 200 seconds (100 frames).

Statistical Tests

The statistical tests used in this study can be found in Appendix C, Table C8.

References

M. I. Anjur-Dietrich, C. P. Kelleher, and D. J. Needleman. Mechanical mechanisms of chromosome segregation. *Cells*, 10(2):465, 2021.

J. W. Armond, E. F. Harry, A. D. McAinsh, and N. J. Burroughs. Inferring the forces controlling metaphase kinetochore oscillations by reverse engineering system dynamics. *PLoS Computational Biology*, 11(11):e1004607, 2015a.

J. W. Armond, E. Vladimirou, M. Erent, A. D. McAinsh, and N. J. Burroughs. Probing microtubule polymerisation state at single kinetochores during metaphase chromosome motion. *Journal of Cell Science*, 128(10):1991–2001, 2015b.

J. W. Armond, K. L. Dale, N. J. Burroughs, A. D. McAinsh, and E. Vladimirou. The dynamics of centromere motion through the metaphase-to-anaphase transition reveal a centromere separation order. *BioRxiv*, page 582379, 2019.

M. Betancourt and M. Girolami. Hamiltonian monte carlo for hierarchical models. *Current trends in Bayesian methodology with applications*, 79(30):2–4, 2015.

R. Blackwell, O. Sweezy-Schindler, C. Edelmaier, Z. R. Gergely, P. J. Flynn, S. Montes, A. Crapo, A. Doostan, J. R. McIntosh, M. A. Glaser, and M. D. Betterton. Contributions of microtubule dynamic instability and rotational diffusion to kinetochore capture. *Biophysical Journal*, 112(3):552–563, 2017.

D. G. Booth, A. J. Beckett, O. Molina, I. Samejima, H. Masumoto, N. Kouprina, V. Larionov, I. A. Prior, and W. C. Earnshaw. 3d-clem reveals that a major portion of mitotic chromosomes is not chromatin. *Molecular Cell*, 64(4): 790–802, 2016. ISSN 1097-2765. doi: 10.1016/j.molcel.2016.10.009.

A. P. Browning, D. J. Warne, K. Burrage, R. E. Baker, and M. J. Simpson. Identifiability analysis for stochastic differential equation models in systems biology. *Journal of the Royal Society Interface*, 17(173):20200652, 2020.

N. J. Burroughs, E. F. Harry, and A. D. McAinsh. Super-resolution kinetochore tracking reveals the mechanisms of human sister kinetochore directional switching. *Elife*, 4:e09500, 2015.

B. Carpenter, A. Gelman, M. D. Hoffman, D. Lee, B. Goodrich, M. Betancourt, M. A. Brubaker, J. Guo, P. Li, and A. Riddell. Stan: a probabilistic programming language. *Journal of Statistical Software*, 76(1):1–32, 2017. ISSN 1548-7660.

B.-C. Chen, W. R. Legant, K. Wang, L. Shao, D. E. Milkie, M. W. Davidson, C. Janetopoulos, X. S. Wu, J. A. Hammer, Z. Liu, et al. Lattice light-sheet microscopy: imaging molecules to embryos at high spatiotemporal resolution. *Science*, 346(6208), 2014. doi: 10.1126/science.1257998.

D. Cimini, B. Howell, P. Maddox, A. Khodjakov, F. Degrassi, and E. Salmon. Merotelic kinetochore orientation is a major mechanism of aneuploidy in mitotic mammalian tissue cells. *Journal of Cell Biology*, 153(3):517–528, 2001.

G. Civelekoglu-Scholey and D. Cimini. Modelling chromosome dynamics in mitosis: A historical perspective on models of metaphase and anaphase in eukaryotic cells. *Interface Focus*, 4(3), 2014. ISSN 20428901.

G. Civelekoglu-Scholey, B. He, M. Shen, X. Wan, E. Roscioli, B. Bowden, and D. Cimini. Dynamic bonds and polar ejection force distribution explain kinetochore oscillations in PtK1 cells. *Journal of Cell Biology*, 201(4):577–593, 2013.

A. Daniyan, A. V. Inchingolo, A. McAinsh, and N. Burroughs. Enhanced kinetochore detection during mitotic human cell division using CFAR. In *2024 27th International Conference on Information Fusion (FUSION)*, pages 1–7, 2024. doi: 10.23919/FUSION59988.2024.10706334.

A. E. Dick and D. W. Gerlich. Kinetic framework of spindle assembly checkpoint signalling. *Nature Cell Biology*, 15 (11):1370–1377, 2013. ISSN 1476-4679. doi: 10.1038/ncb2842.

D. Drpic, A. C. Almeida, P. Aguiar, F. Renda, J. Damas, H. A. Lewin, D. M. Larkin, A. Khodjakov, and H. Maiato. Chromosome segregation is biased by kinetochore size. *Current Biology*, 28(9):1344–1356, 2018.

M. Dumont, R. Gamba, P. Gestraud, S. Klaasen, J. T. Worrall, S. G. De Vries, V. Boudreau, C. Salinas-Luypaert, P. S. Maddox, S. M. Lens, et al. Human chromosome-specific aneuploidy is influenced by dna-dependent centromeric features. *The EMBO journal*, 39(2):e102924, 2020.

M. W. Elting, M. Prakash, D. B. Udy, and S. Dumont. Mapping load-bearing in the mammalian spindle reveals local kinetochore fiber anchorage that provides mechanical isolation and redundancy. *Current Biology*, 27(14):2112–2122, 2017.

P. A. Embacher, T. E. Germanova, E. Roscioli, A. D. McAinsh, and N. J. Burroughs. Bayesian inference of multi-point macromolecular architecture mixtures at nanometre resolution. *PLOS Computational Biology*, 18(12):1–34, 12 2022. doi: 10.1371/journal.pcbi.1010765.

A. Gelman and D. B. Rubin. Inference from iterative simulation using multiple sequences. *Statistical Science*, 7(4): 457–472, 1992.

F. S. Gnesotto, F. Mura, J. Gladrow, and C. P. Broedersz. Broken detailed balance and non-equilibrium dynamics in living systems: a review. *Reports on Progress in Physics*, 81(6):066601, apr 2018. doi: 10.1088/1361-6633/aab3ed.

Q. F. Gronau, H. Singmann, and E.-J. Wagenmakers. bridgesampling: An r package for estimating normalizing constants. *Journal of Statistical Software*, 92(10):1–29, 2020. doi: 10.18637/jss.v092.i10.

L. A. Harasymiw, D. Tank, M. McClellan, N. Panigrahy, and M. K. Gardner. Centromere mechanical maturation during mammalian cell mitosis. *Nature communications*, 10(1):1–21, 2019.

J. U. Harrison, O. Sen, A. D. McAinsh, and N. J. Burroughs. Kinetochore tracking in 3d from lattice light sheet imaging data with kit. *Bioinformatics*, 2022.

T. L. Hill. Theoretical problems related to the attachment of microtubules to kinetochores. *Cell Biology*, 82:4404–4408, 1985. ISSN 0027-8424.

K. E. Hines, T. R. Middendorf, and R. W. Aldrich. Determination of parameter identifiability in nonlinear biophysical models: A Bayesian approach. *The Journal of General Physiology*, 143(3):401–416, 2014.

L. J. Holt, A. N. Krutchinsky, and D. O. Morgan. Positive feedback sharpens the anaphase switch. *Nature*, 454(7202): 353–357, 2008.

K. Iemura, T. Natsume, K. Maehara, M. T. Kanemaki, and K. Tanaka. Chromosome oscillation promotes Aurora A–dependent Hec1 phosphorylation and mitotic fidelity. *Journal of Cell Biology*, 220(7):e202006116, 2021.

M. Jagrić, P. Risteski, J. Martinčić, A. Milas, and I. M. Tolić. Optogenetic control of prc1 reveals its role in chromosome alignment on the spindle by overlap length-dependent forces. *eLife*, 10:e61170, jan 2021. ISSN 2050-084X. doi: 10.7554/eLife.61170.

K. Jaqaman, E. M. King, A. C. Amaro, J. R. Winter, J. F. Dorn, H. L. Elliott, N. Mchedlishvili, S. E. McClelland, I. M. Porter, M. Posch, A. Toso, G. Danuser, A. D. McAinsh, P. Meraldi, and J. R. Swedlow. Kinetochore alignment within the metaphase plate is regulated by centromere stiffness and microtubule depolymerases. *Journal of Cell Biology*, 188(5):665–679, 2010a. ISSN 00219525. doi: 10.1083/jcb.200909005.

K. Jaqaman, E. M. King, A. C. Amaro, J. R. Winter, J. F. Dorn, H. L. Elliott, N. Mchedlishvili, S. E. McClelland, I. M. Porter, M. Posch, et al. Kinetochore alignment within the metaphase plate is regulated by centromere stiffness and microtubule depolymerases. *Journal of Cell Biology*, 188(5):665–679, 2010b.

A. P. Joglekar and A. J. Hunt. A simple, mechanistic model for directional instability during mitotic chromosome movements. *Biophysical Journal*, 83(1):42–58, 2002. ISSN 00063495.

J. Kajtez, A. Solomatina, M. Novak, B. Polak, K. Vukušić, J. Rüdiger, G. Cojoc, A. Milas, I. Š. Šestak, P. Risteski, et al. Overlap microtubules link sister k-fibres and balance the forces on bi-oriented kinetochores. *Nature Communications*, 7(1):1–11, 2016.

R. E. Kass and A. E. Raftery. Bayes factors. *Journal of the American Statistical Association*, 90(430):773–795, 1995. doi: 10.1080/01621459.1995.10476572.

K. Ke, J. Cheng, and A. J. Hunt. The distribution of polar ejection forces determines the amplitude of chromosome directional instability. *Current Biology*, 19(10):807–815, 2009.

I. Matos, A. J. Pereira, M. Lince-Faria, L. A. Cameron, E. D. Salmon, and H. Maiato. Synchronizing chromosome segregation by flux-dependent force equalization at kinetochores. *Journal of Cell Biology*, 186(1):11–26, 2009.

X.-L. Meng and W. H. Wong. Simulating ratios of normalizing constants via a simple identity: A theoretical exploration. *Statistica Sinica*, 6(4):831–860, 1996.

C. E. Miles, J. Zhu, and A. Mogilner. Mechanical torque promotes bipolarity of the mitotic spindle through multi-centrosomal clustering. *Bulletin of Mathematical Biology*, 84(2):29, 2022. doi: 10.1007/s11538-021-00985-2.

A. Mogilner, R. Wollman, G. Civelekoglu-Scholey, and J. Scholey. Modeling mitosis. *Trends in Cell Biology*, 16(2): 88–96, 2006.

W. Mosgöller, A. Leitch, J. Brown, and J. Heslop-Harrison. Chromosome arrangements in human fibroblasts at mitosis. *Human Genetics*, 88(1):27 – 33, 1991. doi: 10.1007/BF00204924.

A. P. Navarro and I. M. Cheeseman. Kinetochore assembly throughout the cell cycle. *Seminars in Cell & Developmental Biology*, 117:62–74, 2021. ISSN 1084-9521. doi: 10.1016/j.semcdb.2021.03.008.

R. Neal. Mcmc using hamiltonian dynamics. In S. Brooks, A. Gelman, G. L. Jones, and X.-L. Meng, editors, *Handbook of Markov Chain Monte Carlo*, pages 116–162. Chapman and Hall/CRC, 2011.

M. Novak, B. Polak, J. Simunić, Z. Boban, B. Kuzmić, A. W. Thomae, I. M. Tolić, and N. Pavin. The mitotic spindle is chiral due to torques within microtubule bundles. *Nature Communications*, 9(1):1–10, 2018.

M. Pargett and D. M. Umulis. Quantitative model analysis with diverse biological data : Applications in developmental pattern formation Labeled structures. *Methods*, 62(1):56–67, 2013. ISSN 1046-2023.

N. Pavin and I. M. Tolić. Mechanobiology of the mitotic spindle. *Developmental Cell*, 2020.

F. Rago and I. M. Cheeseman. The functions and consequences of force at kinetochores. *Journal of Cell Biology*, 200 (5):557–565, 2013.

E. Roscioli, T. E. Germanova, C. A. Smith, P. A. Embacher, M. Erent, A. I. Thompson, N. J. Burroughs, and A. D. McAinsh. Ensemble-level organization of human kinetochores and evidence for distinct tension and attachment sensors. *Cell Reports*, 31(4):107535, 2020.

S. L. Scott. Bayesian methods for hidden markov models. *Journal of the American Statistical Association*, 97(457): 337–351, 2002. doi: 10.1198/016214502753479464.

O. Sen, J. U. Harrison, N. J. Burroughs, and A. D. McAinsh. Kinetochore life histories reveal an Aurora-B-dependent error correction mechanism in anaphase. *Developmental Cell*, 2021.

Y. Shimamoto, Y. T. Maeda, S. Ishiwata, A. J. Libchaber, and T. M. Kapoor. Insights into the micromechanical properties of the metaphase spindle. *Cell*, 145(7):1062–1074, 2011.

R. V. Skibbens, V. P. Skeen, and E. D. Salmon. Directional Instability of Kinetochore Motility during Chromosome Congression and Segregation in Mitotic Newt Lung Cells : A Push-Pull Mechanism. *Journal of Cell Biology*, 122(4), 1993.

C. A. Smith, A. D. McAinsh, and N. J. Burroughs. Human kinetochores are swivel joints that mediate microtubule attachments. *Elife*, 5:e16159, 2016.

Stan Development Team. RStan: the R interface to Stan, 2024a. URL `https://mc-stan.org/`. R package version 2.32.6.

Stan Development Team. Stan Modeling Language Users Guide and Reference Manual, version 2.26.24, 2024b. URL `https://mc-stan.org`.

A. D. Stephens, R. A. Haggerty, P. A. Vasquez, L. Vicci, C. E. Snider, F. Shi, C. Quammen, C. Mullins, J. Haase, I. Taylor, Russell M., J. S. Verdaasdonk, M. R. Falvo, Y. Jin, M. G. Forest, and K. Bloom. Pericentric chromatin loops function as a nonlinear spring in mitotic force balance. *Journal of Cell Biology*, 200(6):757–772, 03 2013. ISSN 0021-9525. doi: 10.1083/jcb.201208163.

K.-C. Su, Z. Barry, N. Schweizer, H. Maiato, M. Bathe, and I. M. Cheeseman. A regulatory switch alters chromosome motions at the metaphase-to-anaphase transition. *Cell Reports*, 17(7):1728–1738, 2016.

A. Vehtari, A. Gelman, D. Simpson, B. Carpenter, and P.-C. Bürkner. Rank-normalization, folding, and localization: An improved $\hat{R}$ for assessing convergence of MCMC. *Bayesian Analysis*, 1(1):1–28, 2021.

E. Vladimirou, N. Mchedlishvili, I. Gasic, J. W. Armond, C. P. Samora, P. Meraldi, and A. D. McAinsh. Nonautonomous movement of chromosomes in mitosis. *Developmental Cell*, 27(1):60–71, 2013.

K. Vukušić, R. Buđa, A. Bosilj, A. Milas, N. Pavin, and I. M. Tolic. Microtubule Sliding within the Bridging Fiber Pushes Kinetochore Fibers Apart to Segregate Chromosomes. *Developmental Cell*, 43(1):11–23.e6, Oct. 2017.

X. Wan, D. Cimini, L. A. Cameron, and E. Salmon. The coupling between sister kinetochore directional instability and oscillations in centromere stretch in metaphase PtK1 cells. *Molecular Biology of the Cell*, 23(6):1035–1046, 2012.

J. T. Worrall, N. Tamura, A. Mazzagatti, N. Shaikh, T. van Lingen, B. Bakker, D. C. J. Spierings, E. Vladimirou, F. Foijer, and S. E. McClelland. Non-random mis-segregation of human chromosomes. *Cell Reports*, 23(11): 3366–3380, 2018.

A. V. Zaytsev and E. L. Grishchuk. Basic mechanism for biorientation of mitotic chromosomes is provided by the kinetochore geometry and indiscriminate turnover of kinetochore microtubules. *Molecular biology of the cell*, 26 (22):3985–3998, 2015.

Appendix

A Additional tables

Parameter	Within variance	Between-cell variance	Between-location variance	Between cell/location variance	sd/mean
α	4.0×10^{-5}	$2.3 \times 10^{-6*}$	4.6×10^{-8}	50.256	0.508
κ	2.1×10^{-4}	$3.6 \times 10^{-5*}$	$2.9 \times 10^{-5*}$	1.256	0.578
L	9.0×10^{-4}	$1.1 \times 10^{-4*}$	$9.9 \times 10^{-6*}$	11.416	0.037
τ	3.2×10^{4}	$1.9 \times 10^{4*}$	$3.1 \times 10^{3*}$	5.987	0.260
v_-	1.8×10^{-4}	$2.3 \times 10^{-5*}$	$4.1 \times 10^{-5*}$	0.569	0.303
v_+	3.4×10^{-5}	$9.7 \times 10^{-6*}$	$9.0 \times 10^{-7*}$	10.723	0.562
p_{icoh}	1.2×10^{-2}	$1.7 \times 10^{-3*}$	$3.0 \times 10^{-3*}$	0.582	0.149
p_{coh}	2.3×10^{-4}	$3.5 \times 10^{-5*}$	$2.4 \times 10^{-5*}$	1.451	0.279

Table A1: K-fiber force variation within cells is larger than between cells. Variance contributions of the biophysical parameters, ($n = 635$ KT pairs from $N = 24$ cells to allow for at least 3 sister pairs in each group and remove outliers), grouping by cell and location (3 radius group classes) within the metaphase plate. The second column denotes the within-cell variance (*i.e.,* , residuals), while the third and fourth columns report the within cell and location variance respectively. Parameter estimations use the model with asymmetry on v_- and v_+; the posterior median v_- and v_+ values are averaged over the two sisters. Stars denote that there is statistically significant difference ($\alpha < 0.01$) between groups of this factor. The ratio of the between cell to the between location variance is shown in fifth column and the size of effect (ratio of population parameters' standard deviation to the population parameters' (abs) mean) in last column. Stars denote the statistically different ratio at $\alpha < 0.01$. Caution: Due to low coverage of KT pairs per cell within each radius group, these results should be taken with caution as some of the ANOVA assumptions are violated.

Parameter	Within variance	Between-cell variance	Between-location variance	Between cell/location variance	sd/mean
α	3.6×10^{-5}	$3.3 \times 10^{-6*}$	5.0×10^{-7}	6.57	0.393
κ	1.8×10^{-4}	$4.4 \times 10^{-5*}$	$4.2 \times 10^{-5*}$	1.045	0.660
L	8.9×10^{-4}	8.9×10^{-5}	$2.1 \times 10^{-5*}$	4.233	0.037
τ	2.0×10^{4}	$7.2 \times 10^{3*}$	$2.6 \times 10^{2*}$	2.748	0.171
v_-	1.9×10^{-4}	$4.9 \times 10^{-5*}$	$5.4 \times 10^{-5*}$	0.897	0.321
v_+	2.8×10^{-5}	$8.8 \times 10^{-6*}$	$1.7 \times 10^{-6*}$	5.124	0.589
p_{icoh}	1.3×10^{-2}	$1.7 \times 10^{-3*}$	$4.4 \times 10^{-3*}$	0.379	0.149
p_{coh}	1.7×10^{-4}	$3.7 \times 10^{-5*}$	$1.8 \times 10^{-5*}$	2.108	0.014

Table A2: Variance contributions of the biophysical parameters, ($n = 290$ KT pairs from $N = 11$ cells to allow for at least 3 sister pairs in each group), grouping by cell and location (3 radius group classes) within the metaphase plate in nocodazole washout treated cells. The second column denotes the within-cell variance (i.e., residuals), while the third and fourth columns report the within cell and location variance respectively. Parameter estimations use the model with asymmetry on v_- and v_+; the posterior median v_- and v_+ values are averaged over the two sisters. Stars denote that there is statistically significant difference ($\alpha < 0.01$) between groups of this factor. The ratio of the between cell to the between location variance is shown in fifth column and the size of effect (ratio of population parameters' standard deviation to the population parameters' (abs) mean) in last column. Stars denote the statistically different ratio at $\alpha < 0.01$. Caution: Due to low coverage of KT pairs per cell within each radius group, these results should be taken with caution as some of the ANOVA assumptions are violated.

	Symmetric		Asymmetric	
	Median	PIR	Median	PIR
τ	830.6 [265.34]	86.42	824.1 [229.1]	83.77
κ	0.017 [0.017]	0.013	0.019 [0.024]	0.013
α	0.012 [0.009]	0.005	0.016 [0.009]	0.005
v_-^1	-0.039 [0.020]	0.006	-0.053 [0.018]	0.009
v_-^2	-0.039 [0.020]	0.005	-0.030[0.021]	0.009
v_+^1	0.006 [0.007]	0.005	0.002 [0.002]	0.007
v_+^2	0.006 [0.07]	0.005	0.016 [0.009]	0.007
L	0.813 [0.042]	0.176	0.840 [0.077]	0.156
p_{icoh}	0.777 [0.220]	0.120	0.803 [0.226]	0.133
p_{coh}	0.947 [0.0208]	0.021	0.952 [0.019]	0.020

Table A3: Summary statistics of symmetric and asymmetric sisters of nocodazole washout treated cells. We label sister 1 as the sister with the greater pulling force ,*i.e.,* $\left|v_-^1\right| \geq \left|v_-^2\right|$. The first and third columns reports the medians of posterior medians for symmetric and asymmetric sisters respectively, while brackets report the population interquartile range. The second and fourth columns report the median of Posterior Interquartile Ranges (PIR) for symmetric and asymmetric sisters, respectively. Based on Mann-Whitney and Kolmogorov-Smirnov tests, the all asymmetric posterior distributions but τ are significantly different that the symmetric posterior distributions, with size of effect (*i.e.,* , percentage difference of the medians) being 15.7%, 26.4% and 9.5%, 20.6%, 2.6% for $\kappa, \alpha, v_-, v_+, L$ respectively . Note that asymmetric parameter values on v_- and v_+ are averaged over the two sisters.

Preferred Model	Pearson	Kendal	Spearman
α	4.8×10^{-1}	1.2×10^{-1}	1.2×10^{-1}
κ	2.2×10^{-16}	2.2×10^{-16}	2.2×10^{-16}
L	9.8×10^{-1}	1.2×10^{-3}	1.2×10^{-3}
v_-	2.2×10^{-16}	2.2×10^{-16}	2.2×10^{-16}
v_+	7.8×10^{-7}	2.7×10^{-7}	2.5×10^{-7}
τ	1.9×10^{-15}	6.5×10^{-15}	9.4×10^{-15}

Table A4: Spatial biophysical parameter trends across the metaphase plate: p-values of Pearson's , Kendall's and Spearman's tests for the presence of a trend, in 798 kinetochore pairs over 26 DMSO treated cells.

Preferred Model	Population	Cell
α	4.8×10^{-1}	6.5×10^{-1}
κ	2.2×10^{-16}	4.5×10^{-5}
L	9.8×10^{-1}	1.9×10^{-1}
v_-	2.2×10^{-16}	2.2×10^{-5}
v_+	7.8×10^{-7}	7.5×10^{-1}
τ	1.9×10^{-5}	2.3×10^{-15}

Table A5: Spatial biophysical parameter trends across the metaphase plate: p-values of Pearson's test for the presence of a trend, in 798 kinetochore pairs over 26 DMSO treated cells, versus the p-values of 36 kinetochore pairs coming from one DMSO treated cell.

B Additional plots

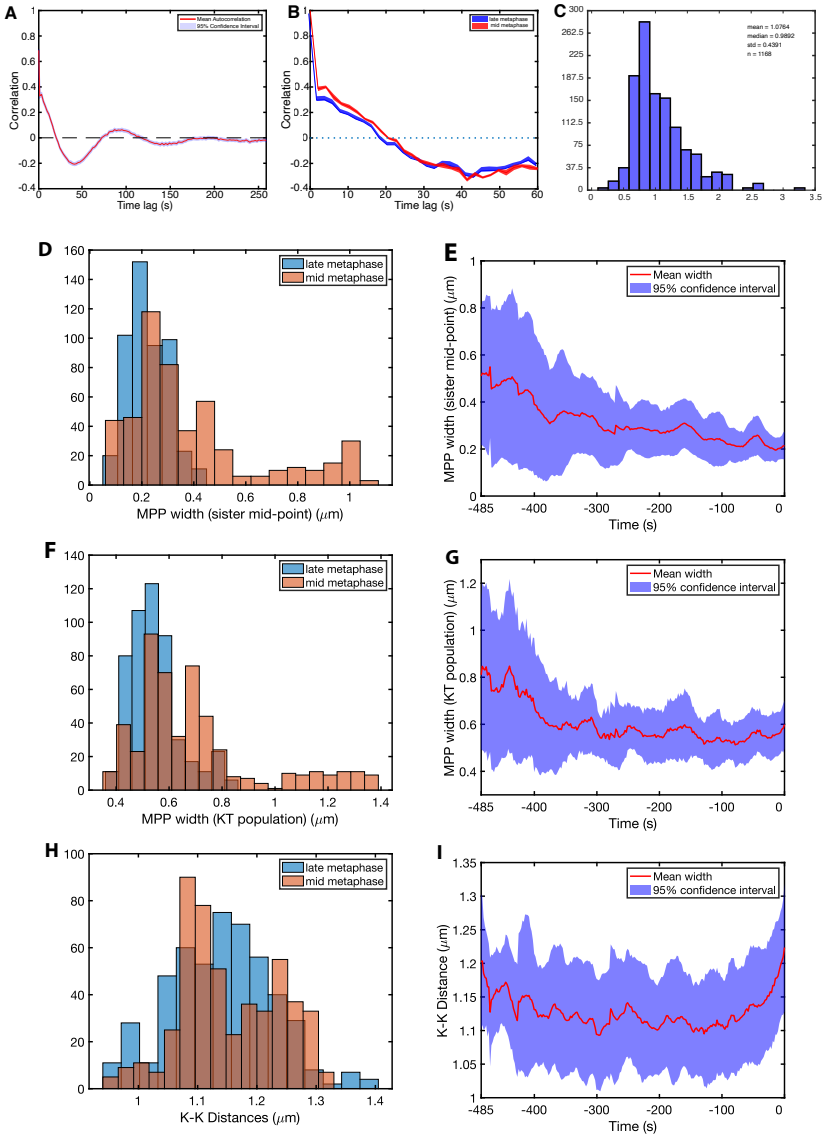

Figure B1: Quantification of intrametaphase maturation in nocodazole washout treated cells. **A** Autocorrelation plot showing the temporal correlation of metaphase oscillations. **B** Autocorrelation of metaphase oscillations in late (red) and mid (blue) metaphase. **C** Sister kinetochore (KK) distance pooled over all KT pairs and time. **D/E** MPP width as measured by paired sister mid-point width (smallest eigenvalue of the covariance matrix of kinetochore mid-points). MPP statistics: **F/G** Metaphase plate (MPP) width as measured by the covariance matrix of the KT population (smallest eigenvalue). **H/I** KK distance. Comparison of mid (orange) and late (blue) metaphase in **D,F,H**, and time-series (time before anaphase onset) in **E,G,I**, mean (red) and standard deviation (blue). Data are based on cells having at least 30 sisters both tracked for 75% of the movie (31 cells in total). Early and mid-metaphase median estimates of MPP in D and F where significantly different (minimum $p_{MW} < 10^{-30}$, while the KK-distance in early an mid-metaphase remained the same, $p_{MW} = 0.026$.

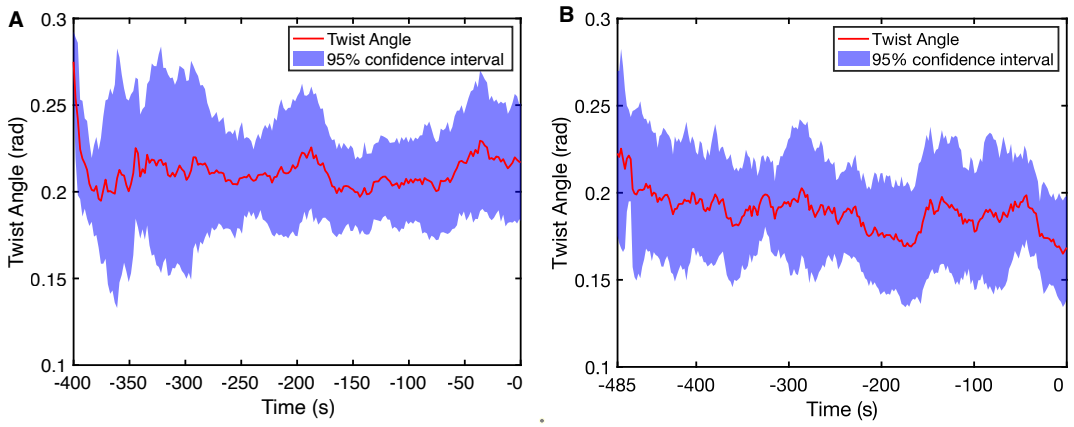

Figure B2: Mean twist angle (in radians) in **A** DMSO **B** nocodazole washout treated data. Shaded blue areas denote the 95% confidence intervals. Time 0 denotes the anaphase onset.

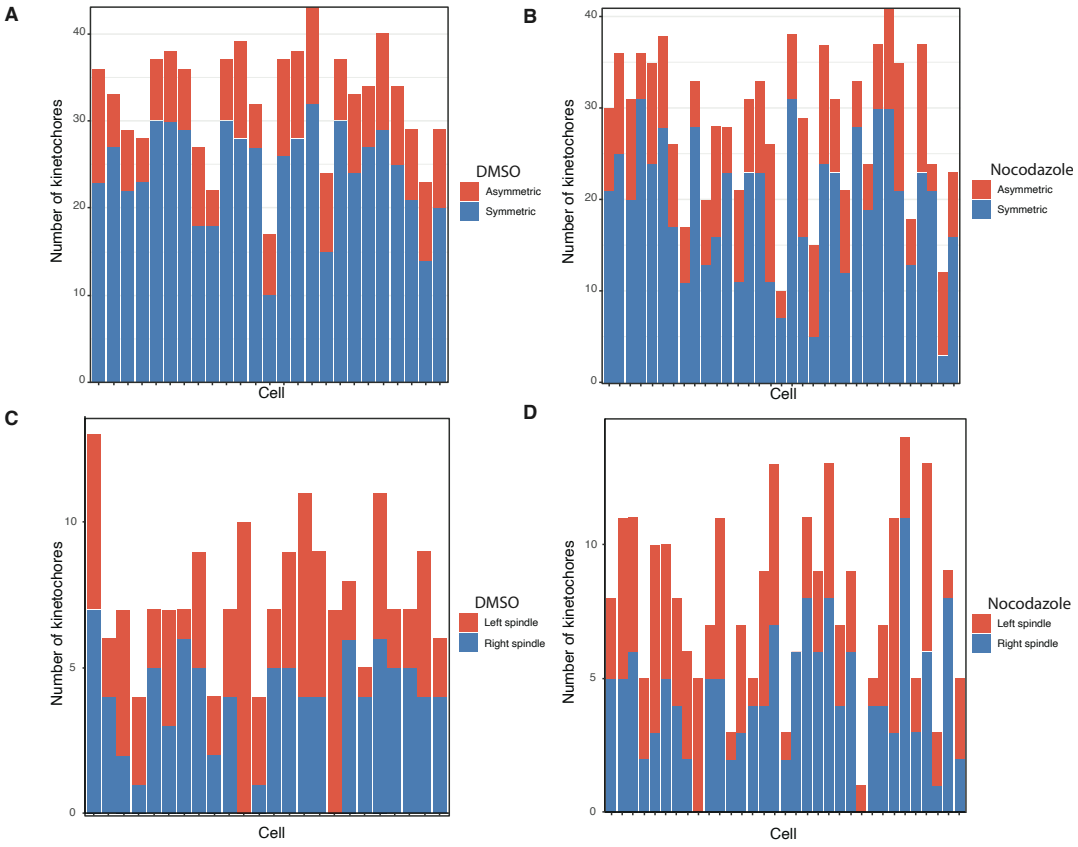

Figure B3: All cells present a significant fraction of asymmetric sisters and no half-spindle bias is observed. **A/B** Symmetric (blue) and significantly asymmetric (red) sister pairs within a cell in **A** DMSO and **B** nocodazole washout treated cells. **C/D** Number of stronger pulling asymmetric sisters positioned in the left (blue) and right (red) half-spindle for **C** DMSO and **D** nocodazole washout treated cells.

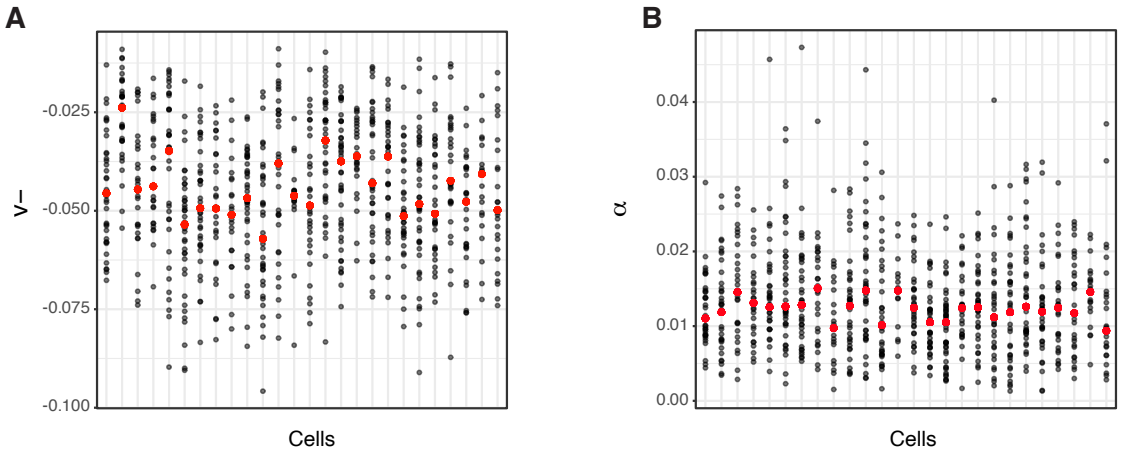

Figure B4: Posterior median estimations of **A** v_{-} and **B** α shown with respect to cell (x-axis). Red dot denotes the median value of the posterior estimations per cell. Between cell variation is evident in both plots.

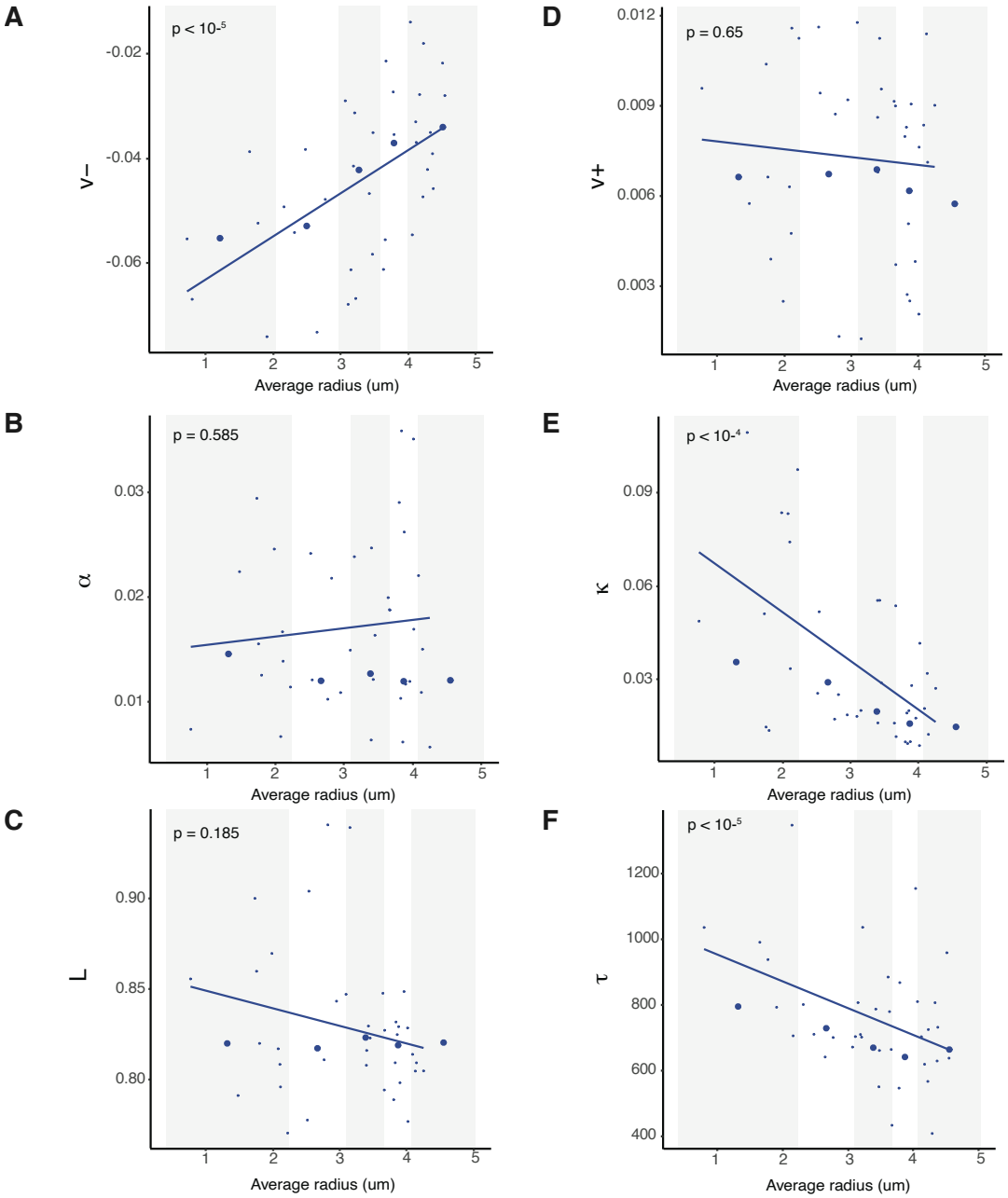

Figure B5: Spatial biophysical parameter trends across the metaphase plate for a single (DMSO) cell. General population trends are evident even on a cell basis. Summary statistics of indicated biophysical parameters partitioned into 5 groups for the average radial position within the metaphase plate. Groups are equally sized, containing the same number of observations, with the five groups defined by their radial distances, *i.e.*, $[0, 2.03]$, $(2.03, 2.95]$, $(2.95, 3.58]$, $(3.580, 4.01]$, $(4.01, 5.03]$ respectively. **B** Pulling forces v_-, **C** Pushing forces v_+, **D** Spring constant κ, **E** PEF, **F** precision τ, **G** Natural length of the centromeric chromatin spring connecting the kinetochore sisters L.

Maturation during metaphase

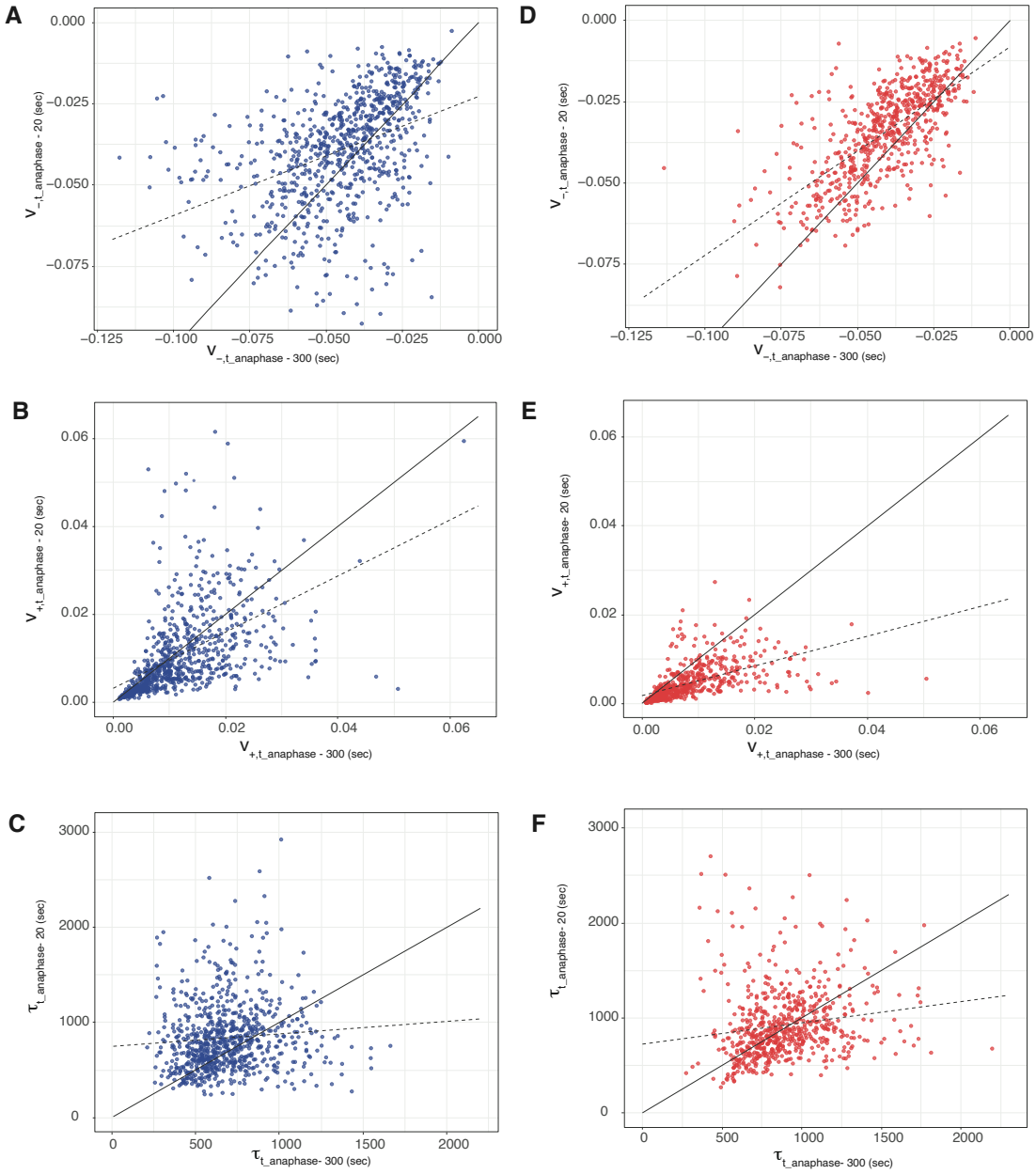

Figure B6: Maturation towards an anaphase ready state. Temporal changes of speed and noise across the last 5 mins of metaphase. Estimated parameters of the model with time dependent parameters v_-, v_+ and τ for **A,B,C** DMSO (blue) **D,E,F** nocodazole washout (red) treated cells, respectively. Estimations are based on the median posterior parameters and calculated at two different time points at 300 seconds and 30 seconds prior to anaphase, *i.e.*, $t = t_{anaphase} - 20$ (y-axis) and $t = t_{anaphase} - 300$ (x-axis). The discrete map comprising the line of regression and the 1:1 diagonal indicate the existence of a stable fixed point at $v_- = -0.04$ ($v_- = -0.02$), $v_+ = 0.01$ ($v_+ = 0.003$) and $\tau = 849$ ($\tau = 923$) in DMSO (nocodazole washout) treated cells.

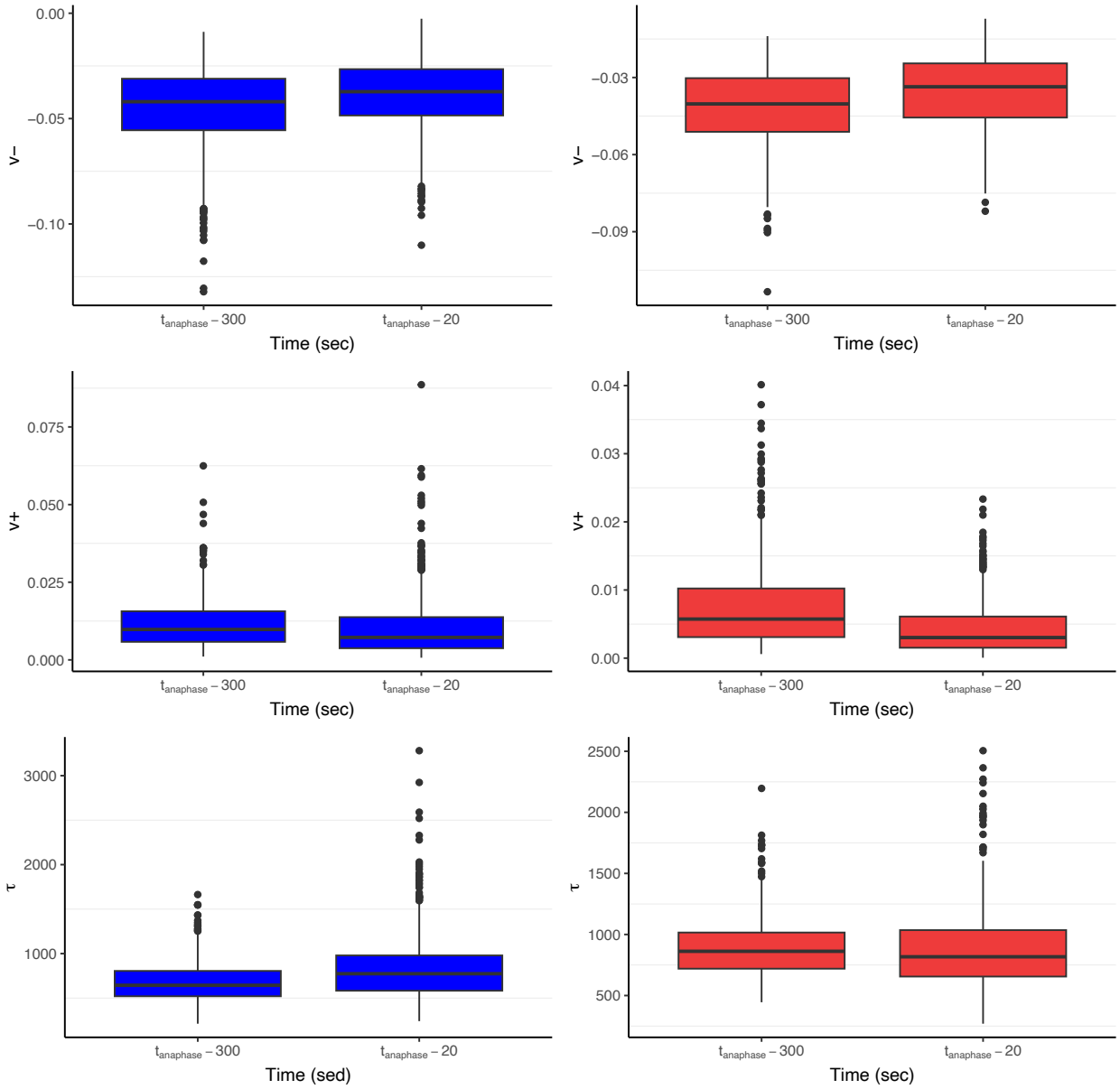

Figure B7: Maturation of dynamic parameters from mid-metaphase (300 s before anaphase) and just before anaphase onset (20s before anaphase). Box plots of the posterior estimation of $v_-(t) = v_{-0} \exp\{v_{-1}t\}, v_+(t) = v_{+0} \exp\{v_{+1}t\}, \tau(t) = \tau_0 \exp\{\tau_1 t\}$, evaluated at time t set to 300 seconds and 20 seconds prior to anaphase, *i.e.*, $t = t_{anaphase} - 300$ and $t = t_{anaphase} - 20$. DMSO (blue) and nocodazole washout (red) treated cells.

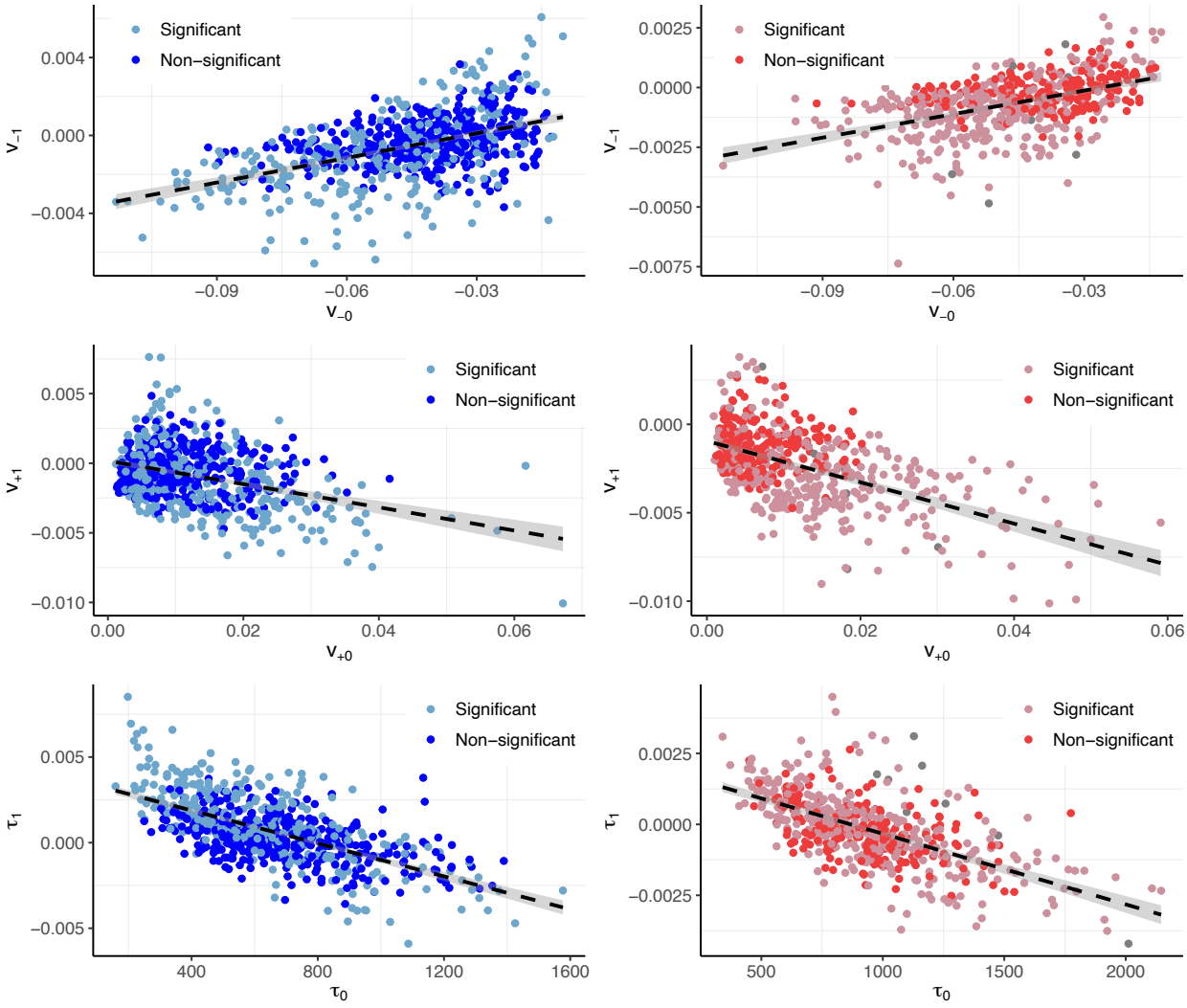

Figure B8: Median posterior parameters of $v_{0-}, v_{1-}, v_{0+}, v_{1+}$ and τ_0, τ_1 for DMSO (blue) and nocodazole washout (red) treated cells of the model with time dependent parameters v_-, v_+ and τ. Estimations of sister pairs which had a preference on the constant/temporal model are denoted with dark/light colours.

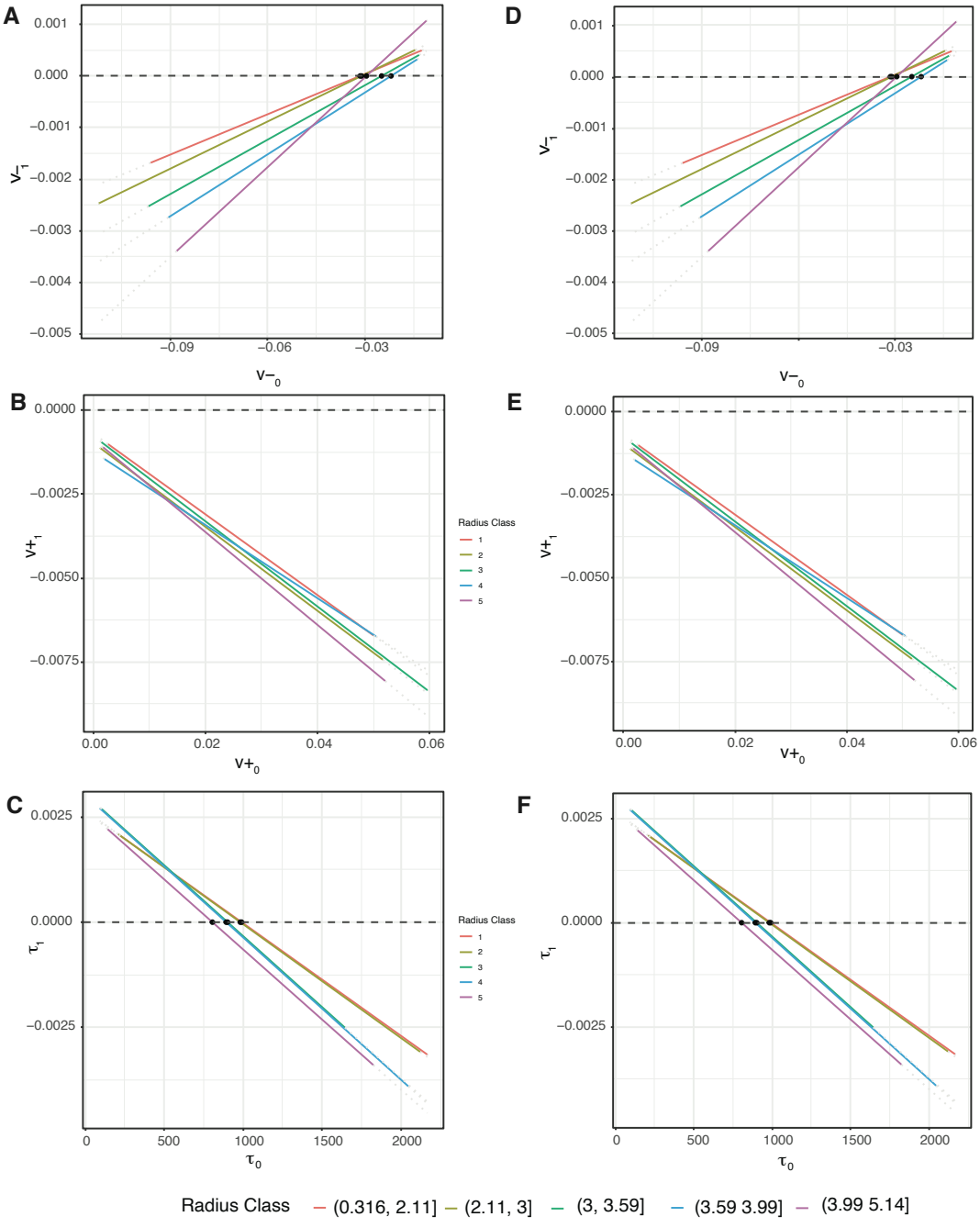

Figure B9: Tuning is consistent across the MPP. Plots of the regression lines for the KT pairs belonging in each of the 5 radius classes (with the five groups defined by their radial distances, *i.e.,* $[0, 2.11]$, $(2.113]$, $(3, 3.59]$, $(3.59, 3.99]$, $(3.99, 5.14]$ respectively) estimates of initial p_0 with time dependent parameter p_1. **A, D** Pulling forces v_- in DMSO, nocodazole washout treated cells, respectively. **B, E** Pushing forces v_+ in DMSO, nocodazole washout treated cells, respectively.**C, F** Noise τ in DMSO, nocodazole washout treated cells, respectively.

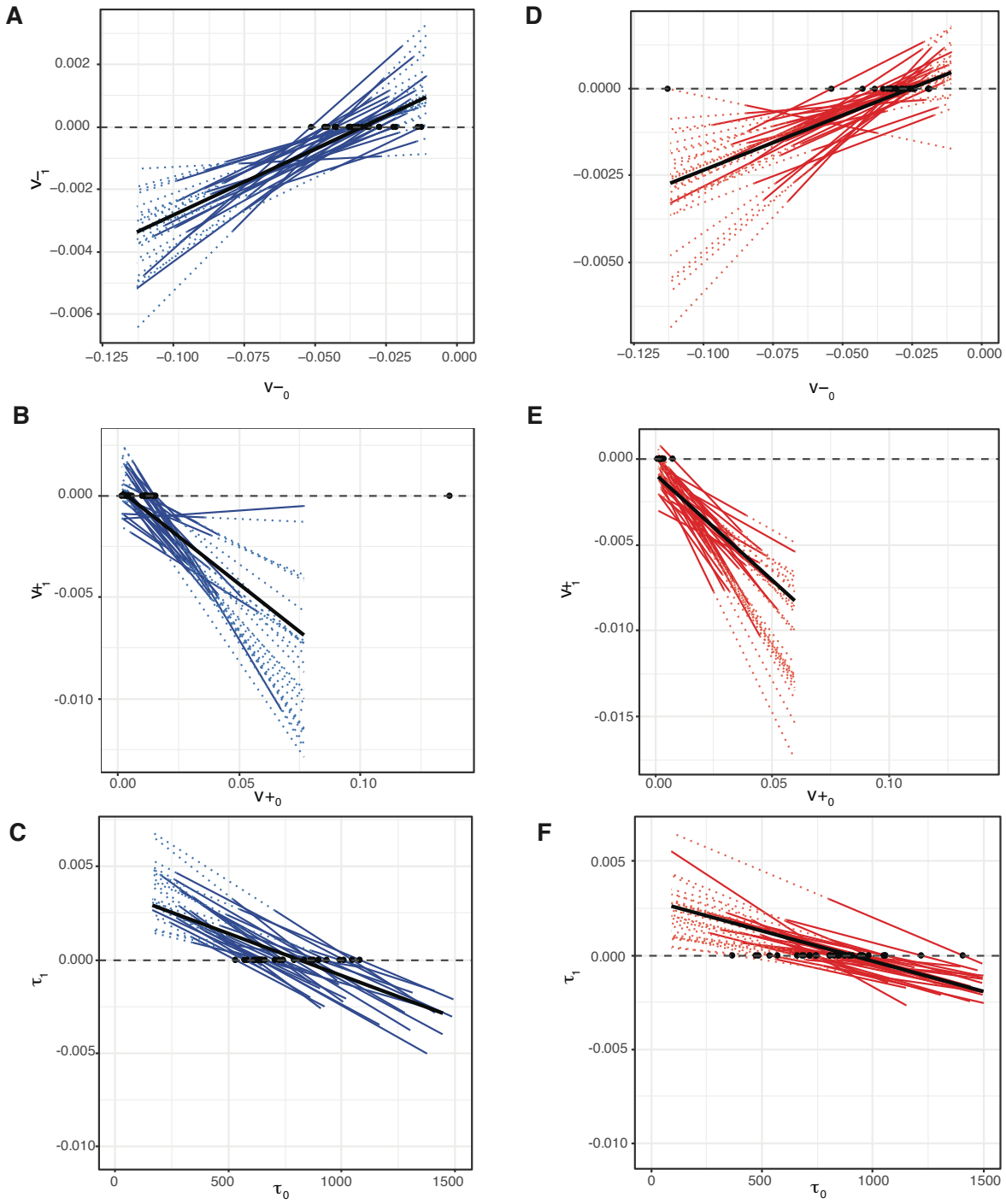

Figure B10: Tuning occurs in individual cells. Plots of the regression lines for individual cells of KT pair estimates of initial p_0 with time dependent parameter p_1. **A/D** Pulling forces v_- in DMSO, nocodazole washout treated cells. 92.3% and 83% of cells have physical (negative) anaphase ready state estimates (intercept of regression line with $v_{-1} = 0$, **B/E** pushing forces v_+ in DMSO, nocodazole washout treated cells, 73.1% and 67.7% of cells have physical (positive) anaphase ready state, **C/F** precision τ, in DMSO, nocodazole washout treated cells, 100%, respectively 100% have positive intercept at $\tau_1 = 0$.

4 **Nocodazole washout treated cells: Asymmetry and maturation during metaphase**

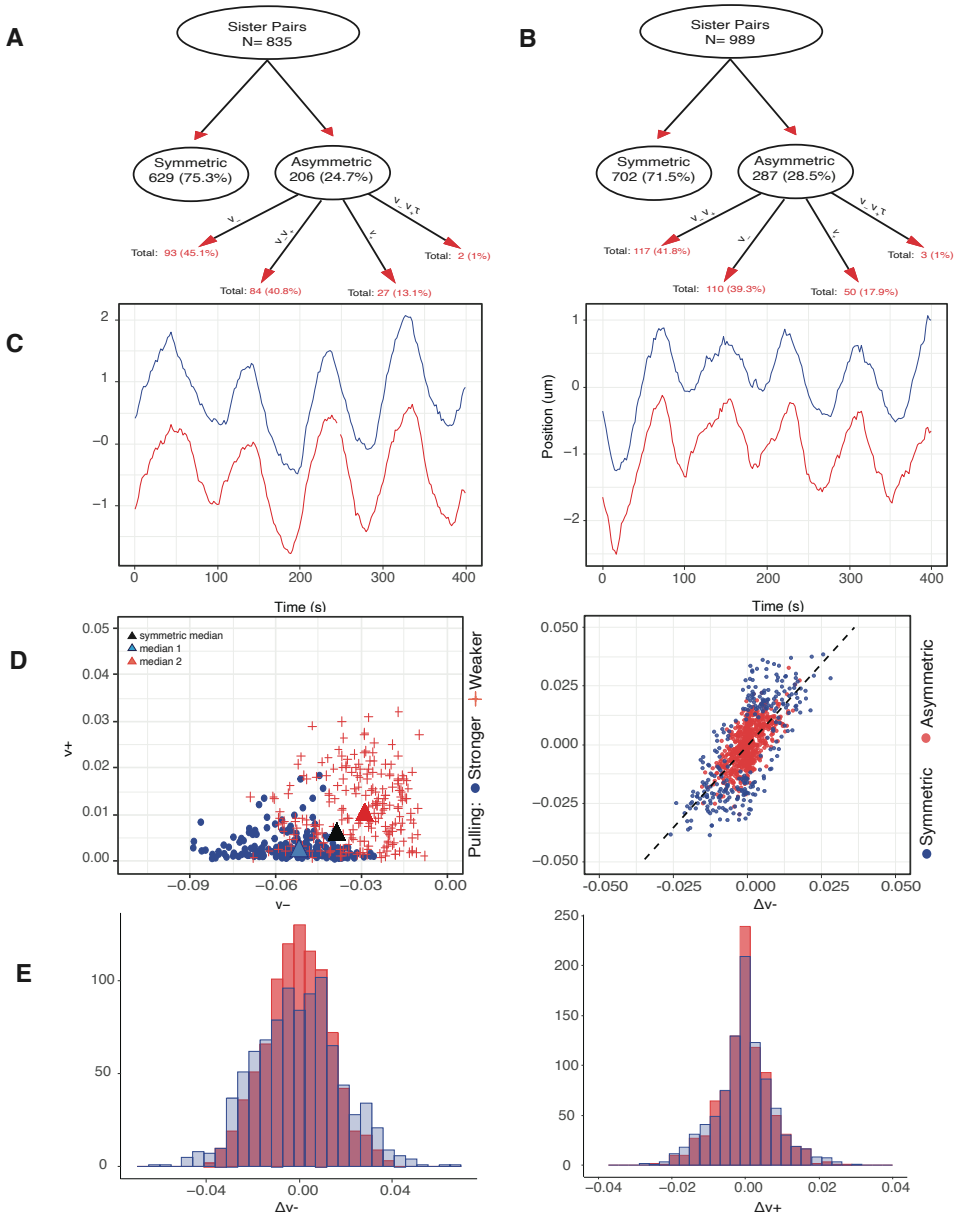

Figure B11: Asymmetry in sister kinetochores is unaffected by nocodazole wash-out treatment. **A/B** Graphical representation of asymmetry model preference network in DMSO (A) and nocodazole washout (B) treated cells. **C** Typical symmetric (left) and asymmetric (right) trajectory. No distinctive characteristics between the symmetric and asymmetric sister pairs, nocodazole washout treated. **D** (LEFT) Comparison of inferred $v-$ and $v+$, using the asymmetric on v_-, v_+ model, over the nocodazole washout asymmetric pairs. Distinction of sisters within a pair is based on their pulling force strength. Stronger and weaker pulling sisters are denoted with blue and red. Population medians are marked with triangle, while black triangle shows the estimated population median of the symmetric pairs.(RIGHT) Direct comparison of $\Delta\left(v_-^1, v_-^2\right)$ versus $\Delta\left(v_+^1, v_+^2\right)$ of symmetric and asymmetric nocodazole washout treated sister pairs, in red and blue respectively, when inferring them with the v_-, v_+ model. Asymmetric pairs do not present any distinctive pattern. **E** Histograms of the nocodazole washout sister difference distribution, *i.e.,* $\Delta\left(v_-^1, v_-^2\right)$ (left) and of $\Delta\left(v_+^1, v_+^2\right)$ (right), when accounting for the sister pairing (red) and disturbing randomizing the pairing (blue), while accounting for the spatial metaphase plate distance.

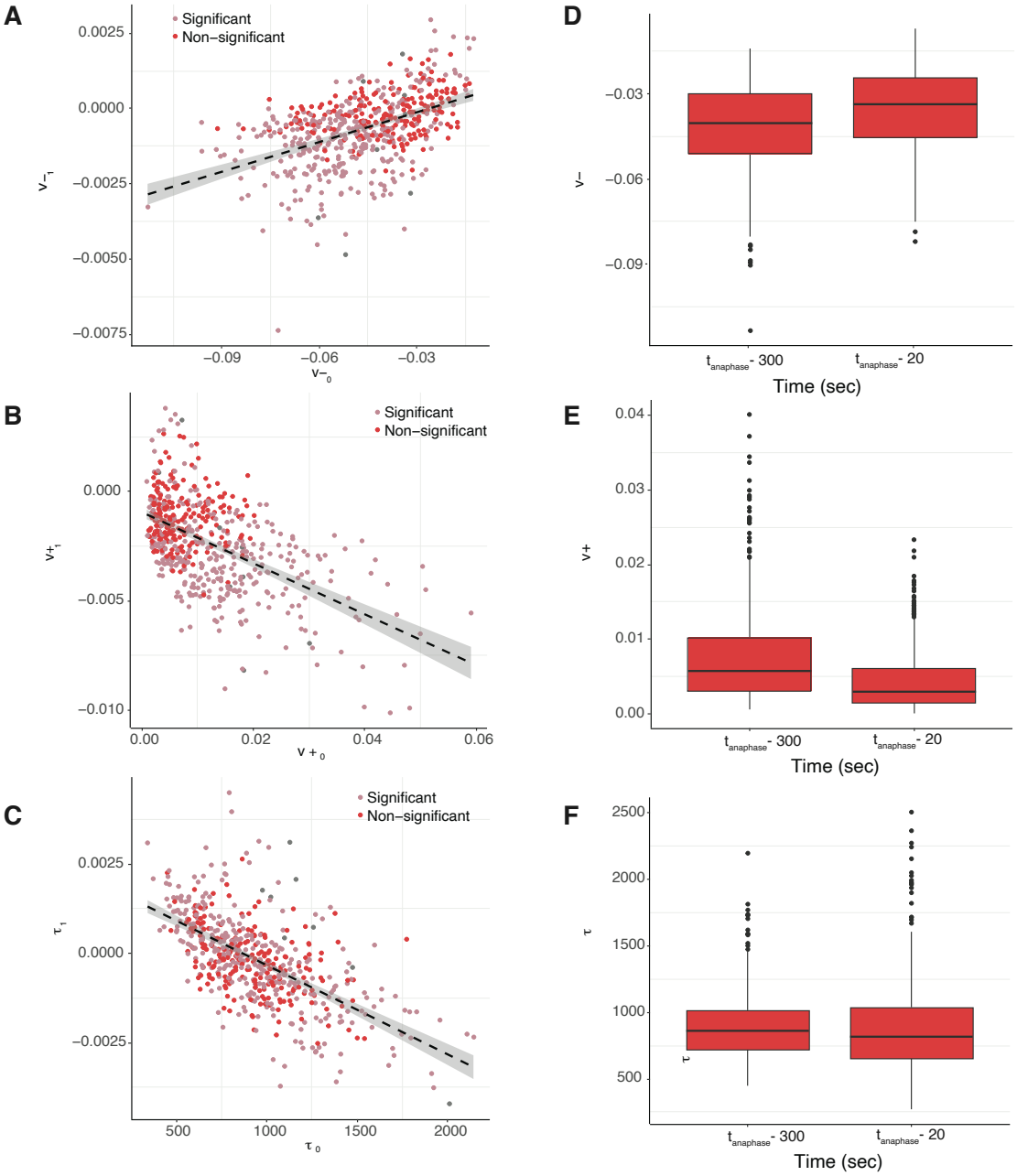

Figure B12: Mechanical tuning in nocodazole washout treated cells. **A/B/C** Scatter plot of posterior median of time dependence p_1 versus initial parameter value p_1 for **A** pushing forces, $v_{1,+}$ versus $v_{0,+}$; **B** pulling forces, $v_{1,-}$ versus $v_{0,-}$; **C** $\tau_{1,+}$ versus $\tau_{0,+}$. **D/E/F** Boxplots of posterior median parameter at the beginning and the end of the trajectory for **D** pushing forces v_+; **E** pulling forces v_-; and **F** noise τ. Parameters v_-, v_+ are statistically different over time (mid-metaphase to late-metaphase comparison), ($p_{MW} < 10^{-16}, p_{MW} < 10^{-9}, p_{MW} < 10^{-16}$ for $v_-, v_+,$ respectively), while τ is not found to be statistically different over time. Finally, variances over time are statistically different with ($p_{BF} < 10^{-17}, p_{BF} < 10^{-35}, p_{BF} < 10^{-3}$ for v_-, v_+, τ respectively). Parameters are inferred on the $M_{v\pm\tau}$ model.

Metaphase oscillation analysis

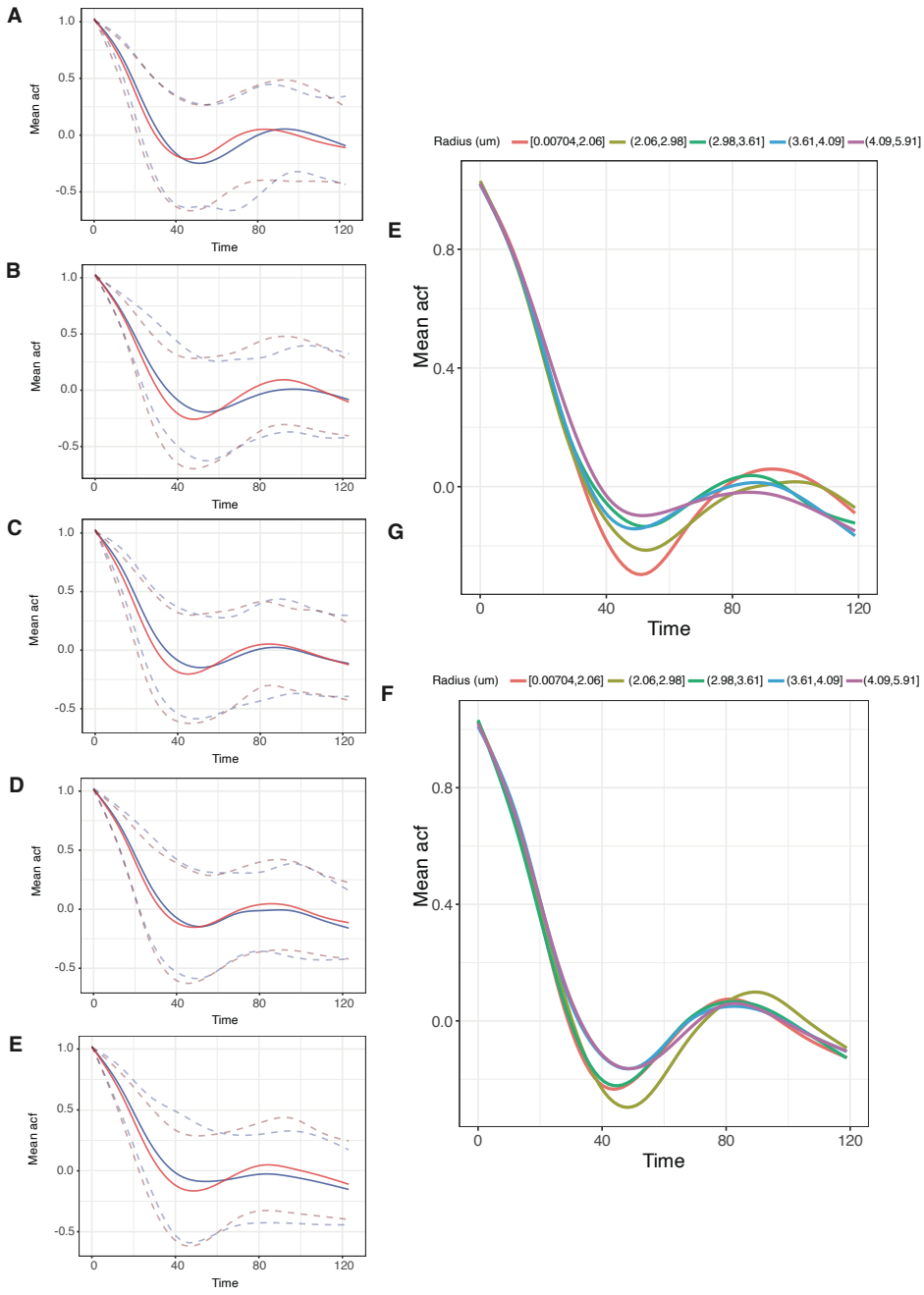

Figure B13: Autocorrelation plot analysis across the metaphase plate: **A-E** Autocorrelation plots for DMSO (blue) and nocodazole washout (red) treated cells. Plots A to E present the mean autocorrelations for sister pairs that belong in one of five groups defined by their radial distances, *i.e.,* $[0, 2.07]$, $(2.07, 2.97]$, $(2.97, 3.59]$, $(3.59, 4.01]$, $(4.01, 5.20]$ respectively. Dashed lines denote the 5% and 95% autocorrelations percentile for each time point. **E, F** Summary of mean autocorrelation plots for DMSO and nocodazole washout treated cells for all 5 classes of radial distances.

6 **Metaphase - Anaphase model**

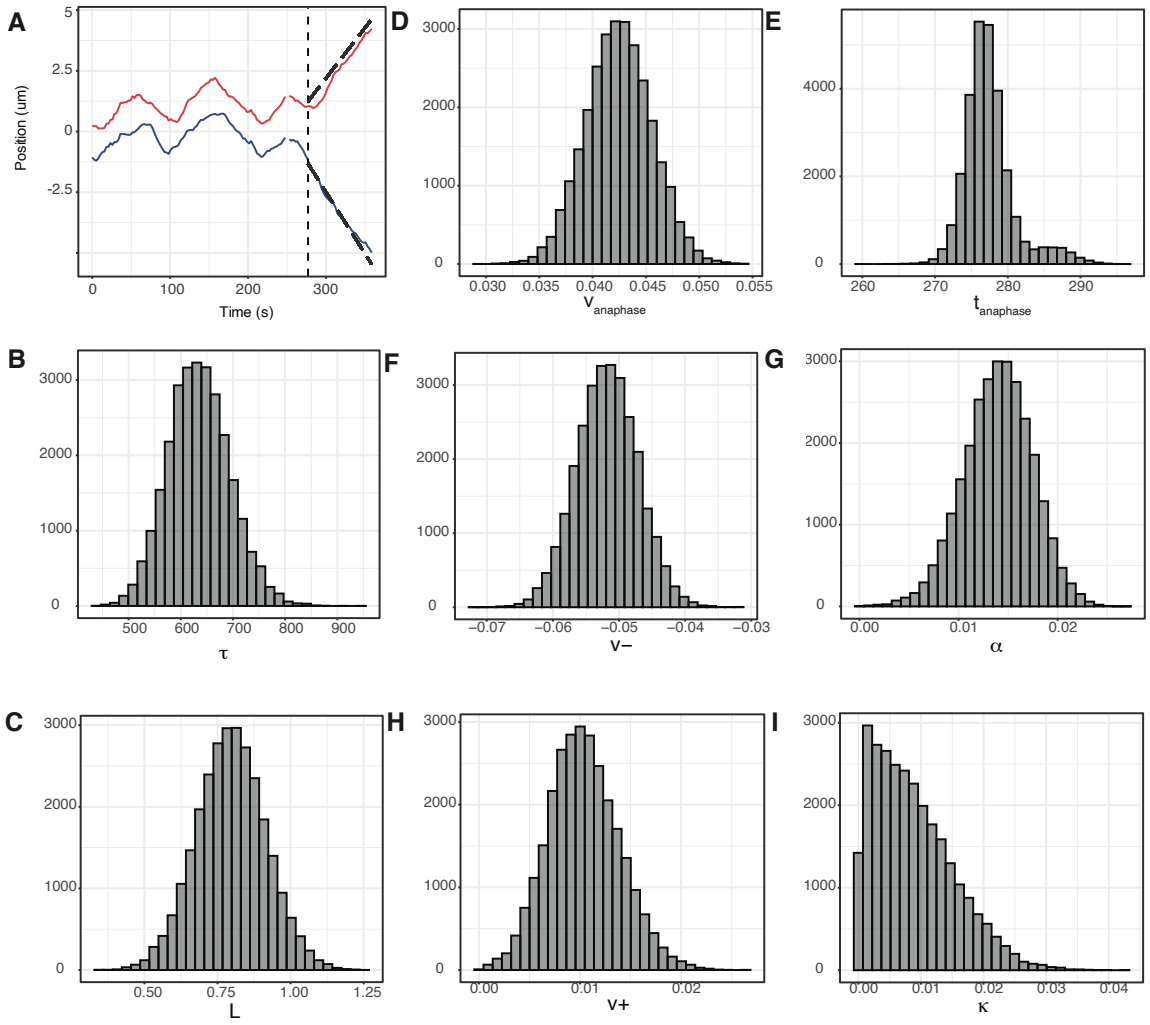

Figure B14: Single trajectory metaphase-anaphase model inference showing parameter estimates and trajectory annotation (DMSO treated cell). **A** Observed KT sister pair trajectory. **B-I** Marginal posterior distribution of the biophysical parameters for the trajectory data in A using the metaphase-anaphase model. Note: v_-, v_+ and $v_{anaphase}$ are averaged over the two sisters.

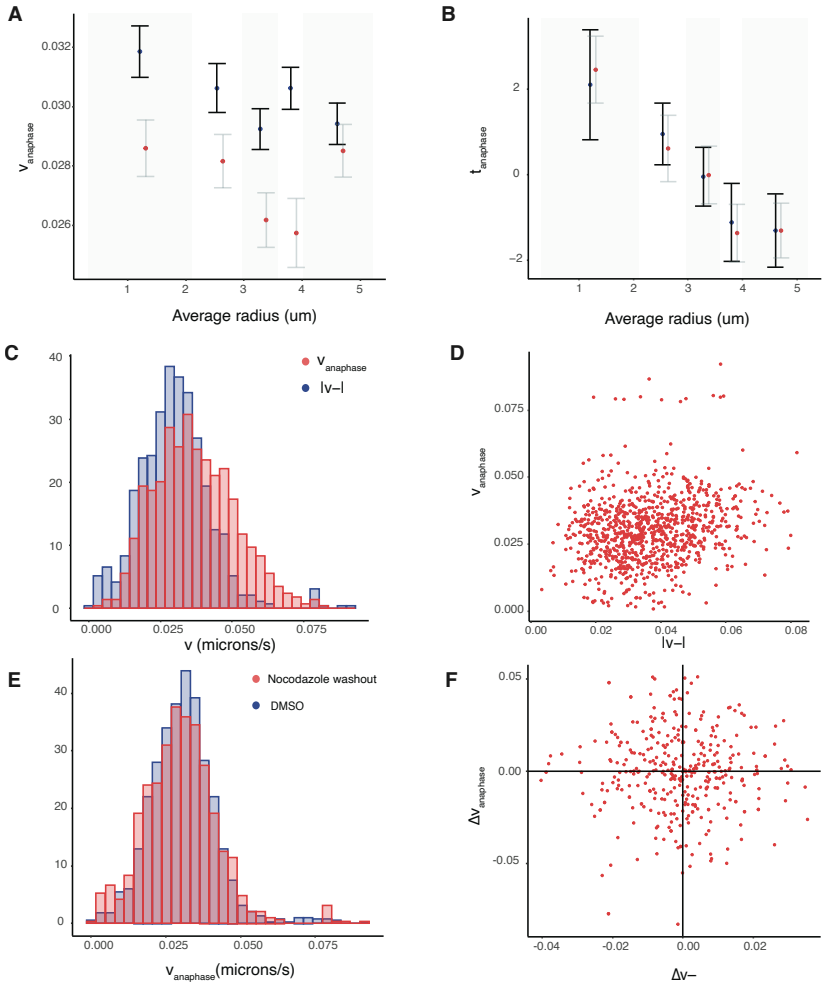

Figure B15: Homogeneity of anaphase K-fibers in DMSO cultured and nocodazole washout cells. **A/B** Spatial biophysical parameter trends across the metaphase plate for anaphase speed/anaphase timings for DMSO (blue) and nocodazole washout (red) treated cells. The estimated correlation between anaphase speed and relative anaphase timings is 0.125 ($p_{Corr} < 10^{-4}$). **C** Estimated densities of $v_{anaphase}$ (red) and pulling force (blue) for nocodazole washout treated cells. **D** Correlation of anaphase speed and absolute v_- (estimated correlation = 0.174, $p_{Corr} < 10^{-15}$). **E** $v_{anaphase}$ for DMSO (blue) and nocodazole washout treated cells. Distributions are not statistically different ($p_{MW} = 0.165$), with the variance of $v_{anaphase}$ nocodazole washout pairs being greater ($p_{Ftest} < 10^{-4}$). **F** Difference of $v^1_{anaphase}$ and $v^2_{anaphase}$ versus v^1_- and v^2_- only on asymmetric (on v_-) sister pairs, for nocodazole washout treated cells. No statistically significant correlation is observed. Inference is based on 456 pairs across 30 nocodazole treated cells.

7 **KT positioning analysis**

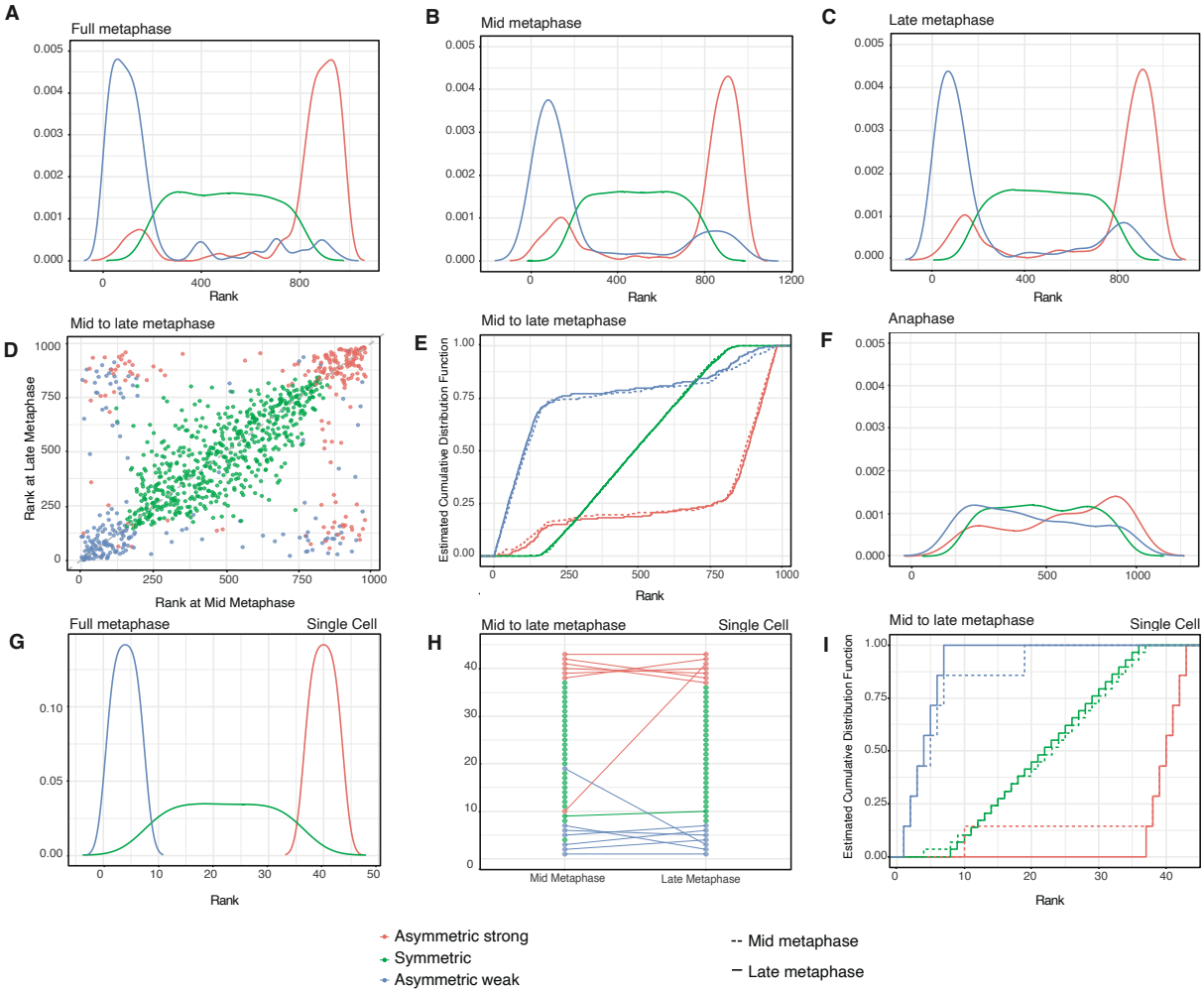

Figure B16: A rank analysis of the lateral organisation of the MPP in DMSO cultured cells. **A/B/C/F** Estimated probability density function of the ranks of averaged positions (from the centre of the metaphase plate) of DMSO treated kinetochores over different periods. **A** full metaphase (185 frames), **B** mid metaphase (80 frames), **C** late metaphase (80 frames) and **F** anaphase (80 frames). **D/E** Change of rank of the averaged positions from mid to late metaphase, for DMSO treated cells, averaged over 50 frames. **D** Scatter plot, **E** estimated cumulative distribution. **G** Estimated probability density function of the ranks of the averaged positions (from the centre of the metaphase plate) of kinetochores over the whole metaphase (185 frames) for a single cell. **H** Rank changes of the positions of kinetochores in a cell, from mid to late metaphase. Lines connecting points from mid to late metaphase indicate the rank of a particular sister KT at these two periods, for the same cell as in G. **I** estimated cumulative distribution of rank changes from mid to late metaphase for the same cell as in G. Red colour denotes the stronger pulling asymmetric sisters, blue the weaker pulling asymmetric sisters and green the symmetric sisters.

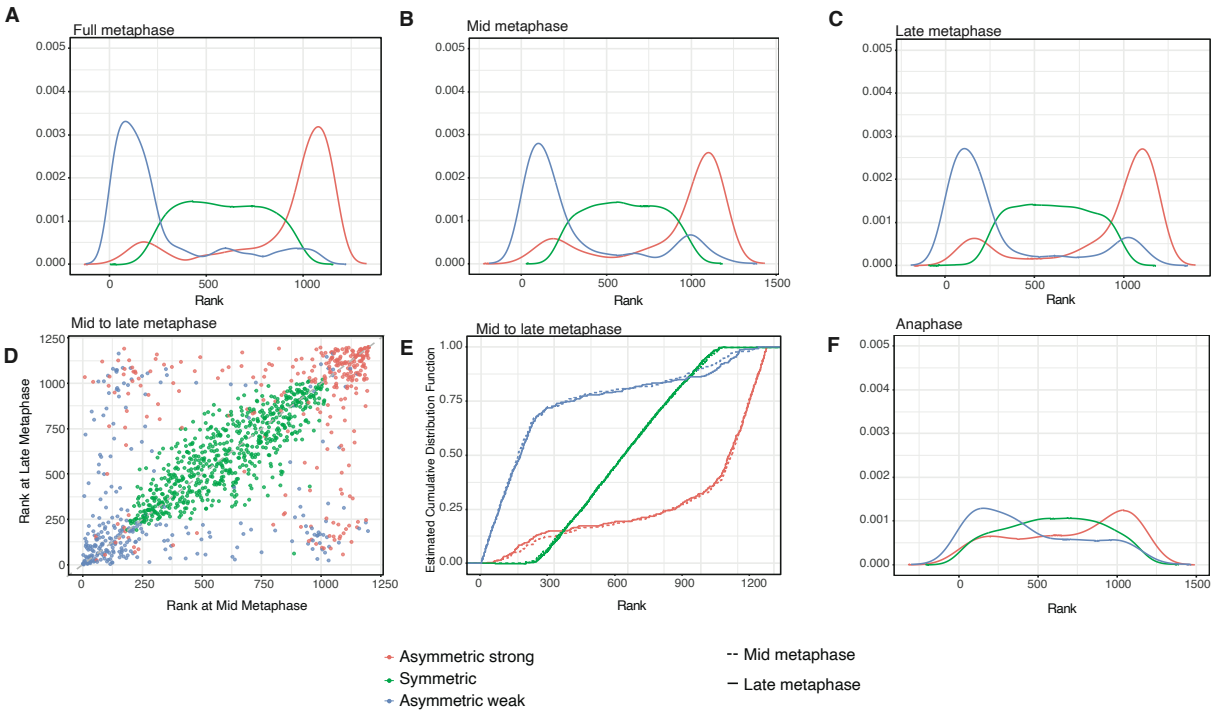

Figure B17: A rank analysis of the lateral organisation of the MPP in nocodazole washout treated cells. **A/B/C/F** Estimated probability density function of the ranks of averaged positions (from the centre of the metaphase plate) of nocodazole washout kinetochores over different periods. **A** full metaphase (185 frames), **B** mid metaphase (80 frames), **C** late metaphase (80 frames) and **F** anaphase (80 frames). **D/E** Change of rank of the averaged positions from mid to late metaphase, averaged over 50 frames. **D** Scatter plot, **E** estimated cumulative distribution. Red colour denotes the stronger pulling asymmetric sisters, blue the weaker pulling asymmetric sisters and green the symmetric sisters.

C Methodology

Likelihood and posterior distribution computation

The metaphase dynamics of eq. (1), are described in detail in Armond et al. [2015a]. The model is a discretised system of equations – discrete measurement time with equal time steps:

$$\left(X^1_{t+\Delta t} - X^1_t\right) = \Delta t\left(-v_{\sigma^1_t} - \kappa\left(X^1_t - X^2_t - L\cos\theta_t\right) - \alpha X^1_t\right) + \sqrt{\Delta t}\mathcal{N}\left(0,\tau^{-1}\right),$$
$$\left(X^2_{t+\Delta t} - X^2_t\right)t = \Delta t\left(+v_{\sigma^2_t} - \kappa\left(X^2_t - X^1_t + L\cos\theta_t\right) - \alpha X^2_t\right) + \sqrt{\Delta t}\mathcal{N}\left(0,\tau^{-1}\right),$$

The kinetochore pair K-fiber state, σ_t, (hidden), takes values in the 4 states,

$$(\sigma^1,\sigma^2) \in \{(+,+),(+,-),(-,+),(-,-)\}, \tag{7}$$

and has transition matrix P (parametrised by p_{coh}, p_{icoh}, the probabilities of remaining in the same state (either coherent or incoherent).

In sum, the observations obey a Stochastic Differential Equation (SDE), with the observation at time t depends only on the previous observation x_{t-1} and the state at time t, while the hidden states are described by the transition probability matrix.

$$x_t \mid \sigma_t, x_{t-1} \sim \mathcal{N}\left(\Delta t f_{\sigma_t}\left(x_{t-1}\right), \Delta t/\tau\right) \quad \text{and} \quad \sigma_t \mid \sigma_{t-1} \sim \text{categorical}\left(P\right).$$

with

$$f^k_i\left(\sigma^i_k\right) = (-1)^k v_{\sigma^k_i} + (-1)^k \kappa\left(d_i - L\cos\left(\theta_i\right)\right) - \alpha\left(x^k_i\right)$$

The likelihood of each sister is given by

$$L\left(x^k \mid v_\pm, \kappa, \alpha, \tau, L, \sigma^k_i, \theta_i\right) = (2\pi)^{-(n-1)}\tau^{n-1}\prod_{k=1,2}\left(\exp\left(-\frac{\tau_0}{2}\sum_{i=1}^{n-1}\left(\left(dx^k_i - \Delta t f^k_i\left(\sigma^i_k\right)\right)^2\right)\right)\right)$$

This model can be modified accordingly to allow for asymmetry, as in eq. (2), and time dependency, as in eq. (4). The likelihood calculation for the asymmetric model is straightforward and hence is omitted. However, while the generalization to asymmetric models is relatively straightforward, the increased complexity lead us to use the following transformations for velocities

$$v^1_{+/-} = v^{mean}_{+/-} + d_{+/-} \quad \text{and} \quad v^2_{+-} = v^{mean}_{+/-} - d_{+/-}, \quad \text{with} \quad -2v^{mean}_{+/-} \le d_{+/-} \le 2v^{mean}_{+/-},$$

which improve the mixing of the Hamiltonian Monte Carlo algorithm. The likelihood for the full time dependent model is shown below.

$$\begin{aligned} &L\left(x^k \mid v_{\pm,0}, \kappa_0, \alpha_0, \tau_0, L, v_{\pm,1}, \kappa_1, \alpha_1, \tau_1, \sigma^k_i, \theta_i\right) \\ &= (2\pi)^{-(n-1)}\tau_0^{n-1}\exp\left(\tau_1\frac{n(n-1)}{2}\Delta t\right)\prod_{k=1,2}\left(\exp\left(-\frac{\tau_0}{2}\sum_{i=1}^{n-1}\left(exp\left(\tau_1 i\Delta t\right)\left(dx^k_i - \Delta t f^k_i\left(\sigma^i_k\right)\right)^2\right)\right)\right) \\ &f^k_i\left(\sigma^i_k\right) = (-1)^k v_{\sigma^k_i,0}\exp\left(v_{\sigma^k_i,1} i\Delta t\right) + (-1)^k \kappa_0\exp\left(\kappa_1 i\Delta t\right)\left(d_i - L\cos\left(\theta_i\right)\right) - \alpha_0\exp\left(\alpha_1 i\Delta t\right)\left(x^k_i\right) \end{aligned} \tag{8}$$

Forward - Stochastic Backward Algorithm

We leverage a modified Forward-Backward (FB) algorithm, [Scott, 2002], to calculate the likelihood and make inference on the parameters. In particular, we use the Forward - Backward stochastic recursion within the STAN environment, [Stan Development Team, 2024a].

The FB algorithm is designed to exploit via recursion the conditional independencies in the HMM. The forward likelihood is defined as $l_t(i) = P\left(x_{1:t}, \sigma_t = i \mid \theta\right)$, which is the joint likelihood of the data $x_{1:t}$ and the state $\sigma_t = i$ averaging over the states up to time $t-1$. The likelihood contribution from data $x_{1:t}$ is just the sum $l^*_t = \sum_i l_t(i)$. Let $\eta_{j,t} = P\left(x_t \mid x_{1:t-1}, \sigma_t = j; \theta\right)$, be the likelihood contribution of an observation, x_t under all states j, $P\left(\sigma_t = i \mid \sigma_{t-1} = j\right)$ the probability that at time t the state will be i given at $t-1$ was at state j, as given by

the HMM transition probability matrix and θ all the unknown parameters. A recursive relationship can be derived as follows

$$\begin{aligned}
l_t(i) &= P(x_{1:t}, \sigma_t = i \mid \theta) \\
&= \sum_j P(x_t, x_{1:t-1}, \sigma_t = i, \sigma_{t-1} = j; \theta) \\
&= \sum_j P(x_t \mid x_{1:t-1}, \sigma_t = i, \sigma_{t-1} = j; \theta)\, P(\sigma_t = i, \sigma_{t-1} = j, x_{1:t-1}) \\
&= \sum_j P(x_t \mid x_{1:t-1}, \sigma_t = i; \theta)\, P(\sigma_t = i \mid \sigma_{t-1} = j, x_{1:t-1})\, P(\sigma_{t-1} = j, x_{1:t-1}) \\
&= \sum_j P(x_t \mid x_{1:t-1}, \sigma_t = i; \theta)\, P(\sigma_t = i \mid \sigma_{t-1} = j)\, P(\sigma_{t-1} = j, x_{1:t-1}) \\
&= \sum_j P(x_t \mid x_{1:t-1}, \sigma_t = i; \theta)\, P(\sigma_t = i \mid \sigma_{t-1} = j)\, l_{t-1}(j) \\
&= \sum_j \eta_{i,t}(x_t; \theta)\, P(\sigma_t = i \mid \sigma_{t-1} = j)\, l_{t-1}(j)
\end{aligned} \tag{9}$$

It is then obvious that the log-likelihood is the sum of all states at time $t = T$, *i.e.,*

$$L(x) = \log\left(P(x_{1:T}; \theta) = \sum_i l_T(i)\right.$$

Now, let $\xi_{j,t} = P(\sigma_t = j \mid x_{1:t}; \theta)$ be the probability of being in state σ_t at time t given all the data up to that time. Taking as initial condition $\xi_0 = P(\sigma_0 = j \mid \theta) = [0, 0.5, 0.5, 0]^T$, i.e., at time $t = 0$ it is equally probable to be in one of the coherent states $(+-, -+)$. Observe that

$$l_t(i) = P(x_{1:t}, \sigma_t = i) = P(\sigma_t = i \mid x_{1:t})\, P(x_{1:t}) = \xi_{i,t} P(x_{1:t}) = \xi_{i,t} \sum_i l_t(i)$$

and note that $f_t = P(x_t \mid x_{1:t-1}) = \sum_i \sum_j \eta_{i,t}(x_t; \theta)\, P(\sigma_t = i \mid \sigma_{t-1} = j)\, \xi_{j,t-1}(i)$ then eq. (9) can be modified and calculate the forward probabilities $\xi_{i,t} = \frac{l_t(i)}{\sum_i l_t(i)}$ instead,

$$\begin{aligned}
\xi_{i,t}(i)\, P(x_{1:t}) &= \sum_j \eta_{i,t}(x_t; \theta)\, P(\sigma_t = i \mid \sigma_{t-1} = j)\, \xi_{j,t-1}(i)\, P(x_{1:t-1}) \\
&= \sum_j \eta_{i,t}(x_t; \theta)\, P(\sigma_t = i \mid \sigma_{t-1} = j)\, \xi_{j,t-1}(i)\, P(x_{1:t-1})
\end{aligned}$$

and deriving our final recursive relationship

$$\begin{aligned}
\xi_{i,t}(i) &= \sum_j \eta_{i,t}(x_t; \theta)\, P(\sigma_t = i \mid \sigma_{t-1} = j)\, \xi_{j,t-1}(i)\, P(x_{1:t-1}) \\
&= \sum_j \eta_{i,t}(x_t; \theta)\, P(\sigma_t = i \mid \sigma_{t-1} = j)\, \frac{\xi_{j,t-1}(i)}{P(x_t \mid x_{1:t-1})} \\
&= \sum_j \eta_{i,t}(x_t; \theta)\, P(\sigma_t = i \mid \sigma_{t-1} = j)\, \frac{\xi_{j,t-1}(i)}{f_t}
\end{aligned}$$

and likelihood is

$$L(x) = \log \sum_t f_t$$

In our setting, we have

$$\eta_{\sigma_t,t} \equiv \mathcal{N}\left(x_t \mid x_{t-1} + \Delta t\, M x_{t-1} + \Delta t\, \tilde{M} \sigma_t + \Delta t \mu, \Delta t \tau^{-1}\right)$$

where M, $\tilde{M}$, and μ are derived from the linear SDE and given by

$$M = \begin{bmatrix} \kappa - \alpha & \kappa \\ \kappa & -\kappa - \alpha \end{bmatrix}$$

and

$$\tilde{M} = \begin{bmatrix} -v_+ & -v_+ & -v_- & -v_- \\ v_+ & v_- & v_+ & v_- \end{bmatrix}$$

$$\mu = [\kappa L \cos(\theta_t), \kappa L \cos(\theta_t)]^T.$$

In this notation, the state variable $x_t = [X_t^1, X_t^2]^T$ represents the positions of both sisters in a pair at time t and the state $\sigma_t \in \{[1,0,0,0]^T, [0,1,0,0]^T, [0,0,1,0]^T, [0,0,0,1]^T\}$ corresponding to the states $\{++, +-, -+, --\}$ for the sister kinetochore pair at time t.

In order to make statements about switching events, we need to consider sequences of states forming a pattern corresponding to coherent switches from one coherent state to another via an intermediate state. To address this, we sample from the full hidden state sequence given all the data, and assess this for switches. We use the stochastic backward simulation to simulate/sample the hidden states, which is a rapidly mixing algorithm, [Scott, 2002]. Observe that

$$P(\sigma_{1:T} \mid x_{1:T}, \theta) = P(\sigma_T \mid x_T) \prod_{t=1}^{T-1} P(\sigma_{T-t} \mid \sigma_{T-t+1} x_{1:T})$$

Then, keeping the terms that depend on σ_t, the it is easy to show the following

$$\begin{aligned} P(\sigma_t = i \mid \sigma_{t+1} = j, x_{1:T}) &= \frac{P(\sigma_t = i, \sigma_{t+1}, x_{1:T})}{P(\sigma_{t+1} = j, x_{1:T})} \\ &\propto P(\sigma_t = i, x_{1:T}) P(\sigma_{t+1} = j \mid \sigma_t = i) P(x_{t+1:T} \mid s_{t+i}) \\ &\propto P(\sigma_t = i, x_{1:t}) P(\sigma_{t+1} = j \mid \sigma_t = i) \\ &\propto \xi_{i,t} f_t P(\sigma_{t+1} = j \mid \sigma_t = i) \end{aligned} \tag{10}$$

The strategy for the backward sampling algorithm is therefore to sample initially from $p(\sigma_T \mid x_{1:T}) = \xi_{T,i}$ as dervived in the forward recursion and subsequently to simulate backward in time from $T-1$ to 1 via the conditional distribution given in eq. (10).

Missing data treatments

Suppose we have missing observations. Let's assume that the data comprises two sections $[1:T_1]$ and $[T_2:T]$, with $T_2 = T_1 + 1 + l > T_1$, *i.e.,* a gap of size $l \geq 1$ where data on both sisters is missing. Given the Markovian property of the observations, we can construct the multi-time point conditional, $P(X_{t+k\Delta t}, \sigma_{t+k\Delta t} \mid X_t, \sigma_t, \theta)$. Incorporating the dependence on the hidden state path, we get the following expression,

$$P(X_{t+k\Delta t}, \sigma_{t+1:t+k\Delta t} \mid X_t, \sigma_t, \theta) = P(\sigma_{t+1:t+k\Delta t} \mid \sigma_t, \theta) P\left(X_{t+k\Delta t} \mid X_t, \sigma_{t:t+(k-1)\Delta}, \theta\right)$$

Thus, we have the full history dependency $P(X_{T_2} \mid X_{1:T_1})$ across a gap.

We consider then obtain the likelihood,

$$L(x_{1:T_1 \cup T_2:T}, \sigma_{1:T} \mid \theta) = P(x_{1:T_1}, \sigma_{1:T_1} \mid \theta) P(x_{T_2}, \sigma_{T_1+1:T_2} \mid x_{T_1}, \sigma_{T_1}, \theta) P(x_{T_2+1:T}, \sigma_{T_2:T} \mid x_{T_2}, \sigma_{T_2}, \theta)$$

and the marginalised likelihood $L(x_{1:T_1 \cup T_2:T} \mid \theta)$ given by summation over the hidden state $\sigma_{1:T}$.

There are a lot of different methods that we can utilise that deal with the gap (middle) terms,

$$P(x_{T_2}, \sigma_{T_1+1:T_2} \mid x_{T_1}, \sigma_{T_1}, \theta)$$

, and each comes with its own set of strengths and weaknesses.

In brief, there we have four options. First, we could fill in the missing values with linear interpolation, secondly, treat sections as independent, *i.e.,* multiply the likelihoods for each section, thirdly, remove data points from the likelihood calculation but retain hidden state propagation, fourthly, impute the hidden values by sampling from the posterior predictive distribution

$$P(x_{missing} \mid x_{obs}, \theta)$$

(using a Brownian Bridge sampler). The first two methodologies are approximating the actual time-series, as if there were no missing values and thus, they introduced a bias which can be, in some cases, non- negligible. The third method, doesn't utilise all the available information, while the fourth option – even though is the most flexible option for extending to missing values of a single sister – it is likely computationally expensive for large gaps. Taking into account the advantages and limitations of each method, we have chosen to work with the third method, which we have found that it optimally balances the trade-off between reducing computational complexity and introducing estimation bias.

Reduced likelihood method

Consider the full likelihood. The gap term can be expressed as,

$$P\left(x_{T_2}, \sigma_{T_1+1:T_2} \mid x_{T_1}, \sigma_{T_1}, \theta\right) = P\left(x_{T_2} \mid x_{T_1}, \sigma_{T_1:T_{T_2-1}}, \theta\right) P\left(\sigma_{T_1+1:T_2} \mid \sigma_{T_1}, \theta\right)$$

The idea here is to exclude the propagation term for x_{T_2}, i.e, use the reduced full likelihood

$$L_r\left(x_{1:T_1 \cup T_2:T}, \sigma_{1:T} \mid \theta\right) = P\left(x_{1:T_1}, \sigma_{1:T_1} \mid \theta\right) P\left(\sigma_{T_1+1:T_2} \mid \sigma_{T_1}, \theta\right) P\left(x_{T_2+l:T}, \sigma_{T_2:T} \mid x_{T_2}, \sigma_{T_2}, \theta\right).$$

giving the corresponding reduced marginalised likelihood $L_r\left(x_{1:T_1 \cup T_2+1:T} \mid \theta\right)$ (here we removed x_{T_2} in notation as information in knowing x_{T_2} is not used. However, the likelihood depends on x_{T_2}, as it is part of the history).

We *propose* to modify the forward algorithm, based on the above lines. In particular, we change the forward likelihood calculation by assuming that the likelihood contribution of the missing observations is 0 and hence, the likelihood contribution at that specific time point, is only defined by the transition probabilities.

We have made a series of experiments, to proof that this methodology is robust and gives unbiased results. In particular, we have compared the likelihood estimations of different simulated data sets, with varying missing data proportions and different distributed missing values (changing the size of the gaps). Also, we have compared the results of this methodology with the results of the first method,*i.e.,* filling the missing data by linear interpolation, which gave similar results, when the missing values' gaps were small. In Appendix Table C6 we present a case study where we have

Actual values	No missing			Single missing			Double missing			Triple missing			All-in-a-row		
	Mean	Variance	p-value	Mean	Variance	p-value	Mean	Variance	p-value	Mean	Variance	p-value	Mean	Variance	p-value
$\tau^1 = 500$	535.53	72.80	0.75	536.75	82.07	1.00	514.33	80.23	0.75	542.16	79.12	1.00	536.98	77.69	1.00
$\tau^2 = 300$	289.01	38.85	0.35	289.82	43.34	1.00	294.92	43.25	1.00	294.84	41.93	1.00	287.27	41.11	0.75
$\kappa = 0.02$	0.022	0.0090	0.35	0.021	0.0097	0.22	0.022	0.0095	0.35	0.021	0.0092	1.00	0.022	0.0097	1.00
$\alpha = 0.06$	0.064	0.0084	1.00	0.061	0.0097	0.75	0.062	0.0096	1.00	0.0062	0.0091	1.00	0.064	0.0092	0.75
$v_-^1 = -0.04$	-0.040	0.008	1.00	-0.039	0.008	0.11	-0.039	0.008	0.35	-0.040	0.008	1.00	-0.040	0.008	1.00
$v_-^2 = -0.06$	-0.059	0.008	1.00	-0.060	0.009	0.51	-0.059	0.008	0.75	-0.058	0.008	0.75	-0.060	0.008	0.75
$v_+^1 = 0.02$	0.020	0.006	0.75	0.019	0.007	1.00	0.018	0.007	1.00	0.019	0.006	1.00	0.019	0.007	1.00
$v_+^2 = 0.042$	0.042	0.007	1.00	0.041	0.007	0.11	0.042	0.007	1.00	0.040	0.007	1.00	0.042	0.007	0.75
$L = 0.75$	0.789	0.119	0.02*	0.789	0.119	0.002*	0.789	0.118	0.02*	0.789	0.119	0.001*	0.789	0.119	0.02*
$p_{icoh} = 0.75$	0.736	0.074	0.35	0.757	0.079	0.35	0.715	0.089	0.35	0.744	0.080	1.00	0.736	0.075	1.00
$p_{coh} = 0.93$	0.914	0.024	0.35	0.915	0.026	1.00	0.907	0.027	1.00	0.914	0.025	1.00	0.912	0.025	0.51

Table C6: Summary of the case study for checking the bias of our algorithm when we have no missing data and 10% missing data points under various settings, *i.e.,* single missing data points, double missing data points, triple missing data points and all-in-a-row missing data points. The case study comprises ten different simulated time-series of length $T = 180$, from a common multivariate distribution, in an effort to Average posterior mean MCMC estimates, average posterior MCMC variance and p-values of the two-sided exact binomial test presented. The null hypothesis is that there is 0.5 probability that the posterior mean estimates are greater than the actual value. Our algorithm gives unbiased results

simulated 10 different time-series of length $T = 180$ and we have assessed whether the different mean posterior estimates where greater than the actual values with probability $p \neq 0.5$. To asses this hypothesis, we performed a two-sided binomial test. In all of our experiments the "reduced likelihood computation" was accurate, with small estimation bias.

Prior distributions

We impose broad prior distributions on the parameters of the biophysical model, as shown in Appendix Table C7. For the natural length of the spring, L, we impose an informative prior based on an additional nocodazole washout experiment (Nocodazole interferes with polymerization of microtubules). This avoids an unidentifiabilty in the model as in Armond et al. [2015a]. Additionally, we use an informative prior for the time of anaphase, t_A, based on first fitting a changepoint model (with a uniform prior on t_A) to get an initial estimate for anaphase onset to guide the biophysical model and avoid exploring parameter space corresponding to pathological behaviour such as anaphase at the start or end of movies.

Statistical Tests

The tests that have been used throughout this study are summarised in Appendix Table C8, describing each test and the abbreviation we use when quoting the p-values in the text.

Parameter	Prior	Support
	Symmetric-Asymmetric Model	
α	$\mathcal{N}\left(\mu = 0.01, \sigma^2 = 0.1^2\right)$	$[0, \infty)$
κ	$\mathcal{N}\left(\mu = 0.05, \sigma^2 = 0.1^2\right)$	$[0, \infty)$
v_-	$\mathcal{N}^0\left(\mu = -0.03, \sigma^2 = 0.1^2\right)$	$(-\infty, 0]$
v_+	$\mathcal{N}_0\left(\mu = 0.3, \sigma = 0.1^2\right)$	$[0, \infty)$
p_{icoh}	$\mathcal{B}eta\left(2, 1\right)$	$(0, 1)$
p_{coh}	$\mathcal{B}eta\left(2.5, 1\right)$	$(0, 1)$
L	$\mathcal{N}_0\left(\mu = 0.79, \sigma^2 = 0.119^2\right)$	$[0, \infty)$
$\tau^{1,2}$	$\mathcal{G}amma\left(0.5, 10^{-3}\right)$	$[0, \infty)$
	Asymmetric Model	
v_-^{mean}	$\mathcal{N}^0\left(\mu = -0.03, \sigma^2 = 0.1^2\right)$	$(-\infty, 0]$
d_-	$\mathcal{N}_{-2v_-^{mean}}^{2v_-^{mean}}\left(\mu = 0, \sigma^2 = 0.1^2\right)$	$[-2v_-^{mean}, 2v_-^{mean}]$
v_+^{mean}	$\mathcal{N}_0\left(\mu = 0.3, \sigma = 0.1^2\right)$	$[0, \infty)$
d_+	$\mathcal{N}_{-2v_+^{mean}}^{2v_+^{mean}}\left(\mu = -0.03, \sigma^2 = 0.1^2\right)$	$[-2v_+^{mean}, 2v_+^{mean}]$
	Temporal Parameters	
p_1	$\mathcal{N}\left(\mu = 0, \sigma^2 = 0.00382^2\right)$	$[0, \infty)$
$*$ Note: p_1: any temporal variable		
	Metaphase-Anaphase Model	
$v_{anaphase}^{1,2}$	$\mathcal{N}^0\left(\mu = 0.3, \sigma^2 = 0.1^2\right)$	$[0, \infty)$
$t_{anaphase}$	$\mathcal{N}_t\left(\mu = t^*, \sigma^2 = (3\Delta t)^2\right)$	$[0, \infty)$

$*$ Note 1: $\mathcal{N}_t$: lower truncated Normal distribution at t
$*$ Note 2: $\mathcal{N}^t$: upper truncated Normal distribution at t
$*$ Note 3: $\mathcal{N}_{t_1}^{t_2}$: lower and upper truncated Normal distribution at t_1 and t_2 respectively
$*$ Note 4: t^*: median (initial) estimate of anaphase time over all KT pairs in a cell

Table C7: Priors for the symmetric, asymmetric, temporal, metaphase-anaphase models.

Test	Type	Null Hypothesis (H_0)	Abbreviation
Kolmogorov-Smirnov	Non-parametric	Equality of 2 continuous distributions	KS
Mann-Whitney (Wilcoxon rank)	Non-parametric	Equality of 2 distributions	MW
Pearson's (χ^2)	Non-parametric	Count numbers come from a Multinomial distribution	Pearson
		Goodness of fit	
		Homogeneity of counts for ≥ 2 groups under the same variable	
		Independence of 2 variables (via Contingency table)	
Spearman's	Non-parametric	No monotonic relationship between 2 ranked variables	Spearman
Kendall's	Non-parametric	Dependence of 2 distributions is 0	Kendall
Pearson's Correlation	Parametric	No linear correlation	Corr
Binomial	Exact test	Two categories occur with equal frequency	Binom
Hoeffding's	Non-parametric	Independence of 2 continuous distributions	Hoef
Distance Covariance	Non-parametric	Multivariate independence	DC
Brown-Forsythe test	Non-parameteric	Variances of 2 groups are homogeneous (equal)	BF
Z-test	Parametric	Mean of a population is μ_0	Ztest
		Equality of the means of 2 populations	
F-test	Parametric	Equality of variances	Ftest

Table C8: Summary of tests used in this analysis. The first column refers to the test, the second the type of the test, *i.e.,* assumptions, the third column describes the null hypothesis and hence the test, while the last column states the abbreviation that is used throughout this study, when referring to p-values.

Implementation: STAN

All our models were implemented in STAN, [Stan Development Team, 2024a] and fitted using the R-package "rstan". STAN is based on a C++ language which obtains posterior samples of the Bayesian models by defining the aforementioned likelihoods and priors. We then used R to access the output, evaluate the posterior densities and likelihoods to make inference on the parameters.

Model selection

Model selection is based on pairwise comparison of models using the Bayes Factors (BF). We use the criteria of Kass and Raftery [1995] and chose the more complex model if it had at least substantial preference over the simpler model ($BF > 3.2$). The BF for model M' relative to a simpler model M is is just the ratio of the models' marginal likelihoods

$$B = \frac{\pi\left(D \mid M'\right)}{\pi\left(D \mid M\right)} = \frac{P\left(M' \mid D\right) P\left(M'\right)}{P\left(M \mid D\right) P\left(M\right)}$$

Assuming that the models are equally probable a priori, *i.e.,* $P\left(M'\right) = P\left(M\right)$, then the BF can be seen as the posterior odds ratio. At first, we compute the BF of all models relative to our base model eq. (1). Then, we determine which models have a substantial preference over the base model. If there are more than one models with substantial preference, and all of these models have the same complexity (*i.e.,* equal number of parameters), we choose the model with the highest BF. If the set of models with substantial preference, contains models with different complexities and the more complex models (*i.e.,* models with higher number of parameters), are nested to any of the other models in the set,then we compute the Bayes Factor of the complex-nested model relative to the simpler model and we choose the more complex model only when the preference of the complex model relative to simpler model is at least substantial and hence increasing the complexity is justified. Finally, if the set of models with substantial preference are models with different complexities but none of them is nested to another, then again we choose the model with the highest BF over the base model.

We use the "bridgesampling" package in R, which computes the log-marginal likelihood for every model, using the log-likelihood samples passed from STAN HMC samples (which were in turn computed in the Forward Backward algorithm). This package utilizes the bridge sampling, [Meng and Wong, 1996, Gronau et al., 2020]. Then, the BF is just the ratio of the marginal likelihoods.

Convergence diagnostics

Convergence and mixing of MCMC chains is assessed via the Gelman-Rubin $\hat{R}$ statistic, [Gelman and Rubin, 1992, Vehtari et al., 2021], using only results where $\hat{R} < 1.05$ for all parameters.

Of $N = 82$ cells tracked, MCMC chains were run successfully for $N = 59$ cells, *i.e.,* 26 and 33 DMSO and nocodazole washout. Where MCMC chains failed to run this was due either to poor tracking results in that cell (insufficient tracked kinetochore pairs or existence of too many missing data) or long time series such that the MCMC chains progressed extremely slowly (failed to find the typical set). Of the $n = 1577$ kinetochore pairs across 59 cells where MCMC chains ran successfully, MCMC chains from $n = 27$ (1.5%) kinetochore pairs failed to converge as assessed by the $\hat{R}$ statistic, leaving estimates from $n = 1550$ kinetochore pairs.

Convergence proportions were slightly lower for the time dependent and metaphase-anaphase model, due to the increased complexity of these models.

D Additional Models

Changepoint model

A simple changepoint model [Armond et al., 2019] to assess the time of anaphase assumes that the intersister distance between a kinetochore pair is constant in metaphase, and increases linearly in time during anaphase. If d_t is the 1D intersister distance (in the x direction perpendicular to the metaphase plate) between kinetochore sisters, then at time point t_i

$$d_{t_i} = \begin{cases} a_1 + \varepsilon_i \text{ for } t_i < t_A, \\ a_2 + b_2 t_i + \varepsilon_i \text{ for } t_i \geq t_A, \end{cases}$$

with the condition that $a_1 = a_2 + b_2 t_A$. Since this model is simpler than the biophysical model, a uniform prior can be used for t_A and weakly informative priors for other parameters.

Multivariate Normal mixture model

The multivariate Normal (Gaussian) model is a generalisation of the univariate normal model

$$\mathcal{N}_d\left(x \mid \mu, \Sigma\right) = \frac{1}{(2\pi)^{D/2}} \frac{1}{|\Sigma|^{1/2}} exp\{-\frac{1}{2}(x-\mu)^T \Sigma^{-1}\left(x-\mu\right)\}$$

with $\mu \in \mathcal{R}^d$, the location vector and $\Sigma \in \mathcal{R}^{d \times d}$, the covariance matrix. We assume that v_- and v_+ follow a multivariate normal distribution (allowing for v_- and v_+ to be dependent). Moving a step further, we have found that the model which explains the 2-dimensional distribution of pulling and pushing forces, is a 3-component multivariate normal mixture model which is defined as a linear superposition of the aforementioned multivariate normal model, *i.e.,* v_- and v_+ have the following distribution,

$$f\left(x\right) = \sum_{k=1}^{K} \pi_k \mathcal{N}\left(x \mid \mu_k, \Sigma_k\right) \quad \text{subject to} \quad \Sigma_{k=1}^{K} \pi_k = 1$$

with $k = 3$, the number of Gaussian components, $\pi_1 ... \pi_k$, the mixture weights of the components, $\mu = \mu_1 ... \mu_k$, a vector containing the mean of each component and $\Sigma_1 ... \Sigma_k$, the covariance matrices of the components.

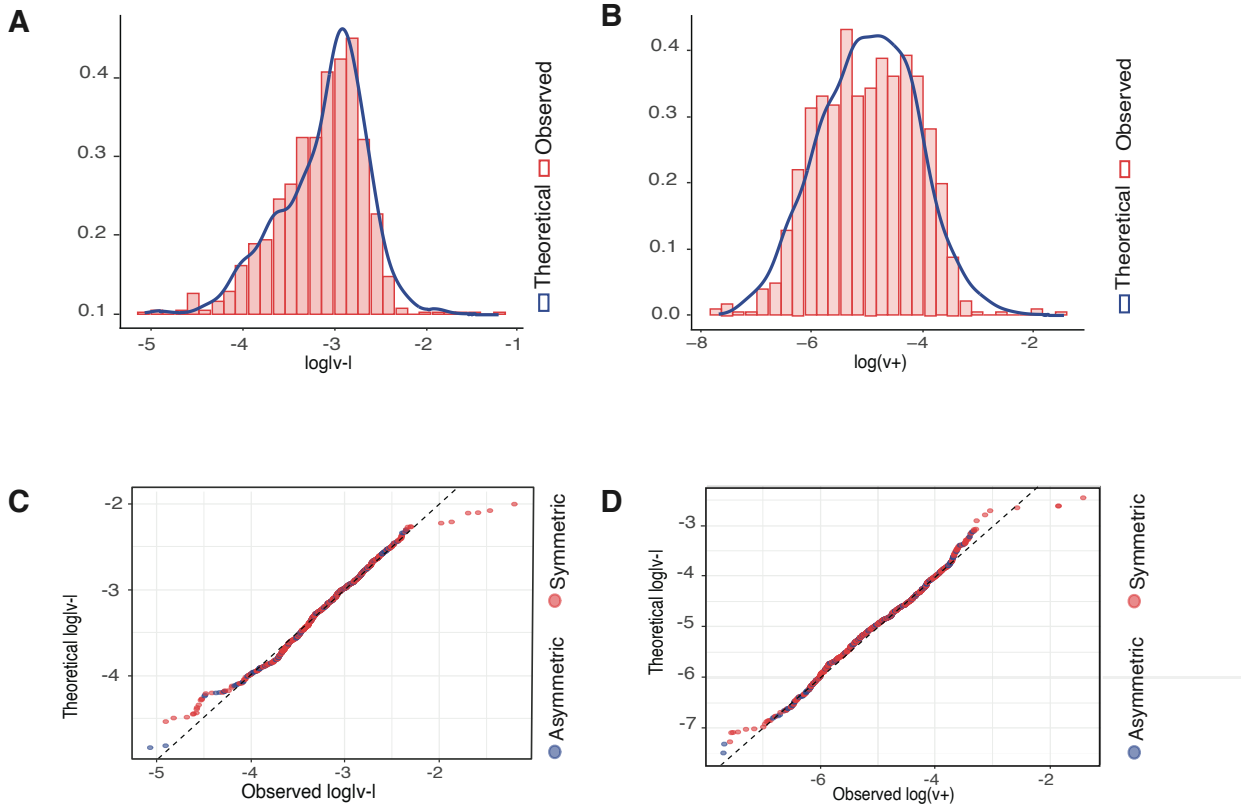

Figure D18: Mixture model of $v_\pm$ joint distribution. **A,B** Histograms of the estimated (red) and theoretical (blue) **A** $\log|v_-|$ and **B** $\log\left(v_+\right)$ of 3−component multivariate normal mixture model. **C,D** QQ plots for 3-component multivariate mixture model showing excellent fit.